POLYMER NETWORKS: MODELING AND APPLICATIONS

A Dissertation
Presented to
The Academic Faculty

By

Hassan Masoud

In Partial Fulfillment
of the Requirements for the Degree
Doctor of Philosophy in the
George W. Woodruff School of Mechanical Engineering

Georgia Institute of Technology

December 2012

POLYMER NETWORKS: MODELING AND APPLICATIONS

Approved by:

Dr. Alexander Alexeev, Advisor
School of Mechanical Engineering
Georgia Institute of Technology

Dr. Richard F. Salant
School of Mechanical Engineering
Georgia Institute of Technology

Dr. David L. Hu
School of Mechanical Engineering
Georgia Institute of Technology

Dr. Paul M. Goldbart
School of Physics
Georgia Institute of Technology

Dr. Alberto Fernandez De Las Nieves
School of Physics
Georgia Institute of Technology

Date Approved: July 26, 2012

To my better half, Parisa,
and my parents, Majid and Farzaneh

ACKNOWLEDGEMENTS

This work is dedicated to my wife, Parisa Pour Shahid Saeed Abadi, for her unconditional and constant love, understanding, and support.

I had the privilege to work with Dr. Alexander Alexeev on seven original projects, three of which are included in this dissertation, since I joined his group in summer 2009. I am very grateful to him for introducing these problems to me and for his invaluable guidance and support. He made my endeavors during the past three years a rewarding and pleasant experience. He also created an environment where I could develop my independent thinking and research skills. I would like to also thank my dissertation reading committee, Drs. Richard F. Salant, Paul M. Goldbart, David L. Hu, and Alberto Fernandez De Las Nieves for reviewing my dissertation and providing me with their valuable insight and comments.

I am thankful to my lab mates, colleagues, and friends for their support and encouragement during my stay at Georgia Tech. A special thank goes to Wenbin Mao for stimulating discussions and for his unreserved help.

I wish to express my sincerest gratitude to the members of APS Padden Award and MRS Graduate Student Award Committees, and judges for the Georgia Tech GTRIC Fellowship for recognizing my research accomplishments as a Ph.D. student. The presentation of my Ph.D. research at scientific conferences and workshops was made possible through generous financial supports I received from the Institute for Complex Adaptive Matter, American Physical Society, Materials Research Society, Gordon

Research Conferences, National Science Foundation, Institute for Mathematics and Its Applications, and Georgia Institute of Technology.

Last but not least, I am ever indebted to my parents, Majid and Farzaneh, who have been my creators, providers and protectors. Their faith in me has always been my main source of motivation.

TABLE OF CONTENTS

LIST OF FIGURES

NOMENCLATURE

List of Symbols[1]

a	Coefficient of conservative DPD force
b	Thickness of capsule membrane
c_{chain}	Number density of polymer chains
c_{chain}^{*}	Overlapping number density
e	Normal strain
$\hat{\mathbf{e}}_x$, $\hat{\mathbf{e}}_y$, and $\hat{\mathbf{e}}_z$	Unit vectors in coordinate directions
f	Coefficient of viscous friction between network and host solvent
$\mathbf{f}_i = \sum_j \mathbf{F}_{ij}^C + \mathbf{F}_{ij}^D + \mathbf{F}_{ij}^R$	Total force applied on bead i from neighboring beads
h	Thickness of network rigid segment
k	Permeability (made dimensionless by square of filaments radius)
k_b	Bending spring constant
k_B	Boltzmann constant
k_{Frankel}	Frankel spring constant
k_{FENE}	FENE spring constant
l_f	Filament length
l_{total}	Total length of springs constituting network filaments
m_i	Mass of bead i

[1] Unless specified otherwise, all dimensional values are given in DPD units.

n_f	Number of filament beads
p	Power value of random weight function
r_c	Cutoff radius of DPD interactions
r_c^{adh}	Cutoff radius of adhesive interactions
r_c^{diss}	Cutoff radius of dissipative DPD force
r_c^{rep}	Cutoff radius of repulsive (conservative) DPD force
r_{eq}	Equilibrium distance of Frankel spring
$\mathbf{r}_i$	Position of bead i
$r_{\max}$	Maximum extension of FENE spring
t	Time
u	Characteristic volume flow rate of encapsulated fluid per unit membrane area
$\langle u \rangle$	Volume-averaged flow velocity
$\mathbf{v}_i$	Velocity of bead i
x, y, and z	Coordinate directions
n_{total}	Total number of beads in simulation box
A, B, C, and C_0	Constants
C_{ave}	Average connectivity of cross-linking nodes
D	Diffusion coefficient
D_0	Diffusion coefficient in the absence of network
D_c	Collective diffusion coefficient of network
D_n	Effective diffusion coefficient
$\mathbf{F}_{external}$	External body force

$\mathbf{F}^C$	Conservative DPD force
$\mathbf{F}^D$	Dissipative DPD force
$\mathbf{F}^R$	Random DPD force
G	Shear modulus (made dimensionless by k_{Frankel}/r_c)
G'	Storage modulus (made dimensionless by k_{Frankel}/r_c)
G'_0	Storage modulus at zero frequency
G'_∞	Storage modulus at very large (infinite) frequency
G''	Loss modulus (made dimensionless by k_{Frankel}/r_c)
H	Asperity height
K	Bulk modulus (made dimensionless by k_{Frankel}/r_c)
L	Length of rigid rods
N	Number of cross-linking nodes in simulation box
P	Normal load (made dimensionless by $G \times$ apparent contact area)
Pe	Peclet number
R	Capsule outer radius
R_f	Final capsule radius
R_g	Radius of gyration
R_{g0}	Radius of gyration in the absence of network
R_i	Initial capsule radius
R_p	Stokes-Einstein radius of rigid particles
R_{rod}	Radius of rigid rods
R_{SE}	Stokes-Einstein radius
T	Temperature

T_{rel}	Elastomer relaxation time
U	Depth of adhesive potential well
U_b	Bending spring potential
U_{Frankel}	Frankel spring potential
U_{FENE}	FENE spring potential
V	Sliding velocity (made dimensionless by $\sqrt{k_B T/m}$)
$\overline{V}$	Rescaled sliding velocity (rescaled by $e^{-U/k_B T}$)
V_{box}	Volume of simulation box
$V_{filament}$	Filament volume
$V_{\max}$	Maximum friction sliding velocity
X , Y , and Z	Principal coordinate directions
α	Filament orientation
β	Constant
χ	Stokes drag coefficient for high aspect ratio filaments
δ	Phase shift
ε	Porosity
ϕ	Volume fraction
φ	Angle between vector representing spring direction and z axis
γ	Shear strain
γ_0	Amplitude of shear strain oscillations
γ^D	Coefficient of dissipative DPD force
η	Kinematic viscosity
λ	Asperity wavelength

μ	Friction coefficient
ν	Poisson's ratio
θ	Angle between two consecutive Frankel springs
ρ	Number density
ρ_e	Elastomer volume density
σ	Coefficient of random DPD force
τ_0	Amplitude of shear stress oscillations
τ_c	Characteristic time of capsule volume transition
τ_s	Characteristic time of solid sphere volume transition
τ_{xz}	Shear stress (made dimensionless by G)
ω	Frequency (made dimensionless by $r_c\sqrt{m/k_BT}$)
ω^D	Weight function of dissipative DPD force
ω^R	Weight function of random DPD force
ξ	Zero-mean Gaussian random variable with unit variance
ψ	Angle between vector representing spring direction and x axis
Δt	Time step
Δx	Lattice spacing in x direction
Δy	Lattice spacing in y direction
Δz	Lattice spacing in z direction
ΔV	Volume change
Λ	Coefficient of adhesive force interactions (made dimensionless by $k_{\text{Frankel}}r_c^{adh}$)
Θ	Deswelling ratio
Ω	Orientation tensor

List of Abbreviations

AFM	Atomic Force Microscopy
BD	Brownian Dynamics
DFT	Density Function Theory
DOX	Doxorubicin
DPD	Dissipative Particle Dynamics
ESEM	Environmental Scanning Electron Microscopy
FEM	Finite Element Method
FENE	Finitely extensible nonlinear elastic
FITC	Fluorescein Isothiocyanate
FLNa	Filamin A
HPC	High Performance Computing
INH	Isonicotinylhydrazine
LB	Lattice Boltzmann
MD	Molecular Dynamics
MEMS	Microelectromechanical Systems
MSD	Mean Square Displacement
NIPAAm	Poly-N-Isopropylacrylamide
NMR	Nuclear Magnetic Resonance
PAA	Polyacrylic Acid
PDMS	Polydimethylsiloxane
PEG	Polyethylene Glycol
PEM	Polymer Electrolyte Membrane
PEO	Polyethylene Oxide
PNIPAM	Poly-N-Isopropylacrylamide

PTMEG	Polytetramethylene Ether Glycol
PVA	Polyvinyl Alcohol
3D	Three Dimensional

SUMMARY

Polymer networks are an important class of materials that are ubiquitously found in natural, biological, and man-made systems. The complex mesoscale structure of these soft materials has made it difficult for researchers to fully explore their properties. In this dissertation, we introduce a coarse-grained computational model for permanently cross-linked polymer networks than can properly capture common properties of these materials. We use this model to study several practical problems involving dry and solvated networks. Specifically, we analyze the permeability and diffusivity of polymer networks under mechanical deformations, we examine the release of encapsulated solutes from microgel capsules during volume transitions, and we explore the complex tribological behavior of elastomers. Our simulations reveal that the network transport properties are defined by the network porosity and by the degree of network anisotropy due to mechanical deformations. In particular, the permeability of mechanically deformed networks can be predicted based on the alignment of network filaments that is characterized by a second order orientation tensor. Moreover, our numerical calculations demonstrate that responsive microcapsules can be effectively utilized for steady and pulsatile release of encapsulated solutes. We show that swollen gel capsules allow steady, diffusive release of nanoparticles and polymer chains, whereas gel deswelling causes burst-like discharge of solutes driven by an outward flow of the solvent initially enclosed within a shrinking capsule. We further demonstrate that this hydrodynamic release can be regulated by introducing rigid microscopic rods in the capsule interior. We also probe the effects of velocity, temperature, and normal load on the sliding of elastomers on smooth

and corrugated substrates. Our friction simulations predict a bell-shaped curve for the dependence of the friction coefficient on the sliding velocity. Our simulations also illustrate that at low sliding velocities, the friction decreases with an increase in the temperature. Overall, our findings improve the current understanding of the behavior of polymer networks in equilibrium and non-equilibrium conditions, which has important implications for synthesizing new drug delivery agents, designing tissue engineering systems, and developing novel methods for controlling the friction of elastomers.

CHAPTER 1

INTRODUCTION

1.1 Background and Context

Polymer networks are natural, synthetic, or hybrid natural-synthetic materials in which constituting polymer chains are all connected to each other either directly or via other connecting chains to form a three-dimensional solid-like structure (see Figure 1.1) [1-3]. These highly permeable, extremely flexible, and yet mechanically sturdy polymeric materials have found an increasingly large number of applications in today's state-of-the-art technologies. For instance, water-swellable polymer networks (hydrogels) that are sensitive to external stimuli are extensively used in technologically advanced areas such as optoelectronics, MEMS, and nanomedicine [4-8]. Triggered by an external stimulus such as variations in temperature, pH, solvent chemistry, light intensity, magnetic or electrical fields, hydrogels can absorb (swell) or expel solvent (deswell) and, as a result, change their volume by many times [9-14]. In most cases, the application of an external stimulus alters the relative strength of polymer-polymer and polymer-solvent interactions and, thereby, gives rise to internal stresses which cause the network to expand or shrink [15]. From a thermodynamic point of view, the network swelling is driven by the osmotic pressure resulting from the difference in the solvent chemical potential inside and outside of the network [16].

The high sensitivity of hydrogels to the environmental changes makes them especially attractive for drug delivery applications, in which delivery agents can effectively shield and protect encapsulated drugs until they reach the treatment site, and

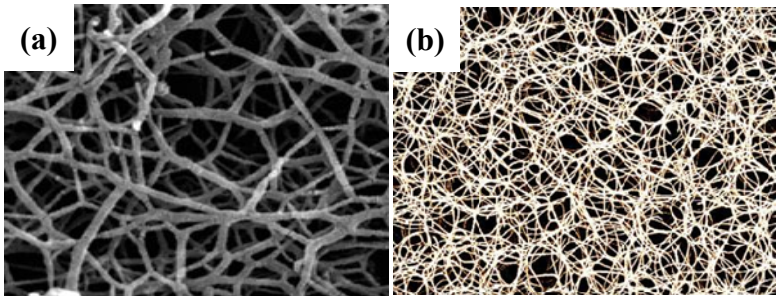

Figure 1.1 (a) A matrix of synthetic nanofibers and (b) an actin network. Reproduced from Refs. 2 and 3, respectively.

then discharge a predefined amount of the drug, thereby playing an active role in the disease therapy [17]. Indeed, researchers have successfully exploited polymer gels to create responsive micro- and nano-delivery agents that can release encapsulated drugs or other solutes on demand (see Figure 1.2) [17-27].

As another example, elastomers (physically or chemically cross-linked polymer networks [4]) are widely exploited in engineering applications including the construction of tires, wiper blades, flexible rotary seals, artificial organs, impact absorbers, dental implants, diaphragms, and solid lubricants for reciprocating machinery [28-31]. This is in part due to their ability to slide on rough, rigid surfaces with or without a lubricant. Distinct tribological properties of elastomers make them particularly useful in automotive and other industrial applications. These properties strongly depend on the characteristics of the substrate roughness [32]. Recent studies have shown that, indeed, micron scale geometrical patterning can be harnessed to regulate the elastomeric friction (see Figure 1.3) [33-36].

In addition to above applications, polymer networks are successfully employed as matrices for drug delivery [37], scaffolds for tissue engineering [38], and materials for soft contact lenses [39] and breast implants [40]. Furthermore, stimuli-responsive

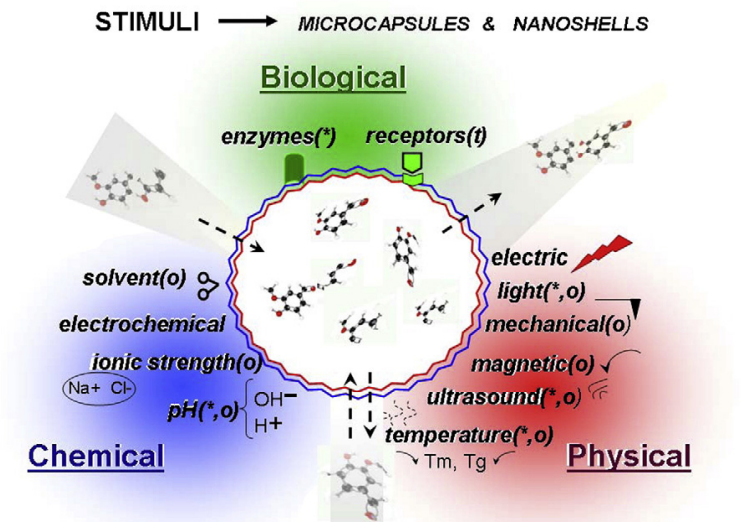

Figure 1.2 Schematic illustrating microcapsule loading and release triggered by chemical, physical, or biological stimuli. Reproduced from Ref. 27.

polymer gels are used to create micro-actuators [41], micro-robots [42-43], and different kinds of smart materials [44-45].

1.2 Previous Studies on Properties of Polymer Networks

The ever increasing importance of polymer networks requires an in-depth understanding of their properties. Indeed, using theory, computer simulations, and experiments, researchers have studied the mechanical, transport (*i.e.* permeability and diffusivity), swelling, and tribological properties of polymer networks [16, 46-84]. Here, we describe a few of the latest investigations. We begin with reviewing the studies focusing on mechanical properties followed by the discussion of studies considering transport, swelling, and frictional properties.

Head *et al*. [85] employed a model system of cross-linked, stiff filaments to examine the macroscopic response of cytoskeletal networks. They found that depending on the density of cross-linking and filament rigidity, mechanically loaded networks

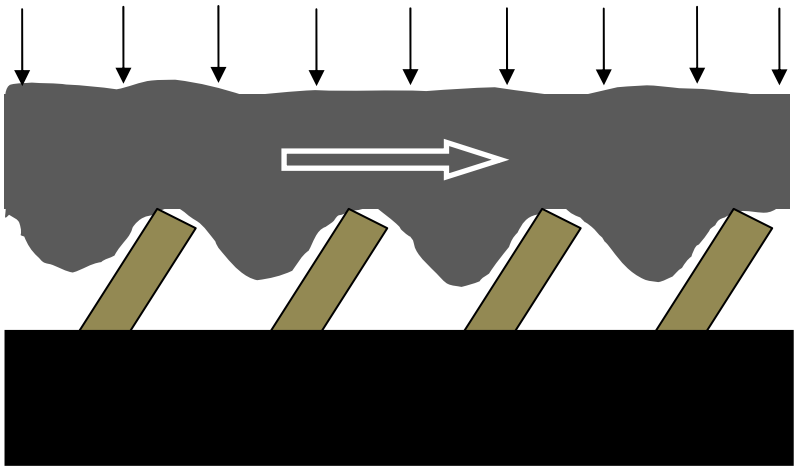

Figure 1.3 Schematic illustrating an elastomer sliding on an engineered rough surface.

undergo either affine or nonaffine deformations. They then characterized the conditions under which the transition occurs. Liu *et al*. [86] used a novel experimental technique to determine the local strain field in semiflexible polymer networks. By tracking embedded probe microparticles, they measured the uniformity of strain in networks under shear. Consistent with previous theoretical studies, their measurements showed that strain affinity strongly depends on the polymer length and cross-link density. Buxton and Clarke [87] performed a 3D computer simulation and identified a ‘‘bending-to-stretching’’ transition in the response of disordered elastic networks under stress. They found that the strain at which the transition occurs is a function of the average network connectivity.

Sander *et al*. [88] developed an image-based multiscale model to capture the anisotropy and heterogeneity of a cell-compacted collagen gel subjected to mechanical loads. Using their model, the authors investigated the relation between applied loads and cellular response, and predicted a heterogeneous network restructuring in which tensile and compressive fiber forces are produced to accommodate macroscopic displacements.

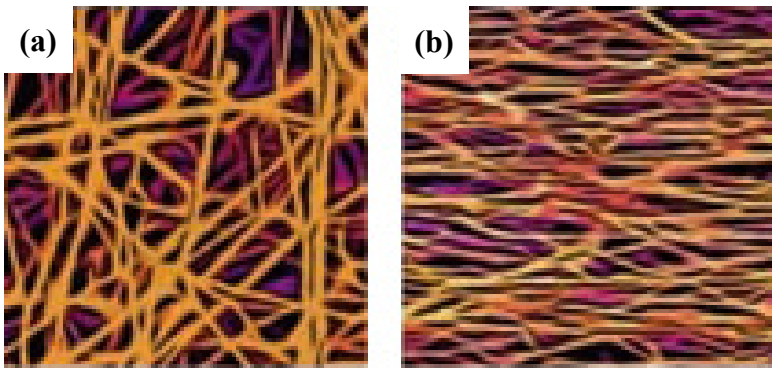

Figure 1.4 Fibrin gel at (a) unstressed and (b) stretched states. Reproduced from Ref. 62.

Koenderink *et al*. [89] synthesized an active polymer network in which processive molecular motors control the network rigidity. The system consists of actin filaments cross-linked by filamin A (FLNa) and contracted by bipolar filaments of muscle myosin II. They showed that the myosin motors stiffen the network by more than two orders of magnitude. They also demonstrated that the stiffening response closely mimics the effects of external stress applied by mechanical shear. Ulrich *et al*. [90] examined the elasticity of a highly cross-linked simple network consisting of randomly cross-linked harmonic springs. Their theoretical analysis showed that the network shear modulus is independent of the spring constant and the average length between cross-linking points, and is solely function of the cross-linking density. A comprehensive review of the recent works on the structure and dynamics of cross-linked actin and double networks are provided, respectively, by Lieleg *et al*. [91] and Gong [92].

Similar to mechanical properties, transport properties of networks have long been of interest to scientists and engineers. Tahir and Tafreshi [93] studied the influence of in-plane and through-plane fiber orientations on a fibrous network transverse permeability. They numerically solved the 3D Stokes equations and demonstrated that the transverse

permeability of a fibrous structure is independent of in-plane fiber orientation but increases with increasing deviation of the fiber through-plane angle from zero. Nabovati *et al*. [94] exploited the lattice Boltzmann method to examine the fluid flow in 3D random fibrous media and developed a semi-empirical constitutive model for the permeability of fibrous media. The authors also examined the influence of curvature and aspect ratio of fibers on the permeability. They found that curvature has a negligible effect, and that aspect ratio is only important for fibers with aspect ratio smaller than 6:1, in which case the permeability increases with increasing aspect ratio. A comprehensive review of experimental and theoretical data on Newtonian fluid flows through different types of porous media is available elsewhere [95].

Flow of non-Newtonian fluids through porous media and polymer networks have been studied by several researchers. Morais *et al*. [96] investigated non-Newtonian fluid flows through a disordered porous medium by direct numerical simulations. They found that their results for power-law fluids can be described by a single universal curve over a broad range of Reynolds numbers and power-law exponents. The authors also considered the flow of Bingham fluids described in terms of the Herschel-Bulkley model. In this case, their simulations revealed that the interplay of the disordered geometry of the pore space, the fluid rheological properties, and the inertial effects leads to a substantial enhancement of macroscopic hydraulic permeability at intermediate Reynolds numbers. Sochi [97] presented a review of the single-phase flow of non-Newtonian fluids in porous media.

Diffusion of various solutes, such as rigid particles and linear macromolecules, has been extensively investigated to understand the fundamentals of transport through

cross-linked biological and synthetic networks. Liu *et al*. [98] experimentally observed that sufficiently small molecules adopt an approximately spherical conformation when diffusing through a gel matrix, whereas larger molecules are forced to migrate in a snake-like fashion. They also found that molecules of intermediate size can temporarily get trapped in the largest matrix pores, where the molecule can extend and, thereby, maximizes its conformational entropy. The authors suggested that this "entropic trapping" leads to an increased dependence of diffusion rate on molecular size. Seiffert and Oppermann [99] carried out a series of experiments and measured the diffusion of linear macromolecules and spherical particles in semi-dilute polymer solutions and polymer networks. They found, in contrast to the prediction of the hydrodynamic scaling model [49-50], that the diffusion of flexible polymers and rigid particles having comparable sizes is not identical. Nevertheless, they indicated that the scaling model provides a reasonable fit to individual sets of experimental data. Cu and Saltzman [57] provided an extensive review of different mathematical models and experimental methods employed to measure the diffusion through polymer networks and specifically through the mucus gel for drug delivery purposes.

Swelling kinetics of polymer networks has been the subject of many recent theoretical and experimental studies [16, 70-84]. Zhang *et al*. [79] developed a finite element model to simulate the large deformation and fluid transport during swelling/deswelling of polymer gels. The authors successfully used their model to study several time-dependent processes in swelling gels, such as draining of fully swollen gels due to weight, free swelling-induced surface instability, and buckling pattern formation due to partial confinement. Keener *et al*. [81] presented a model for the swelling kinetics

of gels that incorporates the free energy including the polymer standard free energy. The authors employed their model to study the effect of free energy parameters on the swelling kinetics and stable states and sizes of the swollen gel and demonstrated that the theories ignoring the polymer standard free energy cannot properly describe the swelling kinetics or equilibrium states.

Jha *et al*. [75] employed a theoretically informed Monte Carlo simulation to examine volume phase transitions of polymeric nanogels. The authors modeled nanogels as regular networks of Gaussian strands discretized with coarse-grained polymer beads, and analyzed the effects of degree of crosslinking, solvent quality, and charge fraction of polymer backbone on the volume phase transition behavior of nanogels. The results of their simulations indicated that their coarse-grained model can capture the universal features of volume phase transition phenomenon as observed in swelling experiments. These features include higher gel swelling with an increase in hydrophilicity and degree of ionization of polymer backbone, and a decrease in crosslink density of the nanogel. Moreover, their model predicted a discontinuous volume phase transition in the case of ionic nanogels. Yashin and Balazs [80] developed a mesoscale model to study reactive gels that undergoe periodic volume changes due to the self-oscillatory Belousov–Zhabotinsky reaction. Traveling waves and different dynamical patterns were discovered that may be useful for mechano-sensing applications and self-propulsion.

Caldorera-Moore *et al*. [76] used atomic force microscopy (AFM) and environmental scanning electron microscopy (ESEM), to characterize the swelling behavior of nano-imprinted hydrogel particles of different sizes and aspect ratios. Their studies showed that the swelling behavior of imprinted gel particles with characteristic

length of 100nm or less is a function of particle size and deviates from the bulk behavior. The authors also developed a model based on FEM and field theory to further support their observations. Wahrmund *et al*. [82] examined the swelling kinetics of micron-sized monodisperse poly-N-isopropylacrylamide (PNIPAM) hydrogel capsules. The authors varied the temperate and measured the inner and outer radii of the microgel capsules as a function of time to characterize their swelling behavior. The results of their experiment indicated that the characteristic swelling time of a gel shell is proportional to the square of the outer radius and is not a function of the capsule thickness. The authors supported their experiment by developing a simple model describing the swelling kinetics of microgel shells.

Not only the mechanical and transport properties of polymer networks, but also their frictional properties have received considerable attention over the past few decades. Researchers have developed theories and performed experiments to scrutinize the tribological behavior of dry and solvated polymer networks [28, 32, 100-124]. For instance, Gong and Osada [120] proposed a model based on the repulsion and adsorption theory at a solid surface to describe the frictional force produced when a polymer gel slides on a solid surface. The authors combined their model with scaling arguments to derive general relationships for the frictional force as a function of the normal load, sliding velocity, polymer volume fraction, and elastic modulus of the gel. The results of this model show that when the interactions are repulsive, friction is due to the viscous flow of solvent at the interface and, therefore, is proportional to the sliding velocity and the normal pressure provided that the pressure is smaller than the elastic modulus of the gel. For the attractive interactions, the model predicts that in addition to the

hydrodynamic friction, the force required to detach the adsorbed chains from the substrate contributes to the friction, too. The authors applied their model to several test cases and found good agreement between their theoretical results and certain experimental observations. In their later experimental work, Gong *et al*. [121] investigated the friction of several kinds of hydrogels sliding on glass and Teflon plates both in air and water. Their experimental measurements revealed that the friction force and its relation with the normal load vary depending on the chemical structure of gels, surface properties of the opposing substrates, and the measurement conditions. They explained the difference in tribological behavior of gels in terms of the surface interaction between the polymer network and solid surfaces. To support their explanation, they measured the adhesion between glass particles and gels, and showed that it correlates very well with the friction.

Du *et al*. [114] examined the friction of a polyvinyl alcohol (PVA) gel sliding against a glass surface in dilute polyethylene oxide (PEO) aqueous solutions with various molecular weights and concentrations. They observed that frictional stress in PEO 2E4 solutions is lower than in pure water. They also saw that the friction decreases with an increase in the PEO concentration and reaches a minimum at the crossover concentration. However, they noticed that in higher molecular weight solutions this friction reduction is only observed for very dilute concentrations, and the frictional stress in higher concentration is higher than that in pure water. The authors showed that at fast sliding velocities, all the friction curves in dilute PEO solution collapse into the pure water curve, independent of the molecular weight and concentration of PEO. Their results revealed that in the low sliding velocity region, where adsorption of PVA gel on glass

plays the dominant role in friction, PEO chains screen the adsorption of PVA chains to the glass surface. In the fast sliding velocity region, on the other hand, liquid lubrication prevails due to either the extensive stretching of PEO chains or formation of a deplete layer near the glass surface.

Finally, Chang *et al*. [115] explored the effect of swelling/deswelling phase transition on the tribological properties of pNIPAAm hydrogels. Using experimental measurements, they showed that, at small shear rates, gels in the collapsed state exhibit significantly higher friction than swollen gels. The authors attributed the difference in friction to changes in the surface roughness, adhesive interactions, and chain entanglements at the gel-gel interface. Regardless of the origin, they demonstrated that the changes in friction, triggered by an external stimulus, are reversible.

1.3 Scope and Objectives

Our literature survey in the previous section reveals that the majority of studies examined the properties of polymer networks under ideal conditions. For example, there are relatively few studies that considered the transport properties of polymer networks under a mechanical load or explored mass transfer through the networks during the volume transition. Investigations concerning the mechanical response of polymer networks in non-equilibrium conditions are also scarce. However, in many real-world applications, polymer networks are subject to external/internal stresses (see for example Figure 1.4) and/or function in a non-equilibrium state.

The study of practical problems involving polymer networks usually requires accommodating several time and length scales. Moreover, there often exist complex geometrical domains where mechanical and fluid phenomena are coupled. The multi-

scale, multi-physics nature of systems in which polymer networks play a primary role makes it extremely difficult to develop comprehensive analytical models. Also, experimental approaches are typically very costly, time consuming and require significant effort. Therefore, there is a critical need to develop rigorous computational approaches capable of describing coupled phenomena associated with the applications of polymer networks. Recent advances in the high-performance computing provide new opportunities for developing such models that can be employed not only for investigating the static and dynamic properties of polymer networks, but also for exploring the entire operation of systems whose performance depend on the function of polymer networks. The synergistic combination of these models with ever-improving experimental methods can answer fundamental questions about the properties of polymer networks and facilitate their applications in emerging technologies.

The central objective of this Ph.D. dissertation is to develop a fully-coupled three dimensional model for permanently cross-linked, semiflexible polymer networks and use it to study (1) the permeability and diffusivity of mechanically loaded polymer networks; (2) to explore transport of encapsulated solutes across the membrane of microgel capsules during swelling and deswelling volume transitions; and (3) to probe the tribological behavior of elastomers sliding on smooth and grooved surfaces.

The results of our studies reveal important and highly-needed information about the relation between the mechanical deformation of polymer networks and the change in diffusive and convective transport of solutes. This information not only gives us a fundamental insight into the transport processes in anisotropic random networks taking place at the micro/nano scale, but also yields engineering guidelines for designing a

whole host of new systems and devices in which polymer networks are harnessed for solute transport, separation, sensing, and micromechanical actuation. Our calculations of release from responsive microgel capsules disclose how the gel transport properties change due to the network swelling/deswelling and provide a new approach for regulating the release of drugs from drug delivery micro-carriers by controlling the membrane pore size. Furthermore, our simulations of elastomeric friction on engineered rough substrates give insights into the complex tribological properties of cross-linked polymer networks and unveil the possibility of harnessing directional surfaces to alter the friction and reduce wear in a controllable and predictable manner. Finally, our three dimensional fully-coupled model of cross-linked polymer networks provides a foundation for future studies on a broad range of problems in engineering, medicine, and biology that involve active and responsive polymer networks.

The remaining chapters of this dissertation are organized as follows. In the next chapter, we introduce our model and characterize its properties. In chapter 3, we present the results of our simulations for convective and diffusive transport through networks under axial and shear loadings. In chapter 4, we describe the controlled release of particles and linear macromolecules from responsive microgel capsules. In chapter 5, we report our findings regarding the friction of elastomers on smooth and grooved surfaces. We conclude with chapter 6 where we summarize our results and discuss future research directions.

CHAPTER 2

METHODOLOGY

2.1 Introduction

Computationally, one could model polymer networks in three different ways; *i.e*. using molecular dynamics (MD), continuum methods, or mesoscale models (Figure 2.1). Each of these simulation techniques has their own benefits and drawbacks. While continuum-based methods such as finite-difference, finite-element, and finite-volume accurately capture phenomena at the macroscale, they fail to correctly model the micromechanics and the complex structure of polymer networks [87, 125-127]. On the other hand, molecular dynamics simulations can very accurately model phenomena taking place at a few nanometers in length and a few nanoseconds in time. However, they become computationally prohibitively expensive when they are employed to simulate larger complex systems [126]. A way to tackle this issue in MD is to use "pseudo-atoms" to represent groups of atoms instead of explicitly representing every atom of the system (see Figure 2.2). The coarse-graining or reduced representation allows simulation of microscale phenomena at larger time and length scales comparing to what can be modeled by conventional all-atom MD.

Over the past few decades, several mesoscale coarse-grained simulation methods have been developed to bridge the gap between the continuum methods and all-atom molecular dynamics simulations [126]. Among those are the Brownian dynamics (BD),

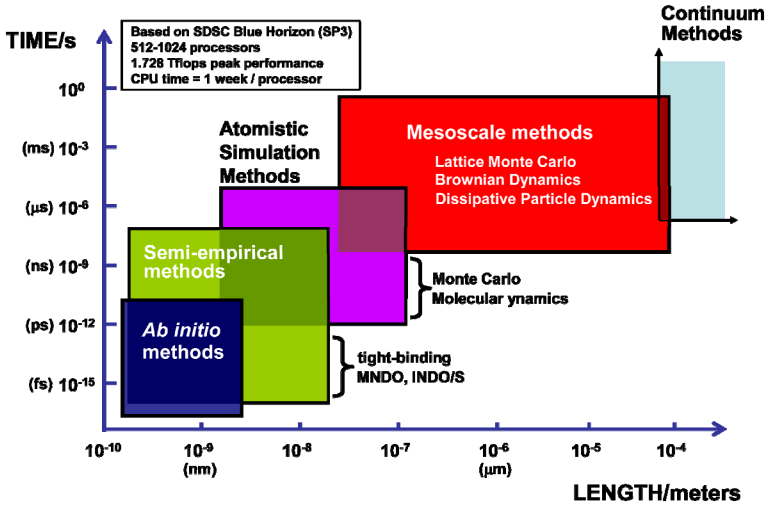

Figure 2.1 Schematic illustrating applicability ranges of various simulation techniques. Reproduced from Prof. C. Heath Turner lecture notes (see http://unix.eng.ua.edu/~checlass/Simulation/l07.ppt).

dissipative particle dynamics (DPD), lattice Boltzmann (LB), and the density functional theory (DFT).

Unlike conventional continuum approaches that solve a set of partial differential equations, the majority of these mesoscopic methods follow the evolution of a many-body system to simulate the governing equations. This makes them particularly effective for massive parallel high-performance computing (HPC) and, therefore, suitable for the computationally demanding task of modeling the complex behavior of soft materials such as polymer networks.

The choice of a particular simulation technique for a given problem depends on the nature of the interactions between the elements of the system and the appropriate level of coarse-graining. Here, we employ the dissipative particle dynamics (DPD), a particle-based computational method that can effectively capture the salient features of the polymer network architecture and, at the same time, can properly model the relevant

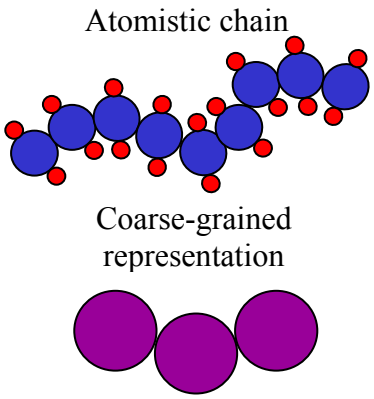

Figure 2.2 Coarse-grained representation of a polymer chain.

hydrodynamic effects and thermal fluctuations. In the following sections, we first introduce DPD and then we describe our methodology and validation studies.

2.2 Dissipative Particle Dynamics

Dissipative particle dynamics [15, 128] is a coarse-grained simulation technique that employs a momentum-conserving thermostat and soft repulsive interactions among beads representing clusters of molecules (Figure 2.2). This allows for simulations of physical phenomena occurring at relatively large time and spatial scales, while capturing the relevant hydrodynamic effects. Indeed, DPD has been successfully employed for simulating the dynamics of soft matter systems including those that involve polymers and nanoparticles dispersed in Newtonian incompressible fluids [126, 129-144].

For instance, Filipovic *et al*. [130] used DPD to examine the motion of circular and elliptical particles in a 2D shear laminar flow. Chen *et al*. [132] exploited DPD to investigate the steady-state and transient dynamics of polymer drops under shear in a microchannel. Alexeev *et al*. [133] employed DPD to probe interactions between lipid bilayer membranes and Janus nanoparticles. Using DPD, Fedosov *et al*. [134] studied the

flow of dilute polymer solutions in micro and nanochannels. Lastly, Fan *et al*. [137] simulated the flow of DNA suspensions in microchannels by DPD.

In DPD, the time evolution of the many-body system obeys the Newton's second law $m_i\, d\mathbf{v}_i/dt = \mathbf{f}_i$, where $\mathbf{v}_i$ and $\mathbf{f}_i$ are, respectively, the velocity and force on a bead i with mass m_i, and t is time. The equations of motion are integrated using the velocity-Verlet algorithm [15]. The force on a bead is $\mathbf{f}_i = \sum_j \left(\mathbf{F}_{ij}^C + \mathbf{F}_{ij}^D + \mathbf{F}_{ij}^R\right)$, where the sum runs over all beads j within a cutoff radius r_c around the bead i. The conservative force is given by $\mathbf{F}_{ij}^C = a_{ij}\left(1-\hat{r}_{ij}\right)\hat{\mathbf{r}}_{ij}$, where a_{ij} is the repulsion between beads i and j, $\hat{r}_{ij} = r_{ij}/r_c$ and $\hat{\mathbf{r}}_{ij} = \mathbf{r}_{ij}/r_{ij}$ with $r_{ij} = \left|\mathbf{r}_i - \mathbf{r}_j\right|$. Here, $\mathbf{r}_i$ is the position vector of bead i. The dissipative force is $\mathbf{F}_{ij}^D = -\gamma_{ij}^D\, \omega^D\left(\hat{\mathbf{r}}_{ij}\cdot\mathbf{v}_{ij}\right)\hat{\mathbf{r}}_{ij}$ and the random force is $\mathbf{F}_{ij}^R = \sigma_{ij}\, \omega^R\, \xi_{ij}\hat{\mathbf{r}}_{ij}\sqrt{dt}$, where $\mathbf{v}_{ij} = \mathbf{v}_i - \mathbf{v}_j$ and ξ_{ij} is a zero-mean Gaussian random variable of unit variance with $\xi_{ij} = \xi_{ji}$. The coefficients γ_{ij}^D and $\sigma_{ij}^2 = 2k_B T\gamma_{ij}^D$ determine the strength of dissipative and random forces, where k_B is the Boltzmann constant and T is the temperature of the system. Moreover, the weight functions ω^D and ω^R are related via $\omega^D = \left(\omega^R\right)^2$. The relations between the weight functions and the strength of dissipative and random forces are set to ensure the thermodynamic equilibrium [145]. The generalized form of the weight function ω^R is given by $\omega^R = (1-\hat{r}_{ij})^p$ with $p = 1$ for the standard DPD model [137].

Unbounded systems in DPD are modeled using periodic boundary conditions. However, there is more than one way to simulate systems involving physical boundaries. Solid surfaces can be modeled indirectly by modifying the periodic boundary conditions

[146-147]. Alternatively, they can be accounted for by locally "freezing" a cluster of DPD beads that represent the surface geometry [146-147]. The former approach is limited to simple geometries whereas the latter can be applied to more complex systems. For example, it was shown that, when combined with a particle reflection rule at the fluid-solid interface, the freezing method can effectively be used to satisfy the no-slip condition [135, 146-149]. Here, we use periodic boundary conditions to simulate phenomena taking place in the bulk and freeze DPD beads to model stationary solid walls.

2.3 Model for Linear Macromolecules and Rigid Objects

We model polymer macromolecules as flexible chains of DPD beads connected sequentially by finitely extensible nonlinear elastic (FENE) springs. The FENE potential is given by $U_{\mathrm{FENE}} = -k_{\mathrm{FENE}} r_{\max}^2 \ln[1-(|\mathbf{r}_i - \mathbf{r}_j|/r_{\max})^2]$, where k_{FENE} is the stretching constant and $r_{\max}$ is the maximum spring extension. This model does not explicitly account for chain uncrossability. However, as reported earlier [134, 150], this is not a critical issue especially when we consider dilute solutions where $c_{chain} << c_{chain}^*$. Here, c_{chain} is the number density of polymer chains and $c_{chain}^* = \left(4\pi R_{g0}^3/3\right)^{-1}$ is the overlapping concentration with R_{g0} being the bulk gyration radius of chains [151].

We model rigid objects by clustering DPD beads to form the desired shape and then considering the cluster as an independent object. Since the distance between the beads comprising a single object are kept constant, the object obeys the dynamics of rigid bodies. Specifically, we construct rigid particles from beads arranged in hexagonal close-

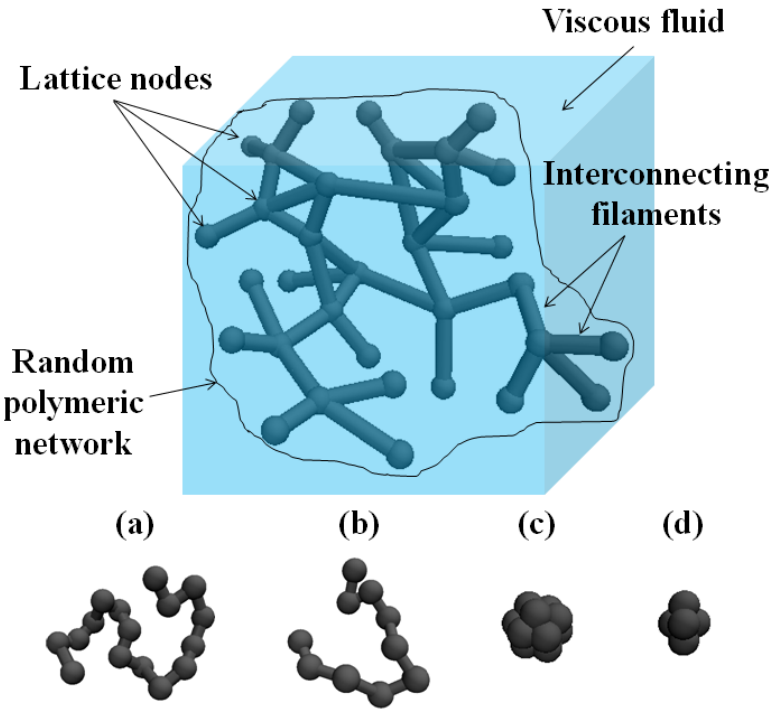

Figure 2.3 Schematic illustrating system components within a periodic simulation box. Insets (a) and (b) show 16-bead and 10-bead polymer chains, respectively. Insets (c) and (d) show, respectively, 13-bead and 5-bead hexagonal closed-packed aggregates representing nanoparticles. Reproduced from Ref. 136.

packed spherical aggregates, and we build immobile solid walls by freezing beads organized in layers of square lattice.

2.4 Polymer Network Model

We use a random lattice of interconnecting elastic filaments to capture the mechanics of disordered polymer networks [87]. The flexible filaments are formed from DPD particles connected by Frankel springs with a potential $U_{\text{Frankel}} = k_{\text{Frankel}}(|\mathbf{r}_i - \mathbf{r}_j| - r_{eq})^2/2$. Here, k_{Frankel} and r_{eq} are the spring constant and equilibrium length, respectively. Additionally, we include a bending potential $U_b = k_b(1+\cos\theta)$, where k_b is the bending stiffness and θ is the angle between two

consecutive pairs of beads. Bending and stretching spring constants can be chosen to match the ratio between bending/stretching and thermal energy of filaments. We note that the number of beads n_f in a filament with the length of l_f is given by $1+l_f/r_{eq}$ where r_{eq} can be tuned to ensure the correct solvent-filament and solute-filament interactions.

We build the cubic network in two steps (Figure 2.3). We first randomly distribute N cross-linking nodes inside the computational domain. Then, we connect each node with C_{ave} closest nodes that are located within a cutoff radius which is set to prevent the formation of excessively long filaments. The resulting average network connectivity deviates from the value of C_{ave} by less than one percent. Thus, we construct polymer networks that are characterized by the number of cross-linking nodes N and the average connectivity C_{ave}. To create non-cubic networks, we first generate a bigger cubic network and then remove the beads and connections that are outside the geometry of interest. Given the importance of porosity in analyzing mechanical and transport properties of porous media, we further characterize our network by defining its porosity as $\varepsilon = 1 - V_{filaments}/V_{box}$, where V_{box} is the total volume of the simulation domain and $V_{filament} = 4/3\, n_{total} \pi R_{SE}^3$ is the volume occupied by the filaments in which $R_{SE} \approx 0.209$ is the Stokes-Einstein radius of DPD beads [152] and n_{total} is the total number of DPD beads used to build the network (n_{total} is different from the number of lattice seed nodes N). When we calculate the porosity, some of the filaments may overlap and, thus, the resulting value exceeds the real network porosity by a few percent. Since the total number of filaments in the network is equal to $N C_{ave}/2$ and the average filaments length varies proportional to $\left(N/V_{box}\right)^{-1/3}\left(C_{ave}+C_0\right)$, where C_0 is a constant related to the

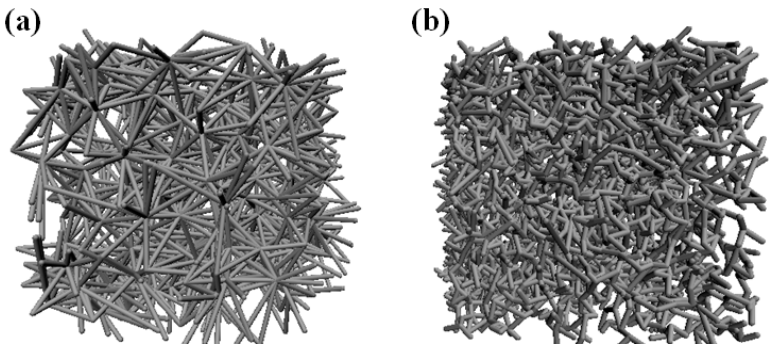

Figure 2.4 Networks with porosity $\varepsilon = 0.8$ and different internal structures: (a) $N = 2000$ and $C_{ave} = 3$; (b) $N = 250$ and $C_{ave} = 12$. Reproduced from Ref. 136.

average distance between lattice nodes $\left(N/V_{box}\right)^{-1/3} C_0$, we can estimate the network porosity using the following equation $\varepsilon = 1 - \pi R_{SE}^2 \left(N/V_{box}\right)^{2/3} C_{ave}\left(A\,C_{ave} + B\right)$. We find that for networks considered in our studies $A = 8.6\times10^{-3}$ and $B = 0.171$. Figures 2.4a and 2.4b show two networks constructed with different values of N and C_{ave}. Here, we choose the network parameters such that the porosity ε is roughly 0.8 for both networks. As we show in the following, despite the notable difference in their internal structures, these networks exhibit similar transport properties.

Below, we characterize the transport, mechanical, and swelling properties of our model network. We first examine its permeability and diffusivity in unstressed state and then probe its elastic and viscoelastic response. Finally, we introduce an approach to simulate the volume transition and use it to evaluate the swelling kinetics of our network.

2.4.1 Transport Properties

We measure the transport properties by calculating the permeability, self-diffusivity, and particle/chain diffusivity in networks with different N and C_{ave} (Figures 2.5 and 2.6). We carry out simulations in a periodic box that encompasses a viscous

solvent, an elastic polymer network, and diffusive objects such as polymer chains and rigid particles (Figure 2.3). The domain dimensions are $10\times10\times10$ in the x, y, and z directions, respectively. This is to ensure that the domain is greater than the minimum box size of $14\sqrt{k}$, as suggested by Clague and Phillips [51] based on the Brinkman screening length criterion. Here, k is the network permeability. We also set the time step $\Delta t = 0.01$, $p = 1$, $m = 1$, $r_c = 1$, $\gamma^D = 4.5$, $a = 25$, $k_{\text{Frankel}} = 200$, $k_b = 2.5$, $k_{\text{FENE}} = 10$, $r_{eq} = 0.418$, $r_{\max} = 2$, $k_B T = 1$ and the solvent number density $\rho = 3$ yielding the solvent kinematic viscosity η equal to 0.283. Unless specified otherwise, all dimensional values are given in DPD units.

We further use polymer chains of 10 and 16 DPD beads (Figures 2.3a and 2.3b) with gyration radius of, respectively, $R_{g0} \approx 0.97$ and $R_{g0} \approx 1.33$, as calculated from the equilibrium simulations. We also construct rigid particles from 5 and 13 DPD beads with the Stokes-Einstein radius of $R_p \approx 0.45$ and $R_p \approx 0.7$ [152], respectively (Figures 2.3c and 2.3d).

Here, we first equilibrate the network without solvent, and then we fix the network geometry and introduce solvent. In the permeability calculations shown in Figure 2.5, we apply an external body force $\mathbf{F}_{external} = 0.01\left(\hat{\mathbf{e}}_x + \hat{\mathbf{e}}_y + \hat{\mathbf{e}}_z\right)$ to drive the fluid flow through the network. Here, $\hat{\mathbf{e}}_x$, $\hat{\mathbf{e}}_y$, and $\hat{\mathbf{e}}_z$ are unit vectors in the x, y, and z directions, respectively. We run the simulations for 3.2×10^5 time steps and evaluate the components of volume-averaged flow velocity, $\langle u \rangle$, in the x, y, and z directions. Next, we use Darcy's law $k = \sqrt{3}\langle u \rangle \nu / \left|\mathbf{F}_{external}\right|$ to find the permeability in each direction [48].

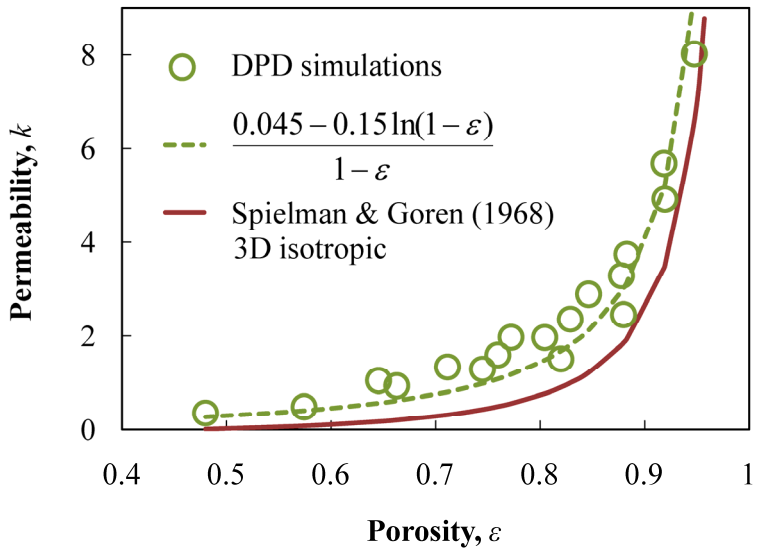

Figure 2.5 Permeability as a function of porosity in 3D isotropic random polymer networks. The network parameters are $N = 250, 500, 1000$ and $C_{ave} = 4, 6, 8, 10, 12, 14$. Reproduced from Ref. 136.

Finally, we average the permeability results over symmetric directions within the network and non-dimensionalize the average by dividing it with the square of filament radius, which is equal to the Stokes-Einstein radius of a DPD particle.

We find good agreement between our permeability-porosity results for networks with different N and C_{ave} and the results of Spielman and Goren [153] for isotropic porous media (Figure 2.5). Slightly higher permeability predicted by our model can be attributed to a somewhat lower drag on filaments constructed from spheres as compared to cylindrical filaments [154]. Figure 2.5 also demonstrates that the permeability of a random filament network depends solely on the network volume fraction and is not a function of the network internal structure. This is in agreement with previously reported results [59].

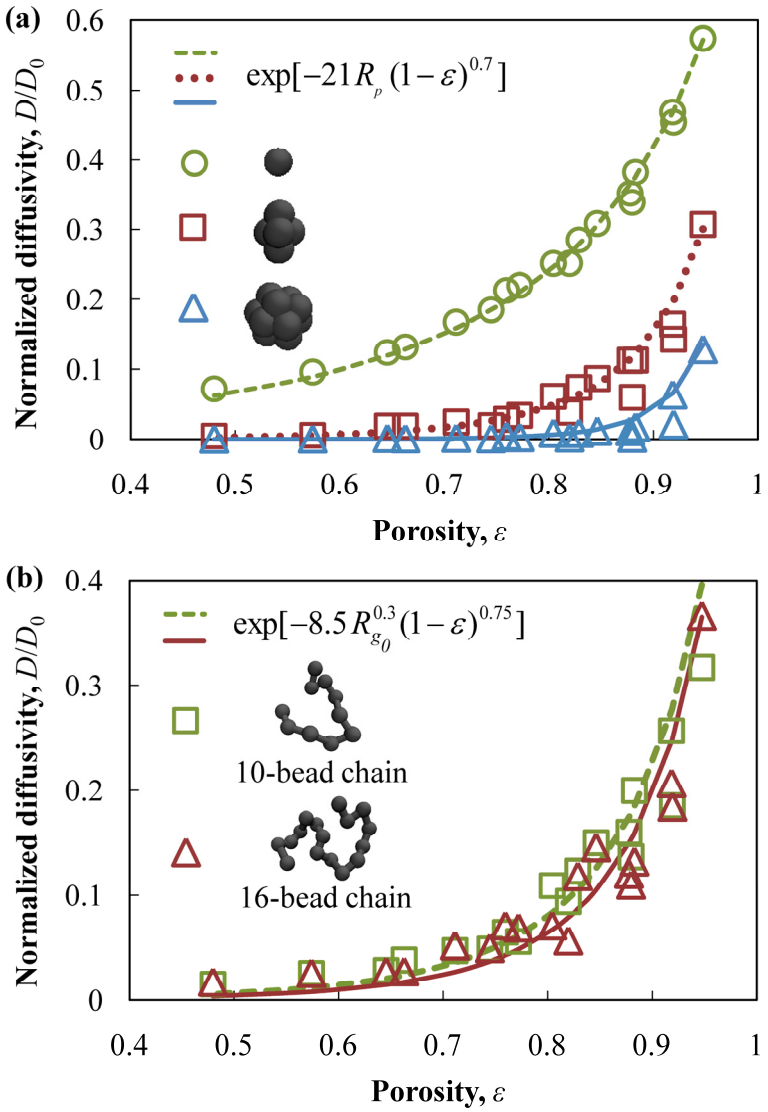

Figure 2.6 Diffusivity of (a) solvent particles (self-diffusivity), rigid particles with radius $R_{SE} \approx 0.45$ and $R_{SE} \approx 0.7$ and (b) 10 and 16-bead polymer chains in 3D isotropic random polymer networks as a function of network porosity. The network parameters are $N = 250, 500, 1000$ and $C_{ave} = 4, 6, 8, 10, 12, 14$. Reproduced from Ref. 136.

To evaluate network diffusivity (Figure 2.6), we introduce 30 diffusive objects (chains or particles) that are initially randomly distributed in the solvent. We continue the simulations for 8×10^5 time steps to collect sufficient statistics regarding the entities' diffusion. We then calculate the diffusion coefficients using the long-time, mean-square

displacement (MSD) relation of Einstein $D = C\left\langle \left| r(t) - r(0) \right|^2 \right\rangle / t$, where $\langle ... \rangle$ represents the ensemble average, C is a constant, and $r(t) - r(0)$ is the object position at time t relative to its original position. Calculated diffusivities are normalized by the corresponding diffusivities in the absence of the network.

Figures 2.6a presents the results of DPD simulation for retarded diffusion of solvent particles (self-diffusion) and rigid particle of radius $R_p \approx 0.45$ and $R_p \approx 0.7$. The diffusion of 10 and 16-bead polymer chains with a radius of gyration equal to $R_{g0} \approx 0.97$ and $R_{g0} \approx 1.33$, respectively, is shown in Figure 2.6b. Figure 2.6 show excellent agreement between our simulations and the experiments of Seiffert and Oppermann [99]. We also find that our simulation results are in close agreement with the hydrodynamic scaling model [49-50] for the diffusion of rigid particles and linear macromolecules in stationary random polymer networks. The smaller value of the scaling exponent for chains indicates weaker dependence of the diffusion on the polymer radius of gyration (see Figure 2.6a and Figure 2.6b). Moreover, in agreement with previous studies [57, 99], our results show that the diffusion coefficient of solid particles is smaller than that of flexible polymers with a similar coil size. This is related to different mechanisms controlling diffusion of solid objects and flexible polymers. Unlike solid particles that have a constant outer radius, the radius of gyration of polymeric chains changes when a chain diffuses through a network. Figure 2.7 illustrates that the radius of gyration decreases with decreasing the network porosity for greater ε and approaches to a constant value as the network becomes denser. The reduction in radius of gyration of

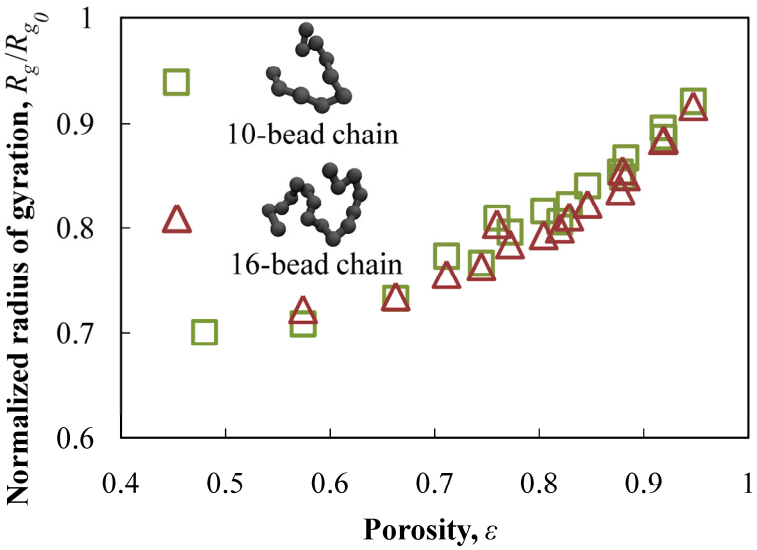

Figure 2.7 Radius of gyration as a function of network porosity for 10- and 16-bead polymer chains in 3D isotropic random polymer networks. The network parameters are $N = 250, 500, 1000$ and $C_{ave} = 4, 6, 8, 10, 12, 14$. Reproduced from Ref. 136.

chain enhances their hindered diffusion in polymer networks and, therefore, yields greater diffusivity comparing to rigid particles.

2.4.2 Mechanical Properties

We evaluate the mechanical properties of our network by measuring its elastic and viscoelastic response to, respectively, constant and oscillatory deformations. The elastic moduli are calculated using linear elasticity relations. To this end, we impose a uniform strain and compute the corresponding stress tensor using the Irvin-Kirkwood method [155]. Specifically, we apply a shear strain of $\gamma = 0.2$ to gauge the shear modulus G and reduce the size of our simulation box to $9.75 \times 9.75 \times 9.75$ to determine the bulk modulus K of the network. Having G and K, we calculate the Poisson's ratio as $\nu = (3K - 2G)/2(3K + G)$. The results of our simulations are presented in Figure 2.8.

Here, we normalize the elastic moduli by k_{Frankel}/r_c and plot them along with the Poisson's ratio versus the network porosity.

Figure 2.8a shows that the shear modulus increases linearly with the network volume fraction $\phi = 1 - \varepsilon$. This finding is in agreement with the results of Buxton and Clarke [87] in the stretching dominated regime, and further implies that the shear modulus scales with the number of cross-linking nodes as $N^{2/3}$ and with the average connectivity as $C_{ave}\left(AC_{ave} + B\right)$. Unlike the shear modulus, the bulk modulus does not change linearly with ϕ and, instead, scales with $\phi^{3/2}$ (see Figure 2.8b). The departure from the linear dependency could be attributed to the background fluid. While the presence of the DPD solvent has little or no effect on the shear strength of the network, it does influence the compressibility of the system and, therefore, the network bulk modulus. The effect of host solvent on the bulk modulus is not the same for all networks and becomes more pronounced for networks with lower porosity. Figure 2.8c shows that, indeed, the network Poisson's ratio approaches 0.5 (becomes almost incompressible) as the network volume fraction falls below 0.05. Although, the variations of network Poisson's ratio is very small, it is enough to cause the deviation from the linear behavior in the $G - \varepsilon$ curve.

We also characterize the nonlinear response of our network. To this end, we apply shear strains of different magnitude to a sample network with $N = 500$ and $C_{ave} = 8$, and measure the corresponding stress. Figure 2.9 shows the dimensionless shear stress τ as a function of applied strain γ. The dashed line in Figure 2.9 represents the linear response. In accordance with previous studies [64, 156-157], we see that the shear stress significantly deviates from the linear behavior and shows a strong strain stiffening.

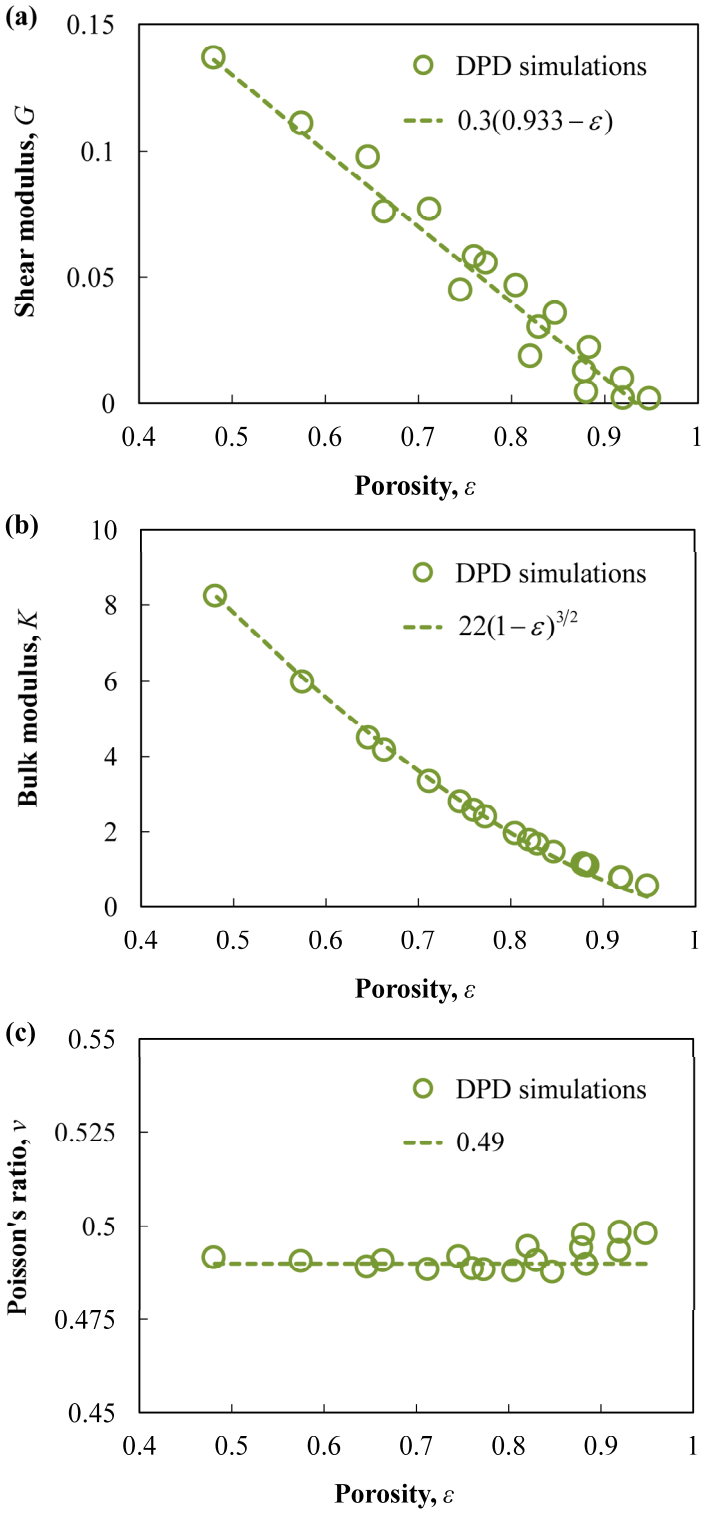

Figure 2.8 (a) Shear modulus, (b) bulk modulus, and (c) Poisson's ratio versus network porosity. The network parameters are $N = 250, 500, 1000$ and $C_{ave} = 4, 6, 8, 10, 12, 14$.

Furthermore, we see that shear stress initially scales with $\gamma^{1.3}$ and later on becomes

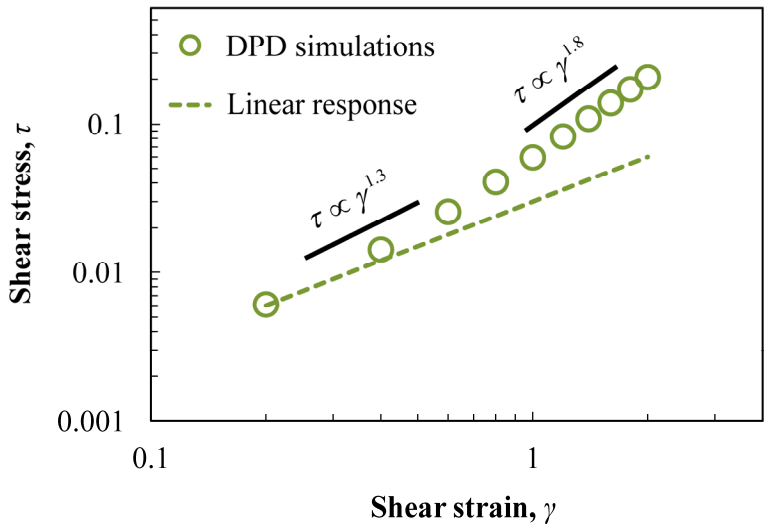

Figure 2.9 Shear stress versus applied strain for a network with $N = 500$ and $C_{ave} = 8$.

proportional to $\gamma^{1.8}$. This is in qualitative agreement with the observations of Stein *et al.* for collagen gels [156].

To evaluate viscoelastic properties of our polymer network, we apply a uniform oscillatory shear strain of the form $\gamma(t) = \gamma_0 \sin \omega t$ to the network and calculate the shear stress developed as a result of the applied strain. We impose an affine sinusoidal shear by exerting an additional force in the x direction to all DPD beads in our periodic simulation box. The force is given by $\mathbf{F}_i^A = m r_{i,z}\, d^2\gamma(t)/dt^2\, \hat{\mathbf{e}}_x$ where $r_{i,z}$ is the z coordinate of the ith bead. We also apply time dependent Lees-Edwards boundary conditions [158] in the z direction. In our simulations, we set $\gamma_0 = 0.2$ to stay in the liner rheology regime.

In the linear regime where the amplitude of strain oscillations is sufficiently small, the stress response takes the form $\tau_{xz}(t) = \tau_0(\sin \omega t + \delta)$ indicating that the stress oscillates with the same frequency as the strain, but leads the strain by a phase angle δ.

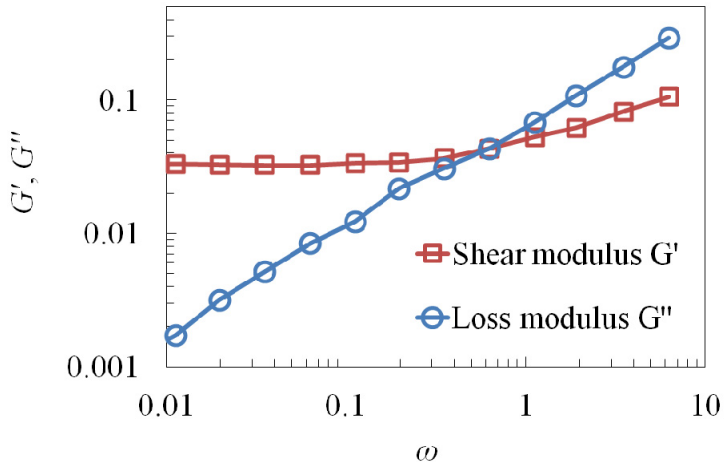

Figure 2.10 Storage and loss moduli versus oscillation frequency for a network with $N = 500$ and $C_{ave} = 8$.

In general, δ lies between 0 and $\pi/2$ and is a function of oscillation frequency. The limiting cases of $\delta = 0$ and $\delta = \pi/2$ correspond to a purely elastic material and a Newtonian liquid, respectively. At a given frequency, storage and loss moduli are given, respectively, by $G' = \tau_0/\gamma_0 \cos\delta$ and $G'' = \tau_0/\gamma_0 \sin\delta$.

Figure 2.10 shows the frequency dependence of dimensionless storage and loss moduli for a sample network with $N = 500$ and $C_{ave} = 8$. Here, the frequency ω is made dimensionless by the characteristic time scale of DPD $r_c\sqrt{m/k_BT}$. Our calculations indicate that G'' increases almost linearly with the oscillation frequency. This is very similar to the behavior of loss modulus in biopolymer networks [159-160] in which the main source of energy dissipation is the fluid viscosity. Our simulation further illustrate that when the frequency is small ($\omega < 0.1$), the storage modulus G' is nearly constant taking the value of shear modulus G. As the frequency increases above 0.1, the storage modulus starts increasing and scales with $\omega^{0.4}$. However, we expect that the scaling

breaks down at sufficiently high frequencies at which the network behaves as a glassy-like material. We will show in chapter 5 that for dry networks G' reaches a plateau in this situation. A similar trend has been observed for some biopolymer networks [160].

2.4.3 Swelling Properties

We access the swelling kinetics of our model network by calculating the evolution of solid and hollow spherical capsules with outer radius R during a swelling process. To model the change in the network swellability, we dynamically modify the length of network filaments by changing the effective equilibrium distance between DPD beads within each filament. This allows us to effectively simulate the internal stresses that cause the network to shrink or expand, and in this fashion, we can accurately capture the volume transition in polymer networks. In experiments, the appearance of internal network stresses driving gel swelling and deswelling volume transitions can result from changes in the environmental conditions such as pH, salt concentration, temperature, light intensity, etc. [4, 6-7, 9, 13-14, 161-165]. Specifically, to model network swelling we increase the equilibrium length of Frankel springs r_{eq} whereas we model deswelling by simultaneously reducing r_{eq} and decreasing the strength of DPD potentials between the filament beads.

To create hollow and complete spheres, we first generate a cubic network with a side greater/equal to the outer capsule diameter and then remove the beads that are outside the capsule shell. Specifically, a $30 \times 30 \times 30$ cubic network, with $N = 12000$, $C_{ave} = 8$, and porosity $\varepsilon \approx 0.85$ [136] is used to construct capsules of different radius and thickness.

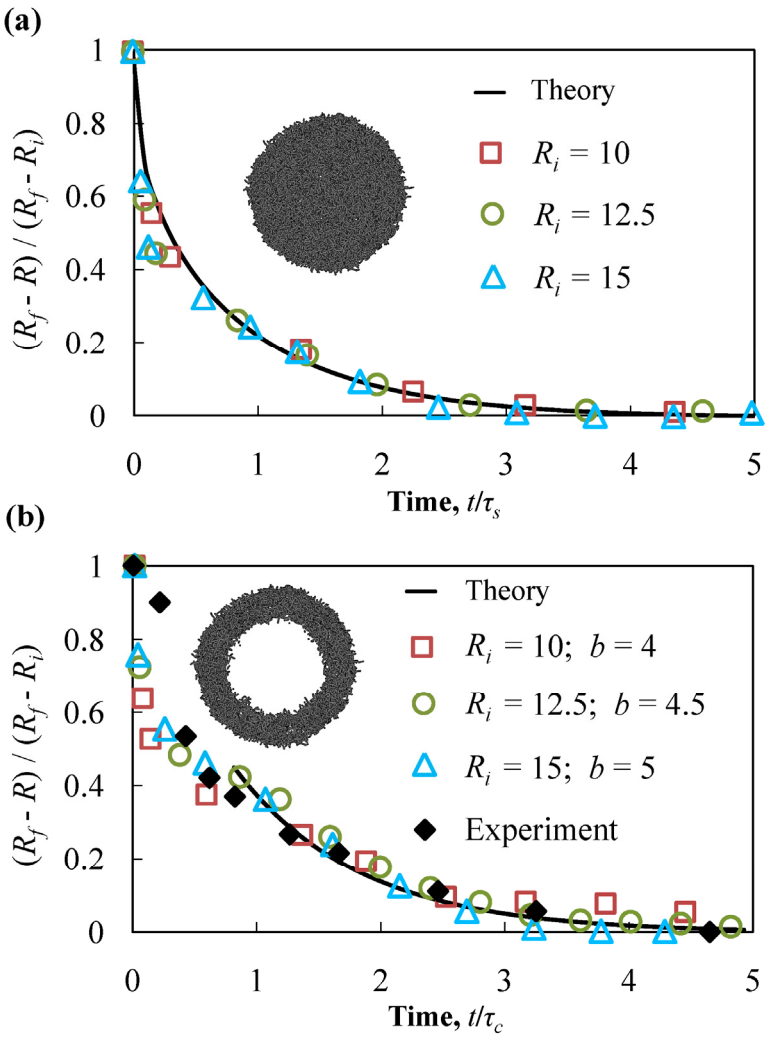

Figure 2.11 Outer radius of swelling (a) solid and (b) hollow microgel capsules versus time. The empty symbols represent the result of simulations with the initial shell porosity $\varepsilon = 0.85$. The filled symbols in panel (b) show the experimental results of Wahrmund *et al.* [82] for neutral microgel shells with $R_i = 30\mu\text{m}$, $R_f = 60\mu\text{m}$, and $D_c \approx 2\times10^{-7}\,\text{cm}^2/\text{s}$. The solid lines indicate the prediction of theory. For hollow capsules, only an asymptotic (long time) solution is shown.

We set the $\Delta t = 0.01$, $p = 1$, $m = 1$, $r_c = 1$, $\gamma^D = 4.5$, $a = 25$, $k_{\text{Frankel}} = 600$, $k_b = 7.5$, $r_{eq} = 0.4$, $k_BT = 1$, $\rho = 3$ and carry out the simulations in a $50\times50\times50$ periodic box. We change the equilibrium length of Frankel springs from $r_{eq} = 0.4$ to

$r_{eq} = 0.6$ at time $t = 0$ and measure the change in the outer capsule radius as a function of time (Figure 2.11). We normalize the radius by the total radius change $\Delta R = R_f - R_i$ and normalize the time by the characteristic volume transition times τ_s and τ_c equal to $\beta R_f^2 / D_c$, where β is a constant equal to $1/\pi^2$ and $1/9$ for, respectively, solid and hollow capsules [82], R_f is the radius at the fully swollen state, R_i is the radius at $t = 0$, and $D_c = (K + 4/3\,G)/f$ is the network collective diffusion coefficient [166]. Here, f is the friction coefficient representing a drag force on the network, and K and G are bulk and shear modules of the gel, respectively [82, 166].

Figure 2.11 shows that our model properly predicts the change in the outer radius of solid and hollow capsules during the network swelling. In Figure 2.11a, we compare our simulations with the Tanaka's model [166] for swelling kinetics of spherical gels and, in Figure 2.11b, with the theoretical and experimental study of Wahrmund *et al*. [82] for microgel shells. The theoretical models are based on the solution to the gel network equation of motion in the limit of low Reynolds number, which represents a force balance between the mechanical stresses within the gel network and the Stokes drag applied by the fluid subject to the stress-free boundary condition. The theory predicts that the characteristic time of swelling is proportional to R^2 / D_c.

Figure 2.11a shows that our results for swelling kinetics of solid capsules agree very well with the Tanaka's model [166]. Furthermore, Figure 2.11b shows that our simulations of swelling kinetic of hollow capsules agree with both the theoretical prediction and the experimental results for neutral microgel shells [82]. Hence, our model correctly captures the swelling dynamics of both solid and hollow capsules, which are

best fitted by the collective diffusion coefficients $D_c = 0.14$ and $D_c = 0.065$, respectively. Since both networks have identical porosity, we relate the difference in D_c for solid and hollow capsules to different effective elastic modules. When we create hollow capsules from cubic gels and remove the bead and connections that are inside and outside the shell, we effectively reduce the gel average connectivity at capsule surfaces, thereby reducing shell stiffness relative to the bulk material.

2.5 Summary and Future Directions

We used dissipative particle dynamics (DPD) to introduce a coarse-grained computational model for permanently cross-linked, semi-flexible polymer networks. We simulated networks as random lattice of interconnected filaments. We characterized the transport and mechanical properties of this mesoscale model. Our simulations indicated that the method we developed is able to capture key features of polymer networks micromechanics under both static and dynamic loadings. Moreover, the results of our characterization revealed that our model based on DPD can effectively simulate the permeation and diffusion in unstressed random networks. We also proposed an approach to model network swelling and demonstrated that it can properly capture the kinetics of network volume transition. Overall, our calculations indicated that our fully-coupled three-dimensional model can be effectively used to analyze transport properties of polymer networks under deformation, to examine release of encapsulated solutes from capsules during volume transition, and to explore complex tribological behavior of elastomers.

In future, our model can be extended by introducing electrostatic interactions. In this way, one would be able to simulate transport of ions and other charged entities which

might be of critical importance in specific problems. This will also allow one to study volume transitions due to a change in the salt concentration. Additionally, our model can be modified to simulate networks with active cross-links. Such model can be utilized to study unexplored properties of actively cross-linked polymer networks.

CHAPTER 3

TRANSPORT THROUGH MECHANICALLY DEFORMED POLYMER NETWORKS

3.1 Introduction

In practical applications, polymer networks are often under mechanical deformation, which gives rise to changes in the filament orientation and also may alter the volume occupied by network. The change in the orientation of filaments affects network transport properties [56, 93, 167]. It is, therefore, important to assess the effect of applied mechanical deformation on permeability and diffusivity of initially isotropic random polymer networks. Recently, the effects of axial compression on the permeability of articular cartilages [168], agarose gels [53] and deformable foams [54] were examined. It was found that, under confined compression/tension, permeability is a nonlinear function of applied strain and relatively insensitive to the changes in solvent volume fraction. There have been a number of studies on the effect of dynamic loading on the diffusion in gels with applications in articular cartilage biosynthesis, tissue engineering, and understanding the cell dynamics. Mauck *et al*. [169] examined the effect of dynamic loadings using a theoretical model, and investigated the circumstances under which convective transport induced by dynamic loading might supplement diffusive transport. They employed the theory of incompressible mixtures to model the tissue (gel) as a mixture of a gel solid matrix and two fluid phases. Their results revealed that the dynamic loading can be used to significantly enhance solute transport into the gel and even can affect certain physiological processes. Brangwynne *et al*. [170] also discussed the

importance of active processes used by living cells to boost and direct random, undirected thermal diffusion of small particles. Moreover, they discussed the recent progress in quantifying these transport mechanisms and identifying their origin and consequences. Finally, Li *et al*. [171-172] performed an experiment in which they measured diffusivity of a polymer electrolyte membrane (PEM) under uniaxial tension and showed that there is a linear coupling between the diffusivity and the alignment of membrane filaments. They found that the alignment of hydrophilic channels in the PEM increases markedly with the stretching. Furthermore, they observed substantial enhancement in water transport in the direction of stretching and suppression in the transverse directions. Their multi-axis NMR diffusometry also indicated that the total diffusion remains unchanged under axial deformation.

To facilitate the development of emerging applications of polymer networks, it is critically important to gain a fundamental understanding of the relation between the network structure and its transport properties, and establish how these properties change due to network mechanical deformation induced by external or internal forces. To date, however, our knowledge of the deformation dependent transport properties of cross-linked networks is still very limited. To bridge this gap, in this chapter, we examine convective and diffusive transport through mechanically deformed polymer networks.

3.2 Computational Setup

We carry out simulations in a $10\times10\times10$ periodic box that encompasses a viscous solvent and an elastic polymer network (Figure 2.3). We also set $\Delta t = 0.01$, $p = 1$, $m = 1$, $r_c = 1$, $\gamma^D = 4.5$, $a = 25$, $k_{\text{Frankel}} = 200$, $k_b = 2.5$, $k_{\text{FENE}} = 10$, $r_{eq} = 0.418$, $r_{\max} = 2$, $k_B T = 1$ and the solvent number density $\rho = 3$ yielding the solvent kinematic

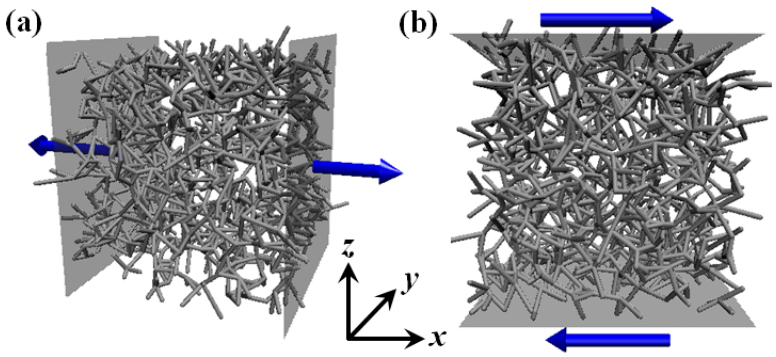

Figure 3.1 Networks under (a) normal and (b) shear deformations, respectively. The arrows indicate the directions of applied forces. Reproduced from Ref. 136.

viscosity η equal to 0.283. Unless specified otherwise, all dimensional values are given in DPD units.

We follow the same procedure described in the previous chapter to calculate the permeability in different directions. We evaluate diffusivities in the x, y and z directions by replacing the total displacement $|\mathbf{r}(t)-\mathbf{r}(0)|$ in the Einstein relation with the displacement in the corresponding coordinate directions. Unless specified otherwise, we use engineering strains to plot the results and we keep the network Poisson ratio 0.5, *i.e.* the porosity in deformed networks remains unchanged.

3.3 Results and Discussion

First, we present the results for networks under normal stress (Figure 3.1a) and then we probe the effect of shear on the network permeability and self-diffusivity (Figure 3.1b). We normalize the transport coefficients by their corresponding values for unstressed networks and average the relative quantities over 18 realizations. The results are plotted in Figures 3.2 and 3.4 with error bars representing the standard deviation from the mean value at each point.

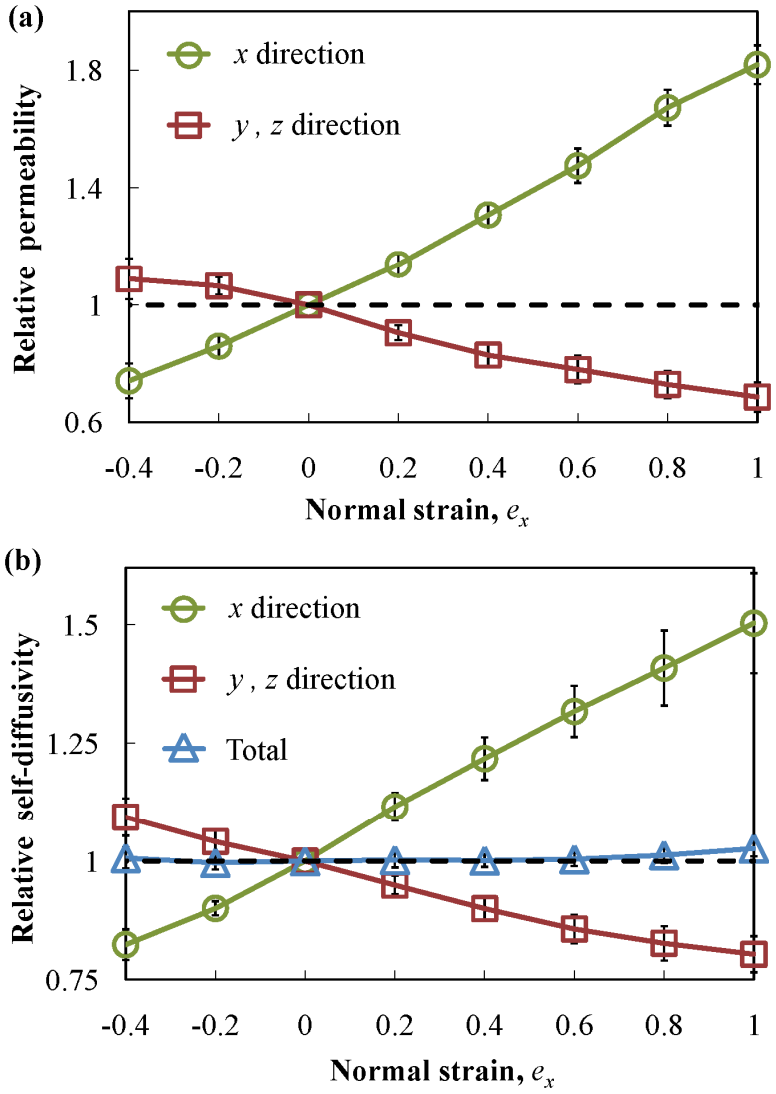

Figure 3.2 Relative (a) permeability and (b) self-diffusivity in the direction of coordinate axes xyz (see Figure 3.1) as a function of applied normal strain. The dashed horizontal lines indicate the unity values for unstressed networks. The error bars represent standard deviation from the average over 18 networks with $N = 250, 500, 1000$ and $C_{ave} = 4, 6, 8, 10, 12, 14$. Reproduced from Ref. 136.

Figures 3.2a and 3.2b show, respectively, the variation of permeability and self-diffusivity as a function of the normal strain e_x. The transport coefficients are calculated in the direction of applied stress and in the transverse directions (Figure 3.1). In all cases, stretching enhances transport in the elongated direction and hinders it in the transverse

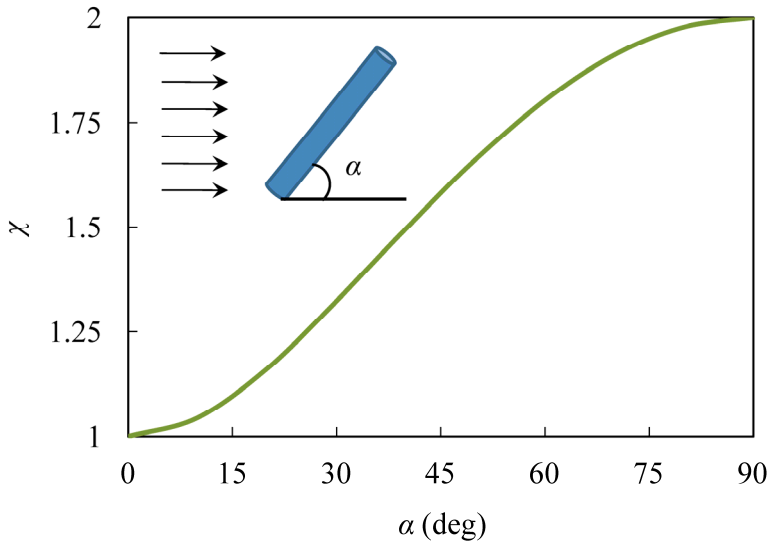

Figure 3.3 Stokes drag coefficient for a high aspect ratio filament as a function of its orientation relative to the flow direction.

direction in which the network is contracted. This phenomenon is a consequence of the change in average orientation of the filaments, which tend to become aligned in the direction of network tension [173]. The anisotropy in filament orientation results in an enhanced transport along aligned filaments. This transport enhancement takes place due to a lower drag experienced by filaments [56] and due to the fact that diffusive objects less likely collide with network filaments in their random walk in the direction of alignment [52]. We find that the total self-diffusivity remains constant indicating that the net diffusivity only depends on the network porosity which remains unchanged under load.

To further illustrate how filaments alignment influence transport through the network, in Figure 3.3 we plot the Stokes drag experienced by a high aspect ratio filament as a function of its relative orientation with respect to the flow direction [174]. We see that, indeed, the drag force on an inclined filament decreases as it becomes more

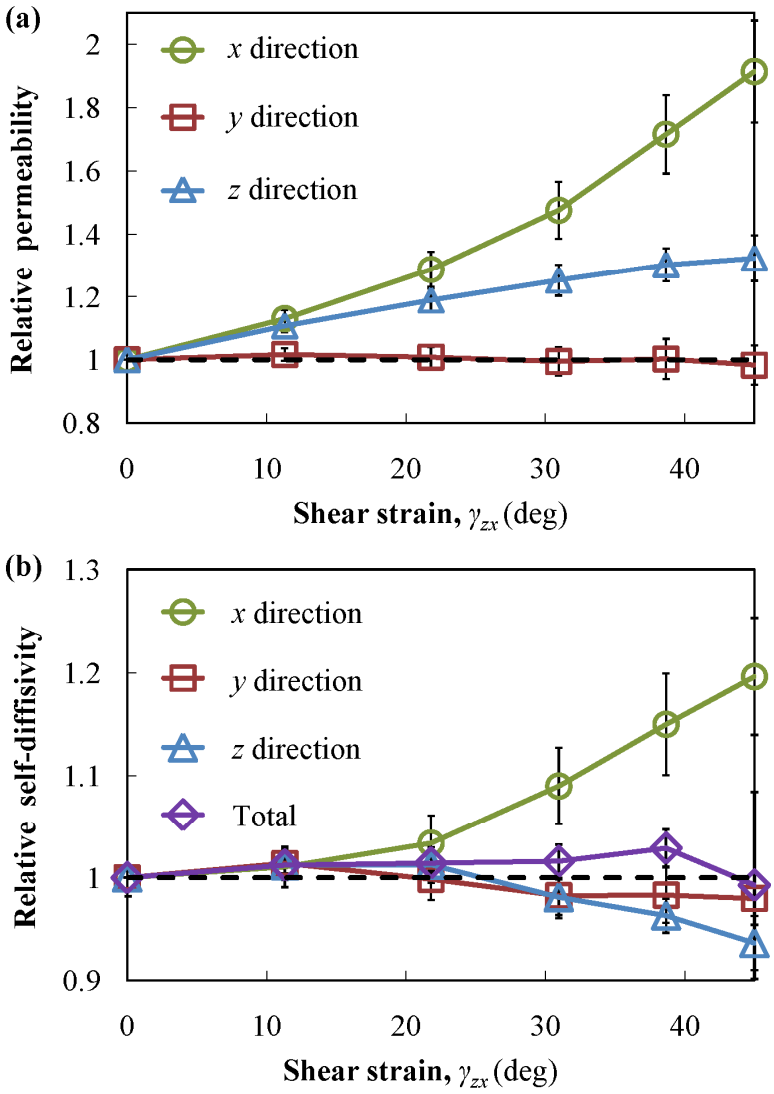

Figure 3.4 Relative (a) permeability and (b) self-diffusivity in the direction of coordinate axes *xyz* (see Figure 3.1) as a function of applied shear strain. The dashed horizontal lines indicate the unity values for unstressed networks. The error bars represent standard deviation from the average over 18 networks with $N = 250, 500, 1000$ and $C_{ave} = 4, 6, 8, 10, 12, 14$. Reproduced from Ref. 136.

aligned with the direction of the fluid flow. This is in very good agreement with the change in the relative permeability of axially deformed networks (Figure 3.2a). Furthermore, Figure 3.3 shows that the drag experienced by a filament parallel to the

direction of the flow is half of the one oriented perpendicular to the flow which agrees nicely with the results of Figure 3.2a.

Under shear, filament orientation changes primarily due to rotation of filaments without a significant change in their overall length. Figure 3.4 illustrates the changes in relative permeability and self-diffusivity caused by the applied shear strain γ_{zx}. While both permeability and self-diffusion increase in the x direction with increasing γ_{zx}, they are roughly constant in the y direction. Furthermore, unlike self-diffusion that slightly decreases in the z direction, permeability in this direction increases under shear. Also, similar to the axial deformation case, the total self-diffusion remains roughly constant. The application of shear strain only affects the orientation of filaments in the xz plane. Therefore, the permeability in the y direction does not change because the in-plane rotation of filaments does not affect the permeability in the direction normal to this plane [93].

To get a better insight into the deformation-dependent transport properties in random polymer networks, we quantify the mechanical deformation of networks. In our study, the network porosity is invariable under external loads; hence deformations imposed on the network can be translated to changes in the network alignment. To characterize the degree of network alignment, we employ a symmetric second-order orientation tensor [56, 173]

$$\mathbf{\Omega} = \frac{1}{l_{total}} \sum l_i \begin{bmatrix} \sin^2\varphi_i \cos^2\psi_i & \sin^2\varphi_i \sin\psi_i \cos\psi_i & \cos\varphi_i \sin\varphi_i \cos\psi_i \\ \sin^2\varphi_i \sin\psi_i \cos\psi_i & \sin^2\varphi_i \sin^2\psi_i & \cos\varphi_i \sin\varphi_i \sin\psi_i \\ \cos\varphi_i \sin\varphi_i \cos\psi_i & \cos\varphi_i \sin\varphi_i \sin\psi_i & \cos^2\varphi_i \end{bmatrix} \quad (3.1)$$

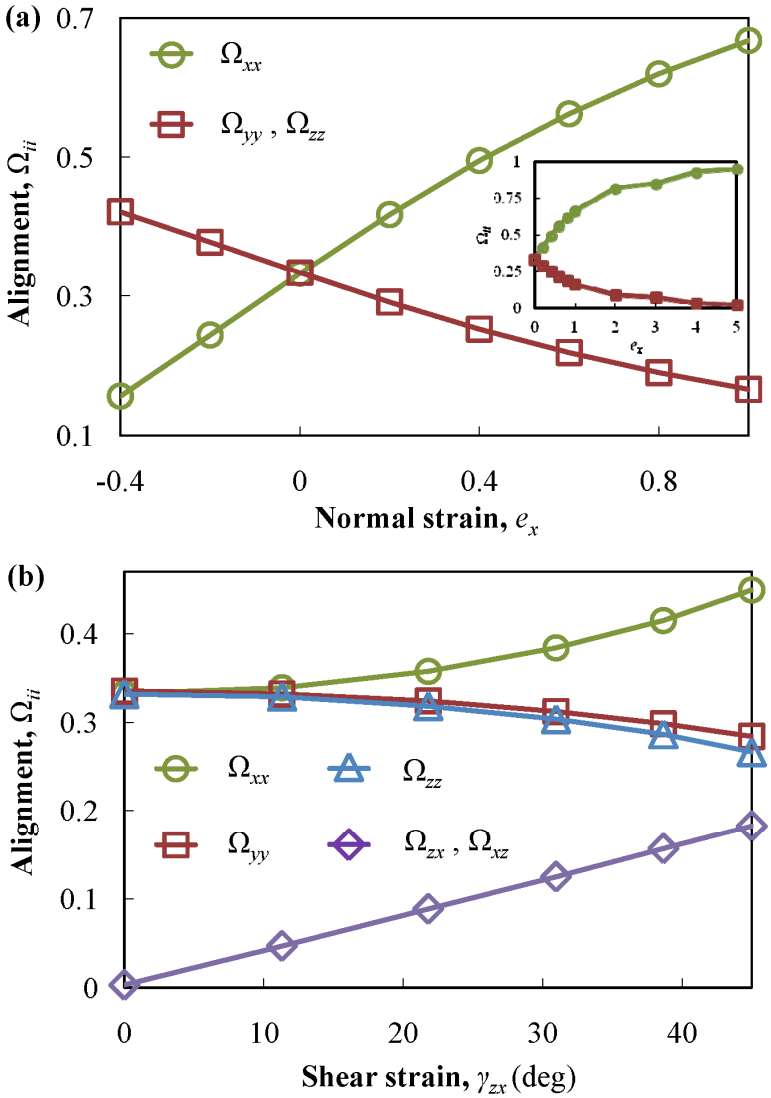

Figure 3.5 Components of the network orientation tensor versus applied (a) normal strain and (b) shear strain. Results are averaged over 18 networks with $N = 250,500,1000$ and $C_{ave} = 4,6,8,10,12,14$. The inset in part (a) shows the results for large normal strains $e_x > 1$. Reproduced from Ref. 136.

where l_i is the length of i th spring, l_{total} is the total spring length, and the sum runs over all springs constituting the filaments. Moreover, φ and ψ are angles between the vector representing the direction of a spring and the z and x axis, respectively. The trace of $\mathbf{\Omega}$ is equal to 1 and for isotropic networks $\Omega_{xx} = \Omega_{yy} = \Omega_{zz} = 1/3$ [56]. When off-diagonal

tensor elements are equal to zero, diagonal elements of the orientation tensor characterize the network alignment along the coordinate axes. On the other hand, non-zero off-diagonal components indicate that the network alignment does not coincide with the directions of the coordinate system.

Figure 3.5 shows how the magnitude of orientation tensor components changes when the network undergoes mechanical deformation. When a normal force is applied in the x direction, Ω_{xx} increases, and Ω_{yy} and Ω_{zz} decrease with increasing e_x (Figure 3.5a). This behavior continues until the network becomes fully aligned. For our networks, complete alignment happens at a strain of about 5 (see the inset in Figure 3.5a). In this situation, we can expect that the transport properties no longer change with an additional increase in the strain provided that the porosity remains unchanged. The results of Figure 3.5a also indicate that, under axial strain, the off-diagonal components remain zero, which means that the coordinate axes coincide with the principal directions of the deformed network. When the network deformation is due to a shearing force (Figure 3.5b), Ω_{xx} increases, while Ω_{yy} and Ω_{zz} slightly decrease with increasing γ_{zx}. More importantly, $\Omega_{zx} = \Omega_{xz}$ are not zero and increase with increasing γ_{zx}, indicating that the principal directions of this orientation tensor differ from the directions of the coordinate system xyz (Figure 3.1). By rotating the xyz system along the y-axis, the tensor can be readily expressed in terms of a new coordinate systems XYZ in which the axes coincide with the principal directions and all off-diagonal elements vanish.

To establish the dependence between the change in transport coefficients and the alignment of the network represented by $\mathbf{\Omega}$, we transform the xyz coordinate system to the XYZ system and plot the relative permeability along the new coordinate directions as

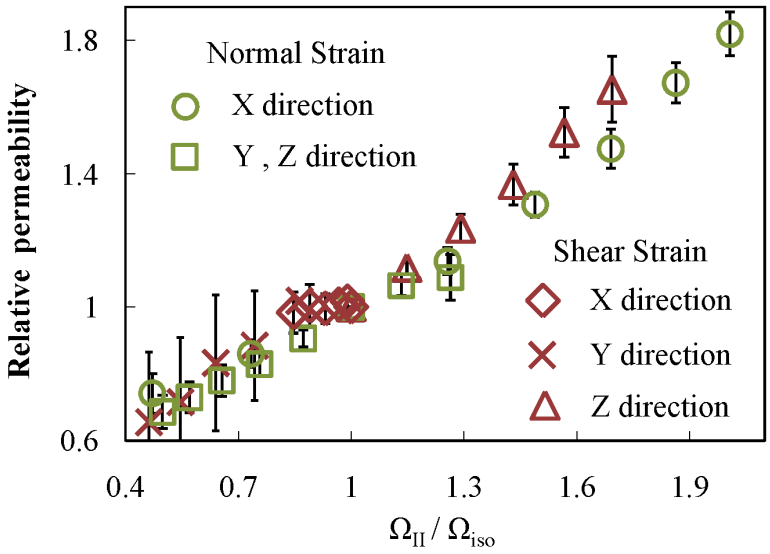

Figure 3.6 Relative permeability versus degree of orientation in principal directions for networks under normal and shear deformations. The error bars represent standard deviation from the average over 18 networks with $N = 250, 500, 1000$ and $C_{ave} = 4, 6, 8, 10, 12, 14$. Reproduced from Ref. 136.

a function of the corresponding diagonal components of the transformed orientation tensor (Figure 3.6). Here, we normalize tensor components by $\Omega_{iso} = 1/3$. We find that all data for permeability collapses into a single master curve, which exhibits nearly linear dependence on the magnitude of the orientation tensor eigenvalues (diagonal components in the XYZ). We note that the effect of porosity is factored out by averaging the results over 18 different realizations.

Thus, the alignment of network fibers due to an external mechanical load uniquely defines the change of permeability in a given direction relative to the un-deformed network. This information can be used to estimate the permeability of polymer networks based on the values of a deformation tensor that can be measured experimentally using 3D imaging techniques [140-141].

3.4 Summary and Future Directions

We employed a mesoscopic simulation technique to study the permeation and hindered diffusion through anisotropic (mechanically loaded) random polymer networks. We found that the network transport properties are defined by network porosity and filament alignment within the network. We characterized the network alignment due to mechanical stretching/compressing or shearing by a second order orientation tensor, and demonstrated that permeability along the principal directions of a deformed network is directly related to the magnitudes of the corresponding tensor components. We expect that our approach can be applied to also assess the diffusivity in polymer networks under mechanical load. Experimental study of Li *et al*. [171-172] explained earlier in this chapter corroborates with our expectation. Since the orientation tensor can be measured experimentally, our approach opens a way for estimating the permeability of deformable random networks under load.

To extend the current study, one could explore the effect of mechanical deformation on the transport properties of compressible networks including those with negative Poisson's ratios. When the Poisson's ratio is not 0.5, not only network orientation but also its porosity changes as a result of the applied strain. To evaluate the permeability and diffusivity in this situation, one needs to take both contributions into account. We anticipate, however, that these two effects are not tightly coupled. Therefore, one could deal with each factor separately and then superimpose in which case our universal permeability-orientation curve can be ready exploited after factoring out the effect of change in the porosity. Another direction to expand our work in this chapter is to examine the influence of gradient in the cross-linking density on the transport properties

of polymer networks. With the growing application of networks with non-uniform cross-linking density, there is a huge demand for characterizing their permeability and diffusivity.

CHAPTER 4

RELEASE OF NANOPARTICLES AND MACROMOLECULES FROM RESPONSIVE MICROGEL CAPSULES

4.1 Introduction

Functional materials have found an increasingly large number of applications in technologically advanced areas such as surface coatings, photonics, corrosion protection, biomedicine, and drug delivery. Among these materials, polymer gels of aqueous solutions (hydrogels) are of particular interest. These materials are typically responsive to external stimuli [4-8, 175], which makes them especially attractive for the use as drug delivery microcapsules. In this case, the delivery agent becomes an active participant, rather than a passive carrier, in the course of disease therapy [17]. A comprehensive review of various fabrication techniques used to prepare the capsules and different release mechanisms can be found elsewhere [17, 176-184].

Despite notable recent progress in synthesis and characterization of micro/nano gels, the development of functional delivery carriers remains to be a challenge. The release from microscopic gel carriers usually involves multiple time and length scales, geometrical complexities, and tight coupling between mechanical and fluid processes within gel polymer network [37, 185-186], which makes it difficult not only to rationally design experiments, but also to develop theoretical models able to predict the dynamic behavior of these multi-component, responsive systems.

To date, the majority of theoretical studies have been focused on simplified mathematical modeling of drug release [187-198] or volume transition during a delivery

process [82, 166, 186, 199-206]. These studies usually consider simple geometries and neglect the coupling among solute transport, volume changes, and possible fluid flows. Only a few recent works dealt with the challenging problem of the concurrent mass transfer and volume transition at the microscale, while even fewer works considered the release from responsive gels.

Experiments also have been focused mostly on the synthesis and fabrication of delivery agents and less attention has been paid to the fundamental understanding of the release [207-209]. This is in part due to the difficulty in tracking the motion of encapsulated solutes or visualizing the fluid flow and structure the polymer network at small scales. Below, we describe several investigations concerning the physics of the release. We begin with the theoretical analyses followed by the experimental studies.

Wang *et al*. [210] proposed a model based on diffusion and particle dissolution mass transport equations to probe the release of soluble drugs from an injectable hydrogel. Results of their simulations suggested that hydrogel matrices can act as polymeric excipients that accelerate the delivery of poorly soluble drugs and yield highly tunable release rates. Durbin and Buxton [211] employed a two-dimensional coarse-grained model based on Flory–Huggins and Cahn–Hilliard equations to simultaneously capture the swelling dynamics of polymer nanogels and the diffusion of encapsulated drugs. They modeled the entropic elasticity of the polymer chain through central force interactions between connected cross-link sites. The authors applied the model to investigate drug release from pH-responsive nanogels and found that the release increases with an increase in the shell hydrophobicity.

Soares and Zunino [212] introduced a model using mixture theory and Fick's law to capture the release due to hydrolytic gel degradation. Their modeling revealed that drug release from biodegradable matrices is an erosion-controlled process. Guo *et al*. [213] used dissipative particle dynamics to study the encapsulation of doxorubicin molecules in the core of micelles self-assembled from cholesterol conjugated His10Arg10, and found that DOX molecules can be efficiently encapsulated in the core of micelles. They demonstrated that the change in pH facilitates the release of DOX, which agrees with the experiments. Using a combination of semi-empirical and *ab initio* computations in vacuum stage, Srinophakun and Boonmee [214] analyzed the release mechanisms of the doxorubicin from a doxorubicin-conjugated glycol chitosan polymer. They found that the stability is increased when the length of the polyethylene glycol (PEG) chains in the glycol chitosan biopolymer is increased. Finally, Zarzycki *et al*. [215] developed a model for drug release from hydrogels by taking into account desorption processes on the solid phase surface and diffusion in pores. The authors verified the model by comparing their results with the experimental data concerning the release of bovine albumin from thermosensitive chitosan gels.

Bae *et al*. [216] experimentally investigated the release of indomethacin incorporated into temperature sensitive Poly-N-isopropylacrylamide (NIPAAm)/poly-tetramethylene ether glycol (PTMEG) interpenetrating polymer networks. They used temperature induced on-off mechanism to create pulsatile pattern in the network and showed that the release of indomethacin can be regulated by rapid deswelling of the surface of the network in response to temperature. Kono *et al*. [217] examined the release of NaCl from a pH-responsive polyamide capsule coated with a lipid membrane. The

authors demonstrated that encapsulated NaCl cab be released by changing the pH of the system. They further illustrated that diffusion driven release in this situation is linearly related to time.

Gutowska *et al*. [218] proposed a new drug release mechanism based on the mechanical squeezing of the host hydrogels. They performed experiments on several temperature and pH sensitive hydrogels and showed that the release profile is highly dependent on the degree and type of gel volume transitions which are controlled by the gel composition and the strength of the applied stimuli. Xing *et al*. [219] used sequential colloidal template polymerization to synthesize poly-acrylic acid (PAA) and poly-N-isopropylacrylamide (PNIPAM) nanogel capsules loaded with an antitubercular drug (INH). Their in *vitro* drug release study indicated that the release rate is prominently controlled by pH than temperature. More importantly, they demonstrated the possibility of drug release by deswelling the hollow capsules. Lastly, Pavlov *et al*. [220] introduced a novel approach based on low power ultrasound irradiation to release encapsulated proteins from polyelectrolyte multilayer microcapsules. Interestingly enough, the authors demonstrated that the release takes place not only as a result of complete ultrasonic disruption of the microcapsules but also as a consequence of increased permeability induced through small defects in the polyelectrolyte multilayers which can be self-healed when the irradiation is stopped.

Our literature review indicates that there is no previous theoretical or experimental study that fully describes the transport of solutes in dynamic polymer networks with complex geometries and associated fluid flows (Figure 4.1). However, the understanding of the coupling among these effects is vital for the development of novel

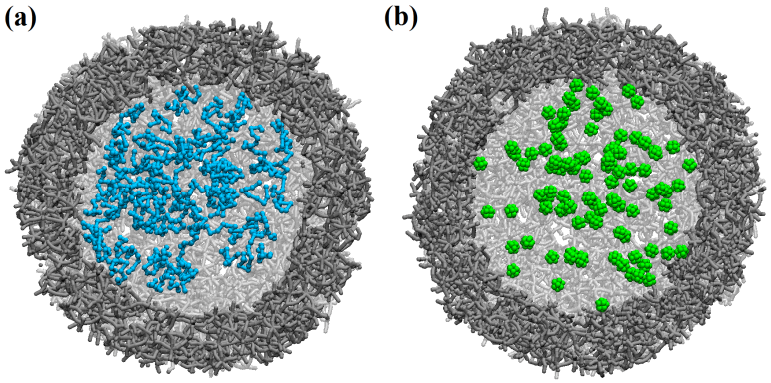

Figure 4.1 Cross-sectional views of initially equilibrated hollow spherical capsules loaded with (a) polymer chains (cyan) and (b) nanoparticles (green) inside the capsules cavity. The shell porosity is $\varepsilon = 0.85$ and the thickness is $b = R_i/3$, where R_i is the initial outer radius of the capsule. For clarity, solvent is not shown. Reproduced from Ref. 131.

mechanisms for controlled release of drugs and other solutes from responsive micro-carriers. In this chapter, we exploit our fully-coupled computational model to directly probe the release dynamics of nanoparticles and linear polymer chains from the interior of hollow gel microcapsules during swelling and deswelling volume transitions (Figure 4.1).

4.2 Computational Setup

We use a $30 \times 30 \times 30$ cubic network, with $N = 12000$, $C_{ave} = 8$, and porosity $\varepsilon \approx 0.85$ [136], to construct spherical capsules with an outer radius $R = 15$ and a membrane thickness $b = 5$. With this network arrangement, the average filament length is about unity, which we found to be small enough to provide microgel network integrity and capsule stability in the simulated conditions. In experimental settings, the capsule integrity can be further enhanced by choosing polymers with different molecular weights [177, 221]. To model network swelling, we increase r_{eq} by 50% that results in a 50%

increase in the capsule diameter (see Figures 4.2a and 4.2b). For modeling network deswelling, we simultaneously reduce the equilibrium length r_{eq} by 50% and the strength of DPD potentials between filament beads by 80%. This results in a 20% reduction in the outer diameter of the capsule (see Figures 4.2c and 4.2d).

To study the release of linear macromolecules, we load the microcapsule interior with 100 polymer chains (Figure 4.1a). Each chain is formed from 10 DPD beads connected sequentially by finitely extensible nonlinear elastic (FENE) springs with $k_{\text{FENE}} = 10$ and $r_{\max} = 1.5$. The gyration radius of these chains representing their hydrodynamic radius is $R_g \approx 1$ as calculated using equilibrium simulations in pure solvent. Unlike the polymer network, the encapsulated linear macromolecules are insensitive to external stimuli.

To examine and quantify the particle release, we introduce 100 nanoparticles that are initially randomly distributed inside the capsule cavity. The rigid nanoparticles are constructed from 13 DPD beads arranged in hexagonal close-packed spherical aggregates that obey the rigid body dynamics and interact with the solvent and network via the DPD potentials. The Stokes-Einstein radius corresponding to the effective hydrodynamic radius of these aggregates is $R_p \approx 0.7$ [152], which is slightly larger than the mean membrane pore size in the un-swollen initial capsule (Figure 4.1b).

We carry out the release simulations in a $50 \times 50 \times 50$ periodic box that contains a viscous DPD solvent, a polymeric microcapsule, and encapsulated nanoparticles/polymer chains (Figure 4.1). We also set $\Delta t = 0.01$, $p = 1$, $m = 1$, $r_c = 1$, $\gamma^D = 4.5$, $a = 25$, $k_{\text{Frankel}} = 600$, $k_b = 7.5$, $r_{eq} = 0.4$, $k_B T = 1$, and $\rho = 3$ yielding the solvent kinematic

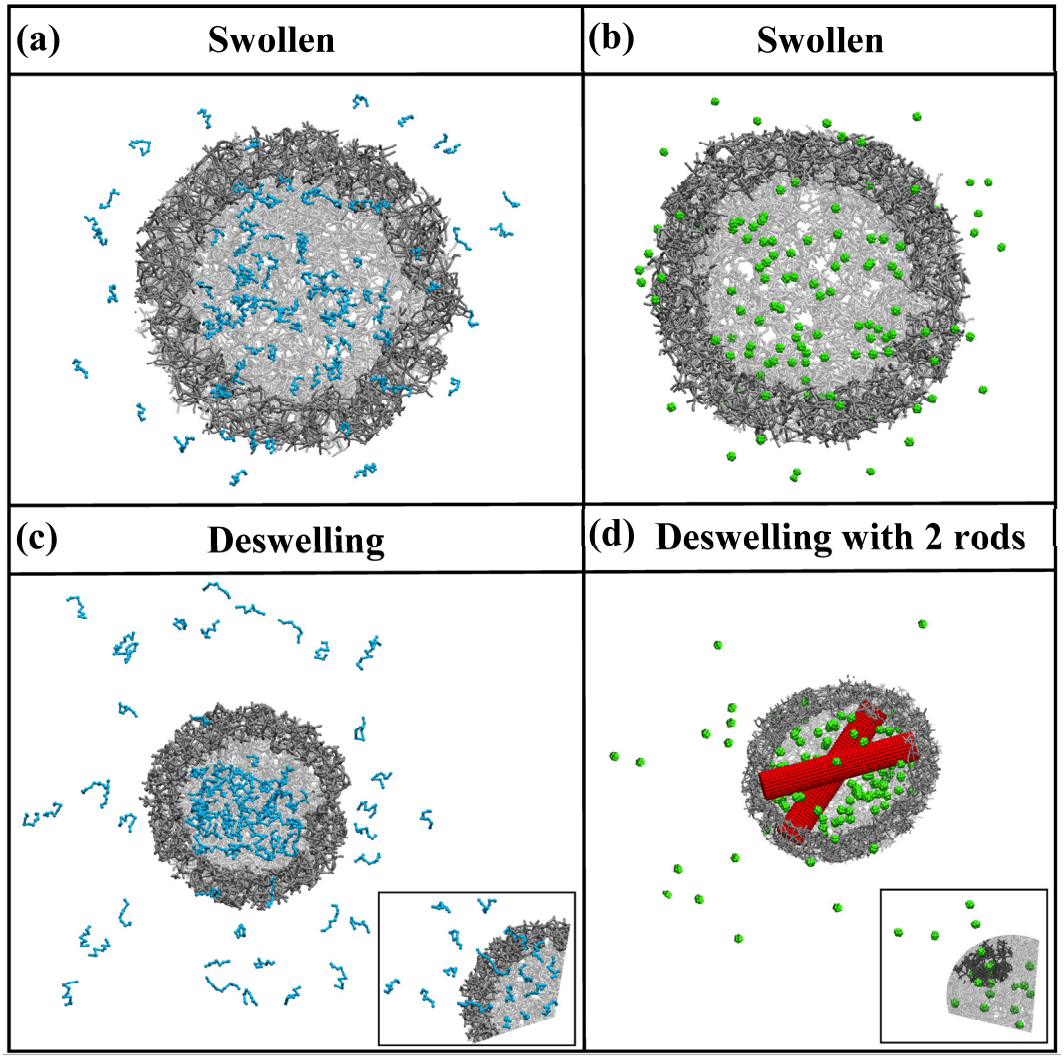

Figure 4.2 Panels (a) and (b) are snapshots from our simulations illustrating the release from swollen gel capsules of encapsulated polymer chains (cyan) and nanoparticles (green), respectively. The swollen capsules have an outer radius $1.5R_i$ and porosity $\varepsilon = 0.95$. Panels (c) and (d) are snapshots illustrating the release of, respectively, polymer chains and nanoparticles during capsule deswelling. The deswollen capsules have an outer radius $0.8R_i$ and porosity $\varepsilon = 0.75$. Panel (c) shows the release from a hollow capsule without rods, whereas panel (d) shows the release from a capsule with two enclosed microrods (red). The rods are not connected to each other and can move freely inside the cavity of an initially equilibrated capsule. For clarity, cross sections of the capsules are shown, whereas solvent is not shown. The inset in panel (c) shows polymer reptation across the deswelling capsule membrane. The inset in panel (d) shows a stream of nanoparticles discharging through a membrane pore during deswelling. Reproduced from Ref. 131.

viscosity η equal to 0.283. After an initial system equilibration, we change the filament

equilibrium length to mimic the gel swelling/deswelling and then continue the simulations for 3×10^5 time steps.

4.3 Results and Discussion

When the gel swells and its polymer network expands, the capsule increases in size and the external solvent penetrates into the growing capsule interior, whereas gel deswelling leads to capsule shrinking and, consequently, a part of the encapsulated solvent is expelled through the porous gel membrane. This cross-membrane flow defines the dynamics of the capsule volume change, which can be described in terms of a force balance between mechanical stresses in the elastic gel network that undergoes volume transition and viscous stresses due to the cross-membrane fluid flow [82, 166].

We first probe the release of nanoparticles and macromolecules from capsules in the initial equilibrium state which is characterized by membrane porosity $\varepsilon \approx 0.85$ (Figure 4.1). Figure 4.3 shows the cumulative fraction of released solutes as a function of release time. Here, time is normalized by the characteristic time of capsule volume transition $\tau_c = R_i^2/9D_c$, where R_i is the capsule outer radius in the initial state and D_c is the coefficient of collective diffusion of the gel [82]. For capsules considered in our study, $D_c \approx 0.065$ leading to $\tau_c \approx 400$ (see section 2.4.3). In Figure 4.3, each point represents an average over five independent realizations. We find that only a few particles and chains can diffuse out of the shell during the simulation time. This slow release is due to the small network mesh size in the initial capsule shell that practically prohibits diffusion of solutes.

In Figure 4.4, we show the cumulative size distributions of membrane pores of the capsule in its initial equilibrium and in the swollen and de-swollen states. Here, pore size

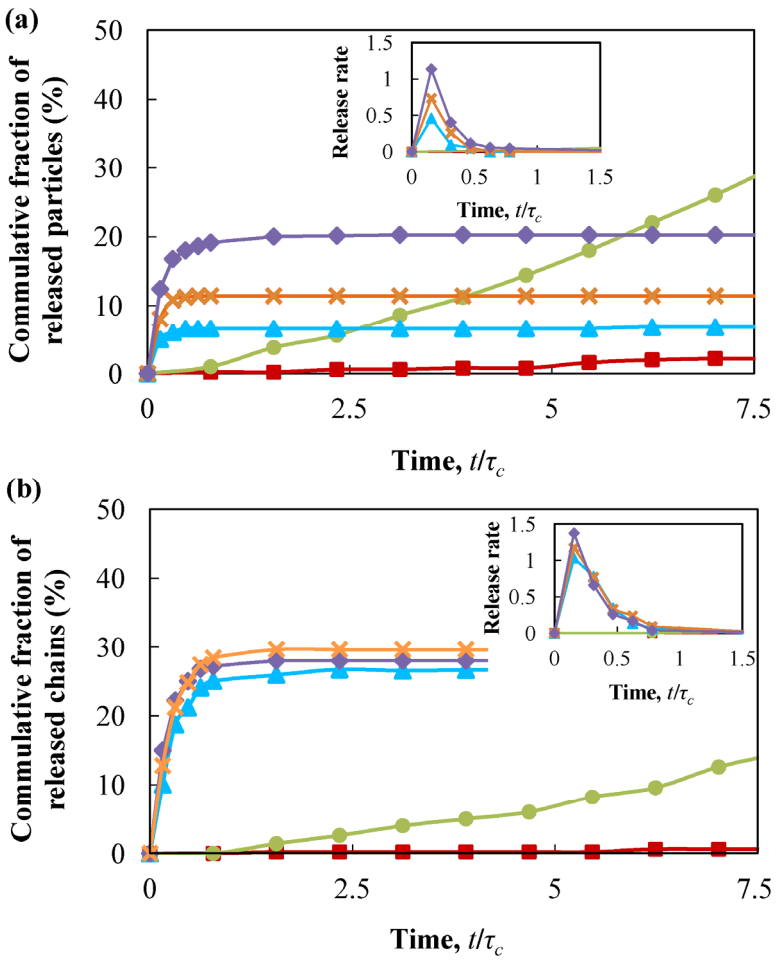

Figure 4.3 Cumulative fraction of (a) released nanoparticles and (b) released polymer chains versus time. The insets show the dimensionless release rate as a function of time. The squares, circles, triangles, crosses, and diamonds are for, respectively, initially equilibrated capsules, swelling capsules, deswelling capsules, and deswelling capsules with one rod and two rods. Each point is an average of five independent realizations. Reproduced from Ref. 131.

is estimated as the radius of the largest circle contained in a triangle formed by three adjacent network filaments and non-dimensionalized by the particle radius R_p. Indeed, we find that the average pore size in the initial equilibrium is smaller than the particle radius R_p and the chain radius of gyration $R_g \approx 1.4R_p$. In this conditions, the solute diffusion rate in the network is orders of magnitude slower than in the pure solvent [136].

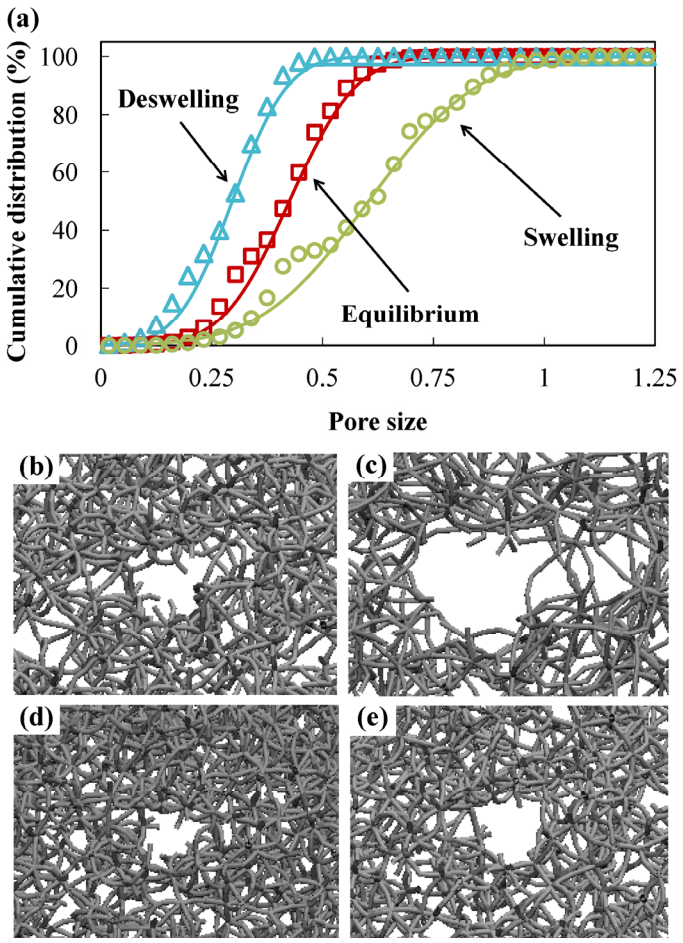

Figure 4.4 Panel (a) shows cumulative pore size distribution of the capsule shell formed from a random network of interconnected filaments. The pore size is non-dimensionalized by nanoparticles radius R_p. The symbols represent simulation data and the solid lines represent fits of normal distributions with the average and standard deviations identical to those of the simulation data. Panels (b), (c), (d), and (e) show representative changes in the pore size of the capsule membrane in the initial equilibrium, swollen, deswollen, and deswollen with two enclosed microrods states, respectively. Reproduced from Ref. 131.

We also find that the network pore distributions fo initial, swollen and de-swollen gels are close to the Gaussian distribution, which is in agreement with the experimental data of Mickel *et al*. [222].

When the gel swells, the network expands and both the capsule diameter and thickness increase by about 50% (Figure 4.2a and 4.2b) leading to porosity $\varepsilon \approx 0.95$ and

larger membrane pores (Figures 4.4a and 4.4c). While the porosity increases by only 10% from the initial capsule state, the solute diffusivity in the membrane, which is an exponential function of ε [49-50], increases by an order of magnitude [136]. This significant change of the shell diffusivity enables a steady release of encapsulated nanoparticles and macromolecules (Figure 4.3). We find an approximately tenfold increase in the release rate compared to the release from the initial capsule, indicating that the release is controlled by the membrane diffusivity.

The diffusion driven release for both nanoparticles and macromolecules proceeds with a nearly constant rate as indicated by a linear change in the cumulative number of released solutes in time (Figure 4.3). This constant release rate has been previously observed in experiments that probed the diffusion of solutes encapsulated in hollow microcapsules [217, 223-225]. The diffusive release has been also studied theoretically by considering particle diffusion through a porous capsule shell [187]. The long time solution predicts a release with a constant rate that is defined by the capsule geometry and the particle diffusion through the capsule shell. Thus, our simulation of release from swollen capsules agrees well with both experiment and theory.

Figure 4.3 also show that the rate of chain release is roughly twice slower than that of particles that have a smaller characteristic size and, therefore, can more easily percolate through an expanded gel network. The percolation through membranes can be characterized by an effective diffusion coefficient that is generally lower than the diffusion coefficient in unbounded networks due to an entropic barrier that prevents solute entrance into the network. This latter effect is more pronounced for flexible chains [226].

We note that during swelling, capsules temporarily lose their initially spherical shapes, which indicates a possible instability (buckling) caused by the rapid gel expansion. However, elastic forces in the membrane shell are sufficient to restore the nearly spherical shape after the equilibration of swollen capsules. The instability can be further mitigated by increasing the volume transition time.

When the capsule deswells, its diameter and membrane thickness decreases by 20% compared to the initial capsule size (Figure 4.2c and 4.2d) resulting in a smaller membrane pore size (Figures 4.4a and 4.4d). In this situation, one might expect that solute release will be further suppressed. Surprisingly, we found that it is not the case for hollow microgel capsules, where a rapid and massive release takes place during the capsule deswelling (Figure 4.3). This release is characterized by a rate which is much faster than that from swollen capsules with larger pores (see Figures 4.4c and 4.4d). Furthermore, we found that during deswelling polymer chains are released nearly twice faster than nanoparticles and the total amount of released chains is about four times greater (remember that the chains have a nearly 50% larger characteristic size than the nanoparticles and the release rate of chains from swollen capsules is about twice slower than that of nanoparticles). This fast solute release, however, only occurs for a short period during which the capsule undergoes the volume change.

Contrary to the swollen gel capsules where the release is controlled by diffusion, the release from deswelling capsules is facilitated by convective fluid flows induced by capsule shrinking. When capsule volume decreases, the encapsulated fluid is squeezed out from the capsule interior, carrying suspended solutes and enabling their rapid release. Since larger pores in the capsule shell have lower hydrodynamic resistance, the

encapsulated solvent flows through these larger pores, which allows the release even when the pore size decreases due to gel deswelling. The insets in Figure 4.2c and 4.2d illustrate the release of nanoparticles and polymer chains discharged through pores in a deswelling membrane.

We can estimate the efficacy of the hydrodynamic release by introducing a dimensionless Peclet number $\mathrm{Pe} = u\,b/D_n$ that compares the characteristic rate of solute discharge due to the fluid flow during capsule deswelling with the diffusion rate from an un-swollen capsule. Here, D_n is the effective diffusion coefficient of solutes in the capsule membrane network in the initial state, b is the membrane thickness, and $u = \Delta V/\left(4\pi\tau_c\left(R_i - b\right)^2\right)$ is the characteristic volume flow rate of encapsulated fluid per unit membrane area, where $\Delta V = \frac{4}{3}\pi\left(R_i - b\right)^3\left(1-\Theta^3\right)$ is the change in the capsule internal volume during deswelling and $\Theta = R_f/R_i$ is the deswelling ratio with R_f being the final outer radius.

Using the above expressions, we find that the Peclet number is $\mathrm{Pe} = \frac{\left(1-\Theta^3\right)}{3}\frac{D_c}{D_n}\frac{9b\left(R_i - b\right)}{R_i^2}$. Here, the first term indicates that convective transport is enhanced when the deswelling ratio decreases and more internal fluid is released. The second term represents the ratio between the capsule collective diffusion and the solute diffusion, and shows that the effect of hydrodynamic release can be enhanced by faster volume transition (larger D_c) and/or slower solute diffusion rate (smaller D_n). The last term represents the effect of capsule geometry and indicates that the hydrodynamic release is increased when the shell thickness is $b \sim 0.5R_i$.

For our simulation parameters, Pe is equal to about 120 and 450 for nanoparticles and polymer chains, respectively. Here, we estimate the effective diffusion coefficient D_n based on the release data shown in Figure 4.3. We find that our scaling model agrees well with the simulation results for polymer chains in which case $\mathrm{Pe} \approx 420$. However, when it comes to nanoparticles, our simulations yield $\mathrm{Pe} \approx 30$. Thus, the model predicts a number of hydrodynamically released particles about four times greater than what we obtain in the simulations.

This discrepancy between the scaling model and our simulations of nanoparticle release can be attributed to the rapid decrease of membrane pore size in shrinking capsules. When pores become too small for rigid particles to pass, the release terminates even when the encapsulated solvent is still leaking from inside the capsule. Indeed, we find that the nanoparticle release stops after $t/\tau_c \approx 0.5$, whereas the release of compliant polymer chains that can easily reptate through the porous membrane continues approximately twice longer driven by an outward fluid flow.

To prevent membrane sealing due to pore shrinking in deswelling capsules and enhance the release of nanoparticles, we introduce rigid microrods in the capsule interior (Figure 4.2d). The rods are comparable in length with the internal capsule diameter and can freely move inside an initially un-swollen capsule. However, when the capsule shrinks and decreases in size, the rods resist capsule shrinkage and stretch the membrane. The mechanical stretching induces stresses in the membrane that oppose the network contraction due to gel deswelling, thereby keeping the membrane pores open (Figure 4.4e). Specifically, we introduce rods with length $L = 10$ and radius $R_{rod} = 2$ that are

constructed by clustering DPD beads. The rods behave as rigid bodies and interact with the solvent network and nanoparticles via the DPD potentials.

The cumulative release and the release rates for deswelling microcapsules with one and two internal rods are shown in Figure 4.3. Indeed, we find that rigid rods enhance discharge rate of rigid nanoparticles compared to both the deswelling capsules without internal rods and the diffusion-controlled release from the swollen capsules (Figure 4.3a). Furthermore, we find that the net release of particles from a capsule with two separate rods is almost twice greater than from a capsule with one internal rod, and results in $\mathrm{Pe} \approx 90$, which is close to the theoretical limit. We relate this additional release enhancement to a stronger membrane stretching by two internal rods compared to one rod. Thus, by changing the number of encapsulated micro-rods one can engineer nanoparticle-loaded capsules that yield different release rates.

Whereas the release of nanoparticles is very sensitive to the presence of encapsulated micro-rods, the release of polymer chains from deswelling capsules remains practically unaffected after the inclusion of the rods (Figure 4.3b). The difference in the amount of released chains for simulations without rods and for simulations with one and two rods does not exceed 10%. This confirms that the release of linear macromolecules is not limited by the pore sealing in deswelling gel, but rather by the amount of released solvent during the capsule volume change.

Gels can typically swell and deswell reversibly [227-229] which makes responsive gels especially attractive for applications where periods of rapid discharge of encapsulated solutes should be followed by intervals of no release [230-231]. Such pulsatile drug delivery systems, for example, can be utilized in biomedical settings in

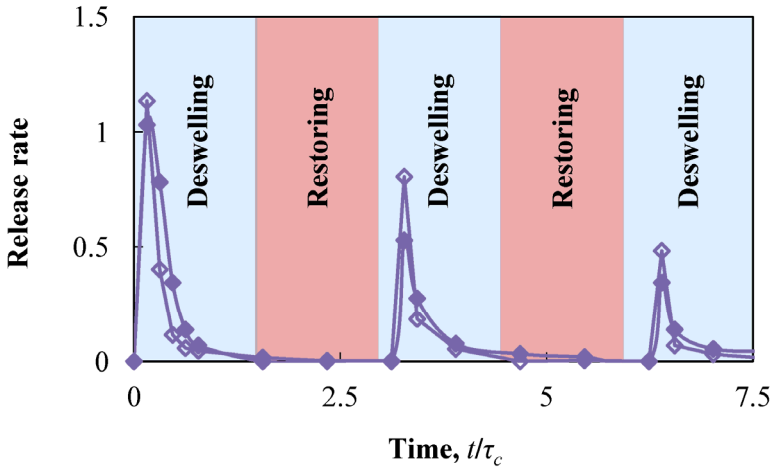

Figure 4.5 Pulsatile release from hollow responsive microcapsules that undergo reversible deswelling/restoring cycles. Filled symbols show dimensionless release rate of polymer chains from a capsule without rods (see Figure 4.2c). Empty symbols show dimensionless release rate of nanoparticles from a capsule with two encapsulated microrods (see Figure 4.2d). Each deswelling and restoring interval equals to $t/\tau_c = 1.6$. Reproduced from Ref. 131.

which a precise amount of the drug should be administrated with specific time intervals [232].

To probe the utility of responsive microcapsules in multi-pulse release applications, we carry out simulations of periodic release of macromolecules from capsules without rods and nanoparticles from capsules that enclose two independent rigid rods. In these simulations, capsules cyclically deswell (Figures 4.2c and 4.2d) and restore their initial state (Figures 4.1a and 4.1b) with constant time intervals equal to $1.6\tau_c$. Figure 4.5 shows the release profiles during three successive capsule deswelling/restoring cycles. The simulations reveal that immediately after the beginning of a deswelling interval, a significant amount of solutes is released. This burst release is then followed by a period of no release, which continues until the beginning of the next capsule deswelling cycle. Thus, the released amount is defined by the dynamics of capsule deswelling and is

insensitive to a particular extend of de-swollen and swollen periods, if they are greater than τ_c. The total amount of solutes that are released in consecutive cycles decreases due to their decreasing concentration within the periodically deswelling capsules.

4.4 Experimental Realization

The phenomena predicted in our simulations can be experimentally realized using microgel capsules with the outer radius of the order of $1\,\mu\text{m}$ and the collective diffusion coefficient $D_c \sim 10^{-7} - 10^{-8}\,\text{cm}^2/\text{s}$. Responsive capsules with such properties can be prepared using a verity of experimental techniques [17, 25, 27, 82, 181, 233-235]. For instance, Zha *et al*. [233] and Xing *et al*. [235] synthesized temperature responsive nanogel capsules by colloidal template polymerization followed by core removal. Zhang *et al*. [234] prepared responsive hollow nanogel shells by synthesizing core–shell nanogels. A hollow capsule was obtained after the degraded core was released through the shell. Wahrmund *et al*. [82] employed a capillary-based microfluidic device to form monodisperse poly-N-isopropylacrylamide (PNIPAM) hydrogel microcapsules. Another microfluidic approach was developed by Seiffert *et al*. [25] to synthesize multilayered microgel capsules. A variety of stimuli responsive micro and nano-capsules can also be formed using layer-by-layer (LbL) techniques [27, 177].

To induce a controlled release, these responsive capsules need to be loaded with nanoparticles and polymer chains with characteristic sizes comparable to the average pore size of the gel network which is typically in the range from tens to hundreds of nanometers. For example, Zahr *et al*. [236] used LbL assembly to encapsulate drug nanoparticles inside a macromolecular nanoshell. Wang *et al*. [237] introduced a facile approach for encapsulating water-insoluble compounds in polymer capsules using

mesoporous silica particle-mediated drug loading followed by the generation of a polymer multilayer shell using the LbL technique. Kozlovskaya *et al*. [238] fabricated hydrogel capsules by hydrogen-bonded self-assembly and then used them to encapsulate FITC-dextran by locking the capsule wall with electrostatically associating polycations at high pH.

Microencapsulation techniques are not limited to nanometer-sized solutes. Experiments have shown that micrometer-sized large structures can also be encapsulated inside the capsules. Kim *et al*. [239] and Shum *et al*. [240] demonstrated that microfluidics can be effectively employed to encapsulate objects comparable to the container in size. Dahne *et al*. [241] and Vriezema *et al*. [242] showed that large object can be self-assembled or polymerized inside microcapsules. Such approaches can be potentially employed to encapsulate microrods inside responsive gel capsules.

The amount of solute release from experimental microgel capsules can be adjusted by changing gel porosity and the degree of gel swelling/deswelling. Furthermore, the release time from deswelling capsules can be directly regulated by changing the capsule response time to volume transition τ_c. Since this timescale is proportional to R^2, the use of smaller capsules enables faster release. For example, for a capsule with typical network diffusivity $D_c \sim 10^{-7}\ \mathrm{cm}^2/\mathrm{s}$, the release time of the order of seconds can be obtained if the radius is about a few micrometers.

4.5 Summary and Future Directions

We employed a coarse-grained computational method to study the release of nanoparticles and macromolecules from responsive microgel capsules. Our simulations revealed that not only swelling, but also deswelling of hollow microcapsules can be

harnessed for controlled release. We showed that the release mechanisms for swollen and deswelling gel capsules are different. The release from swollen capsules is relatively slow, controlled by the solute diffusion through the capsule shell. The rate of this release depends on the degree of capsule swelling that sets the membrane porosity and, therefore, can be tuned in a wide range by modifying the gel chemistry. The release from deswelling capsules, on the other hand, is burst-like and is driven by the flow of the encapsulated solvent triggered by capsule shrinking. This rapid and massive hydrodynamic release occurs on the time scale of the deswelling volume transition. The amount of released solutes is controlled by the capsule volume decrease, whereas the release rate is defined by the deswelling kinetics. We found that deformable polymer chains that can easily penetrate through membrane pores are released in larger amounts from deswelling capsules, than nanoparticles that are filtered out by shrinking membrane pores. Our simulations further demonstrated that the inclusion of rigid microrods inside deswelling capsules mitigates the membrane pore closing, and in this fashion provides an effective method for regulating the rate of hydrodynamic release of nanoparticles. Finally, we showed that periodic deswelling of responsive capsules can be utilized in multi-pulse release applications. Thus, responsive microcapsules offer a uniquely adaptive and tunable delivery means that provides effective mechanisms for both basal and pulsatile release of encapsulated drugs and other solutes.

Our work in this chapter could be extended by considering release from cubic and tetrahedral capsules [243] and studying how capsule geometry affects the rate and duration of release. Furthermore, one could explore the possibility of using Janus capsules to facilitate the swelling-induced release. These capsules consist of two halves

with dissimilar swellablity, and, therefore, undergo anisotropic deformations in response to external stimuli that trigger the volume transition. These non-uniform deformations might give rise to a hydrodynamic flow from the capsule interior to the outside and, thereby, lead to release of encapsulated solutes.

CHAPTER 5

FRICTION OF POLYMER NETWORKS ON SMOOTH AND GROOVED SURFACES

5.1 Introduction

A large number of engineering and high tech applications involve sliding of a soft polymeric network over a solid wall and, often, the friction experienced during this sliding plays an important role in the overall performance of the system. Polymer networks have typically very low elastic moduli and high internal dissipation which makes their tribological properties quite different from that of conventional solids. For instance, elastomers are able to slide on a rough, rigid surface with and without a lubricant. Unlike solid friction in which the coefficient of friction is constant, friction coefficient of elastomers is not constant and changes with changing the normal force, temperature, and sliding velocity [28, 101-104, 110, 112, 124]. In addition, the tribological behavior of elastomeric materials in relative motion against a solid wall highly depends on the size, geometry, and distribution of surface asperities [32, 105-106, 110, 112-113]. Researchers have attempted to establish the dependence of elastomeric friction on these factors [28, 32, 100-113, 124]. Below, we describe several of the latest investigations.

Persson [106] used the theory of contact mechanics to investigate the adhesive and hysteric friction of elastomers sliding on solid rough substrates. He showed that the main part of the elastomeric friction comes from the energy dissipation in the bulk of the material which is caused by the oscillatory stresses acting on the polymer network from

the surface asperities. He further demonstrated that the adhesive interaction between the elastomer and substrate deforms the polymer network such that it follows the short-wavelength surface roughness profile of the surface. The results of Persson's calculations indicated that these viscoelastic deformations give rise to additional contribution to the sliding friction. Later, Persson [244] developed a more detailed theory for rubber contact mechanics and used it to probe how hysteretic rubber friction depends on the nature of the substrate surface roughness and the sliding velocity. This theory was further extended by Carbone *et al*. [113] for the case of surfaces with anisotropic roughness. The authors showed that the friction coefficient depends rather strongly on the sliding direction, whereas the area of contact is a weak function of the sliding direction. They also performed experiments on rubber blocks sliding on unidirectionally polished steel surfaces and found good qualitative agreement between the results of the experiment and the prediction of the theory.

In a separate study, Persson and Volokitin [245] developed a model for the sliding motion of viscoelastic solids on adhesive flat surfaces. Their model revealed that the thermal motion of molecules at the nanoscale could give rise to very strong fluctuating shear stresses comparable in magnitude with the depinning stresses at solid-elastomer interfaces. Their model also predicted a bell-shaped curve for the shear stress versus the sliding velocity. The authors found that the low-velocity side of the curve exhibits similar temperature dependence as the bulk viscoelastic modulus. Finally, they showed that the small-amplitude roughness has a negligible effect on the sliding friction of elastomers on adhesive flat surfaces.

Vorvolakos and Chaudhury [246] studied the kinetic friction of polydimethylsiloxane elastomers against a supported monolayer of hexadecylsiloxane and a thin film of polystyrene. They varied the molecular weight of the elastomer and measured the friction as a function of sliding velocity and temperature. The authors found that, on both surfaces, friction decreases with molecular weight. They also found that the friction initially increases with the velocity, reaches a maximum, and then decreases or approaches a plateau. In agreement with the previous theoretical studies, the authors observed that while the velocity of maximum friction is almost independent of the molecular weight of the polymer, it changes for different substrates.

Rand and Crosby [247] probed the tribological behavior of elastomeric wavy surfaces. To this end, the authors measured the sliding friction of a rigid spherical lens over a surface-wrinkled, elastomeric substrate. They carried out experiments both along and perpendicular to the surface wrinkles, and compared the sliding force to that required for sliding on non-wavy surfaces. They evaluated the effects of wrinkle dimensions and the applied normal force on the sliding resistance and showed that their result can be explained by a simple Bowden–Tabor friction model. Furthermore, they demonstrated that the wrinkle aspect ratio has a secondary effect on the sliding friction.

Recent advances in the microfabrication technology [34, 248] have enabled researchers to harness engineered roughness to regulate elastomeric friction [33, 35-36, 113, 249-250]. He *et al*. [250] employed a nanoindentation-scratching system to examine the effect of surface texture on the friction of micropatterned PDMS elastomers at the macro and micro scales. The authors found that while surface textures can significantly reduce the coefficient of friction at the macroscale, they play a less important role in

friction at the microscale. The lower coefficient of friction was believed to be the result of reduction in the real area of contact for patterned surfaces. Using a custom-made tribometer, Wu-Bavouzet *et al*. [33] investigated the friction of a flat PDMS lens on a pillared PDMS substrate for a range of normal loads, sliding velocities, and pillar sizes. The results of their experiments revealed that the frictional response of the system does not follow the classical Coulomb law and, instead, obeys an adhesive friction law of elastomers. Furthermore, the authors found that the contact on small pillars is intimate whereas the contact is laid on high pillars. Intimate and laid contacts, respectively, refer to situations where the rubbing surface touches the counter surface and where the rubbing surface is suspended above the counter surface asperities. Moreover, they demonstrated that, for some pillar heights, a transition from an intimate to a laid contact takes place as the sliding velocity increases.

Our review of relevant studies indicates that the tribological response of elastomers is very rich and complex and is still not completely understood [109, 251]. Moreover, to the best of our knowledge, the frictional behavior of elastomers sliding on ratchet surfaces (*i.e*. surfaces with ordered directional roughness) has not been considered and is yet to be explored. To get a better insight into the microtribology of polymer networks, there is an essential need for comprehensive computational models capable of simultaneously capturing the micromechanics of the polymer network, describing interfacial interactions, and resolving the thermal fluctuations. These models not only can improve our understanding of general tribological features of elastomers, but also can be used to predict the frictional behavior of future designs.

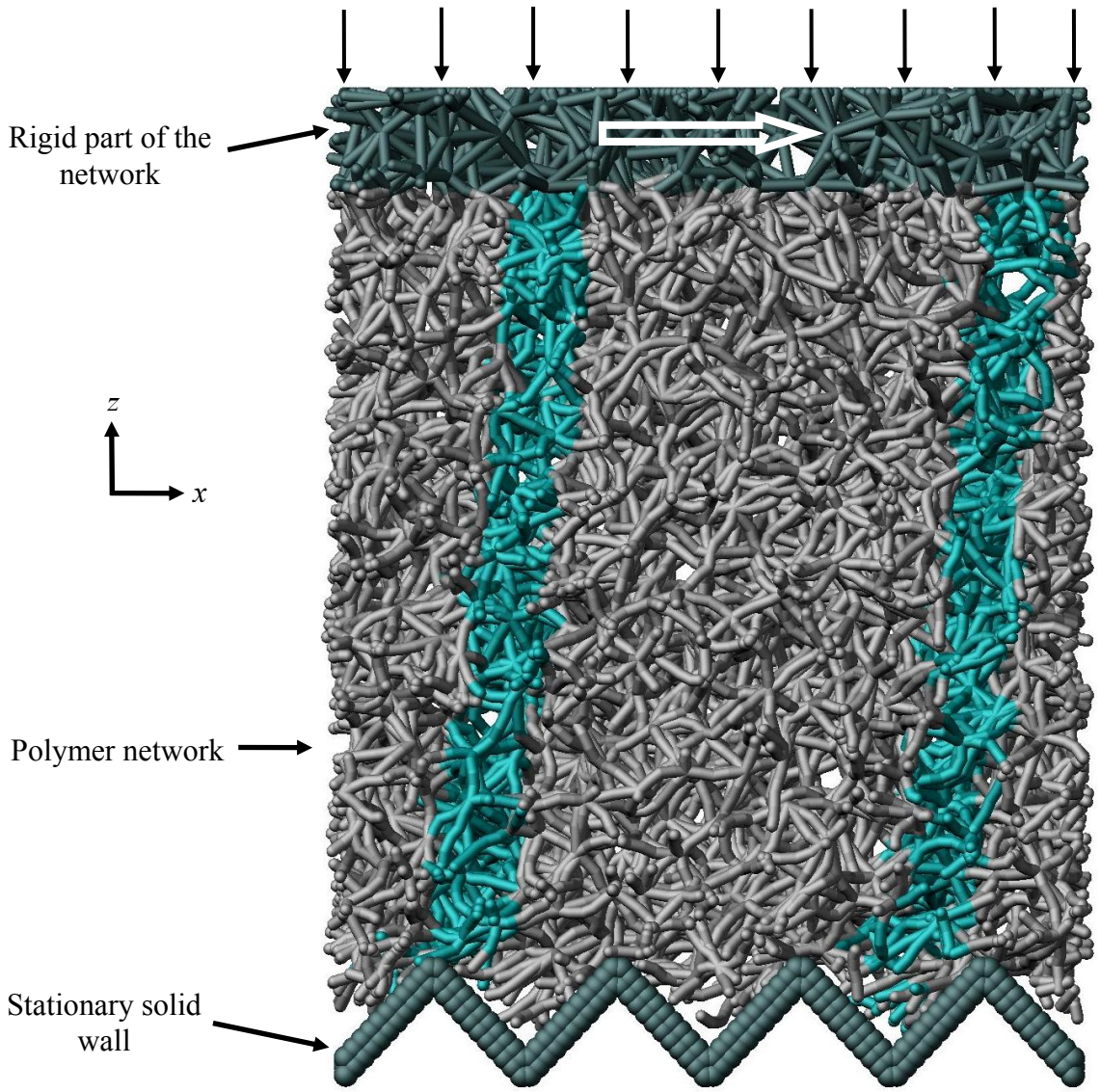

Figure 5.1 A snapshot illustrating a polymer network pressed against a fixed rigid wall while sliding at a constant velocity. The white arrow displays the direction of sliding whereas black arrows on top of the network display the direction of normal load. The cyan strips indicate parts of the network that are initially normal to the substrate and are deformed due to the shearing friction force exerted by the wall. Only two layers of wall beads are visible (see Figure 5.2).

In this chapter, we use our model for polymer networks to study the friction of elastomers in relative motion against flat and directionally grooved substrates. Our simulations shed light on the intricate relation between the coefficient of friction and

system parameters such as normal load, temperature, and sliding velocity. It also provides useful information for developing new methods of regulating friction and reducing wear using directional surfaces.

5.2 Computational Setup

Our model includes a semiflexible cross-linked network and a stationary solid wall (see Figure 5.1). The size of our computational domain is $15\times10\times25$ in the x, y, and z directions, respectively. The network has dimensions $15\times10\times17$ in the x, y, and z directions. It has $N=2550$ cross-linking nodes with the average connectivity of $C_{ave}=8$. Moreover, the top layer of the network with thickness $h=2$ is modeled as a rigid body (see Figure 5.1). This rigid part represents a solid plate attached to the top boundary of the network. Unlike the systems we considered in previous chapters, our system here does not include a solvent. Hence, our simulations represent the behavior of a dry elastomer. Unless specified otherwise, all dimensional values are given in DPD units.

In the simulations described in this chapter, we set the DPD parameters for our network to $\Delta t=0.01$, $p=0.25$, $m=1$, $\gamma^D=10$, $a=100$, $k_{\text{Frankel}}=600$, $k_b=7.5$, and $r_{eq}=0.27$. We assign the cutoff radius for repulsive and dissipative interactions to $r_c^{rep}=0.125$ and $r_c^{diss}=1$, respectively. Furthermore, we turn off DPD interactions among the beads that belong to the same filament. The use of two separate cutoff radii allows us to independently tune the range of repulsive and dissipative interactions between the filaments. In the absence of a solvent, repulsive interactions account for the excluded volume effect and prevent filament overlapping. Moreover, dissipative interactions

determine the strength of network internal friction. The combination of random and dissipative interactions also acts as a thermostat keeping the system temperature constant.

To evaluate the sliding friction of our network under a normal load, we apply a body force in the negative z direction to the rigid segment of the network and, at the same time, force the rigid part to move at a constant velocity in the positive x direction (see Figure 5.1). Then, we measure the opposing force exerted by the wall on the network in the direction of motion. The body force is distributed such that the total torque on the network's rigid part is zero. This is to ensure that the rigid segment remains parallel to the xy plane.

We examine the frictional behavior of our network on a smooth substrate and on surfaces with triangular, forward, and backward sawooth asperities (see Figure 5.2). We build the substrates from three layers of freezed beads arranged in a square lattice with the spacing $\Delta x = \Delta y = 0.25$. The layers are extended to the boundaries of the simulation box in the x and y directions. We fix the distance between the layers to $\Delta z = 0.234$ and shift the middle layer with respect to the top and bottom ones by a half of the lattice spacing. To model rough walls, we set the height and wavelength of asperities to $H = 2$ and $\lambda = 3.75$, respectively (see Figure 5.2). In all cases, we place the rigid walls just above the bottom of our simulation box.

We consider walls with both adhesive and non-adhesive surfaces. To model non-sticky surfaces, we let the beads in the top layer interact with the network beads via repulsive DPD interactions. In this case, we set the cutoff radius to $r_c^{rep} = 0.25$ and fix the strength of interactions to $a_{top} = 100$. We simulate adhesive walls by using a force

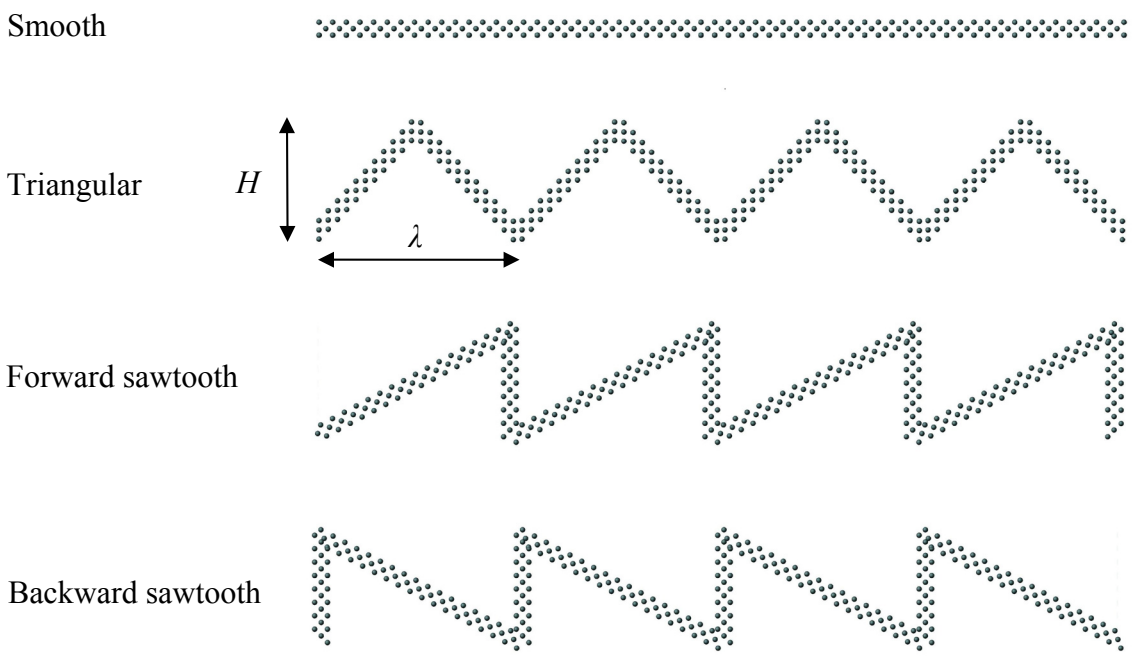

Figure 5.2 Smooth and grooved substrates modeled using three layers of freezed beads.

interaction in the form $F_{ij}^{A}=\begin{cases}-\Lambda_{ij}\left(r_{ij}/r_c^{adh}\right)\hat{\mathbf{r}}_{ij} & \text{for } r_{ij}<r_c^{adh}/2\\ -\Lambda_{ij}\left(1-r_{ij}/r_c^{adh}\right)\hat{\mathbf{r}}_{ij} & \text{for } r_{ij}\geq r_c^{adh}/2\end{cases}$ where Λ_{ij} is the attraction coefficient and $r_c^{adh}=0.25$ is the cutoff distance beyond which there are no interactions. To properly impose no penetration condition, we set the interactions between the network and beads in the middle and bottom layers to be the same as DPD repulsive interactions with $a_{mid}=200$, $a_{bott}=400$, and $r_c^{rep}=0.25$.

In our simulations, we use periodic boundary conditions in all directions. We note that, even without applying the boundary conditions, our choice of parameters and box size does not allow the polymer network to cross boundaries in the z direction. In our friction simulations, the run-time is always a few times larger than the initial transient period in which the friction increases rather linearly from zero and reaches a steady periodical state. We average the measured friction force over a time interval that is long

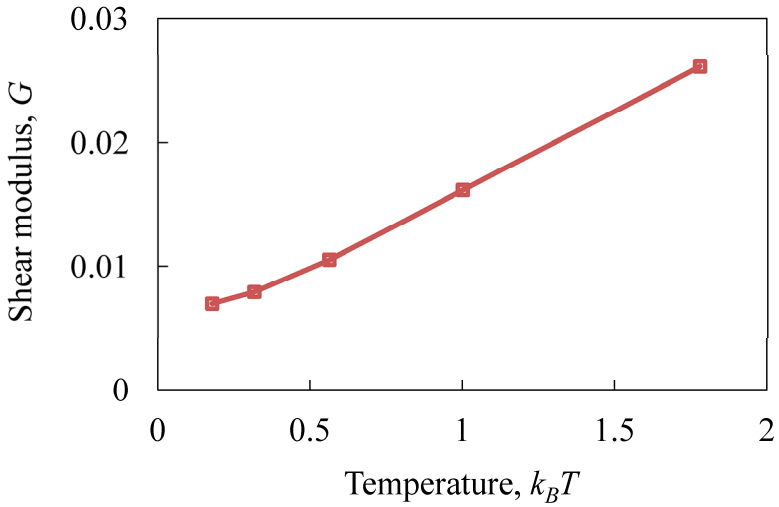

Figure 5.3 Network shear modulus as a function of temperature. The network parameters are $N = 2550$ and $C_{ave} = 8$.

enough to reduce noise in the data. As an example, for the sliding velocity of 0.01, we run the simulations for 4×10^5 time steps and average the results over the last 2×10^5 time steps. In the subsequent sections, we first evaluate the elastic and viscoelastic response of our network, and then present the result of our friction simulations.

5.3 Elastic and Viscoelastic Properties of Dry Network

We follow the procedures introduced in section 2.4.2 to characterize the mechanical properties. In particular, we set $\gamma = 0.2$ and $\gamma_0 = 0.1$, and measure the shear, loss, and storage moduli of our network. We perform the simulations using a $10\times10\times10$ cube created from the original $15\times10\times17$ network. Figure 5.3 shows the temperature dependence of the shear modulus G normalized by $k_{\text{Frankel}}/r_c^{diss}$. For the range of temperature considered, we see that G increases linearly with the temperature. This highlights the importance of entropic contribution in the elastic response of our network, which is also a characteristic of elastomers [252].

We plot the storage and loss moduli as a function of frequency for three different temperatures in Figure 5.4. The moduli and frequency are made dimensionless by $k_{\text{Frankel}}/r_c^{diss}$ and $r_c^{diss}\sqrt{m/k_BT}$, respectively. Our calculations show that the loss modulus G'' is nearly independent of the temperature and increases linearly with the oscillation frequency. This behavior is reminiscent of the response of Newtonian fluids with a viscosity equal to the slop of $G''-\omega$ curve. An analogous linear relation has been reported for the loss modulus of elastomers at intermediate frequencies [253]. We note that, without a host solvent, the main source of energy dissipation in the network is the internal friction between filaments. We also note that, in reality, the loss modulus of elastomers might be a stronger function of temperature.

When the period of strain oscillations is very larger, the network has enough time to respond to the applied deformations, and, therefore, the stress is in phase with the strain (see section 2.4.2). Hence, the viscoelastic network behaves like a purely elastic solid with a constant G' equal to G (see, for example, Figure 2.9). With an increase in the frequency, the period of oscillations becomes comparable with the network elastic response time causing the strain to lag behind the stress with a phase difference of δ. In this situation, the network does not have adequate time to react to the deformations, and, therefore, it appears to be stiffer. This behavior continues till the network reaches its glassy state where the stiffness is no longer a function of frequency. Indeed, the results of our simulations indicate that, for the three temperatures considered, the storage modulus G' initially increases with the frequency and then becomes nearly constant when the oscillation frequency is larger than 2. A similar trend has been observed for rubbers and elastomers [254]. Our calculations also demonstrate that the storage modulus has a

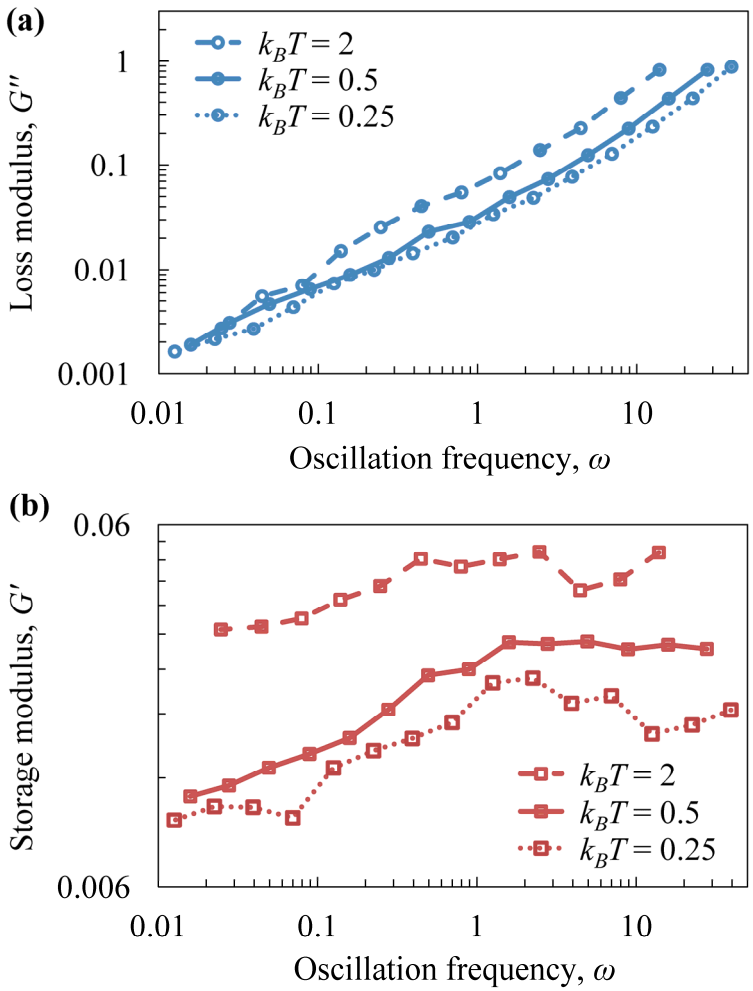

Figure 5.4 (a) Loss and (b) storage moduli versus oscillation frequency at different temperatures. The network parameters are $N = 2550$ and $C_{ave} = 8$.

stronger dependency on the temperature than the loss modulus and increases as the temperature rises. This is consistent with the variations of the shear modulus as a function of temperature (Figure 5.3). Overall, the results of mechanical characterization reveal that our dry network can reproduce typical elastic and viscoelastic response of elastomers.

5.4 Results and Discussion

The power required to rub an elastomer against a rigid wall at a constant speed is equal to the friction force experienced by the elastomer times the sliding velocity. This

power compensates for the rate of energy dissipation inside the elastomer. In the absence of adhesive surface interactions, the energy is dissipated due to cyclic deformations in the bulk of the elastomer network caused by oscillatory forces exerted by the periodic asperities of the counter surface. The frequency of these periodic deformations is proportional to the sliding velocity and is inversely proportional to the wavelength of asperities (see Figure 5.2). The resulting friction force in this situation is commonly referred to as the hysteretic friction and is directly related to the viscoelastic properties of the elastomer [104-105].

When there is an attractive interaction between an elastomer and a solid substrate, energy dissipation occurs not only in the bulk, but also at the network-wall interface. The resulting friction in this situation is commonly described as the adhesive friction [106]. However, there is no consensus among the researchers about the exact origin of dissipation at the interface [255]. For instance, Schallamach [103] and others [255] suggested that the energy dissipation occurs during a cyclic extension, detachment, and re-attachment of elastomer chains at the interface whereas Persson and Volikitin [245] attributed the energy dissipation to the stick-slip motion of segments of the elastomer close to the surface which they envisioned as stress patches. According to Schallamach's theory, the sliding friction does not necessarily correlate with the elastomer viscoelatic properties. On the contrary, Persson and Volikitin's theory predicts a close relationship between the friction and viscoelastic moduli of the elastomer. Here, we first present our results for the sliding on non-adhesive surfaces (hysteretic friction) and then discuss the sliding on adhesive substrates (adhesive friction).

To facilitate the comparison of our simulations with previous experimental and theoretical investigations, we use dimensionless parameters to present our results. We normalize the friction force by the normal load and present the results in terms of the friction coefficient μ. The sliding velocity V is normalized by the characteristic velocity of thermal fluctuations $\sqrt{k_B T/m}$. We make the normal load P dimensionless by the shear modulus multiplied by the apparent contact area. The shear stress σ_{xz} is made dimensionless by the shear modulus and, finally, the attraction coefficient Λ is normalized by $k_{\text{Frankel}} r_c^{adh}$. We note that the only parameter left dimensional is the temperature which is represented by $k_B T$.

5.4.1 Sliding on Non-adhesive Surfaces

We begin by examining the effect of sliding velocity on the hysteretic friction of our network. Figure 5.5 shows the variation of friction coefficient μ as a function of velocity V for sliding on smooth and grooved surfaces (see Figure 5.2). Here, the temperature and dimensionless normal load are kept constant. Consistent with the previous studies [104-105], we see that, regardless of the surface geometry μ initially increases logarithmically with the sliding velocity, reaches a maximum, and then decreases with further increase in the velocity.

At a fixed asperity wavelength, the frequency of oscillatory forces applied by the rough wall to the network increases with increasing the sliding velocity. We previously showed that the network loss modulus increases with the frequency. Therefore, an increase in the velocity results in a greater dissipation and subsequently higher friction. However, this trend changes as the period of imposed deformations approaches the

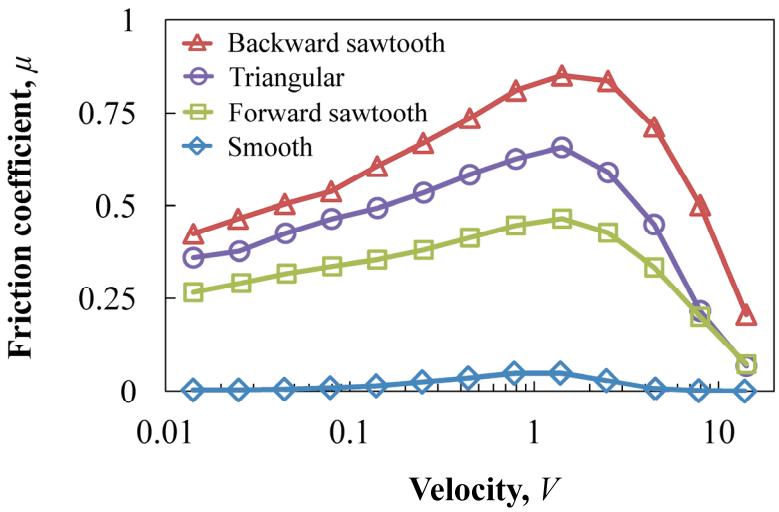

Figure 5.5 Friction coefficient as a function of velocity for the network sliding on non-adhesive smooth and grooved substrates (see Figure 5.2). The temperature and dimensionless normal load are $k_BT = 0.5$ and $P = 0.25$, respectively. The network parameters are $N = 2550$ and $C_{ave} = 8$.

minimum time required to fully dissipate the energy. At this point, the friction reaches its maximum value. When the sliding velocity further increases, the friction coefficient declines since the time available to dissipate the energy during one cycle of oscillations decreases. At very high velocities, the friction becomes practically nil as almost no energy is dissipated.

The minimum time for complete dissipation depends on how fast the disturbances can propagate and how far they need to travel to fully dissipate the energy. We estimate the former as the velocity of thermal fluctuations $\sqrt{k_BT/m}$ and the latter as the wavelength of asperities λ. To confirm that λ is a good approximation for how far the information travels, in Figure 5.6, we show the depth-averaged shear stress σ_{xz} distribution in the network for the sliding velocity corresponding to the maximum friction coefficient. Note that at this velocity, the network does not make a perfect contact with

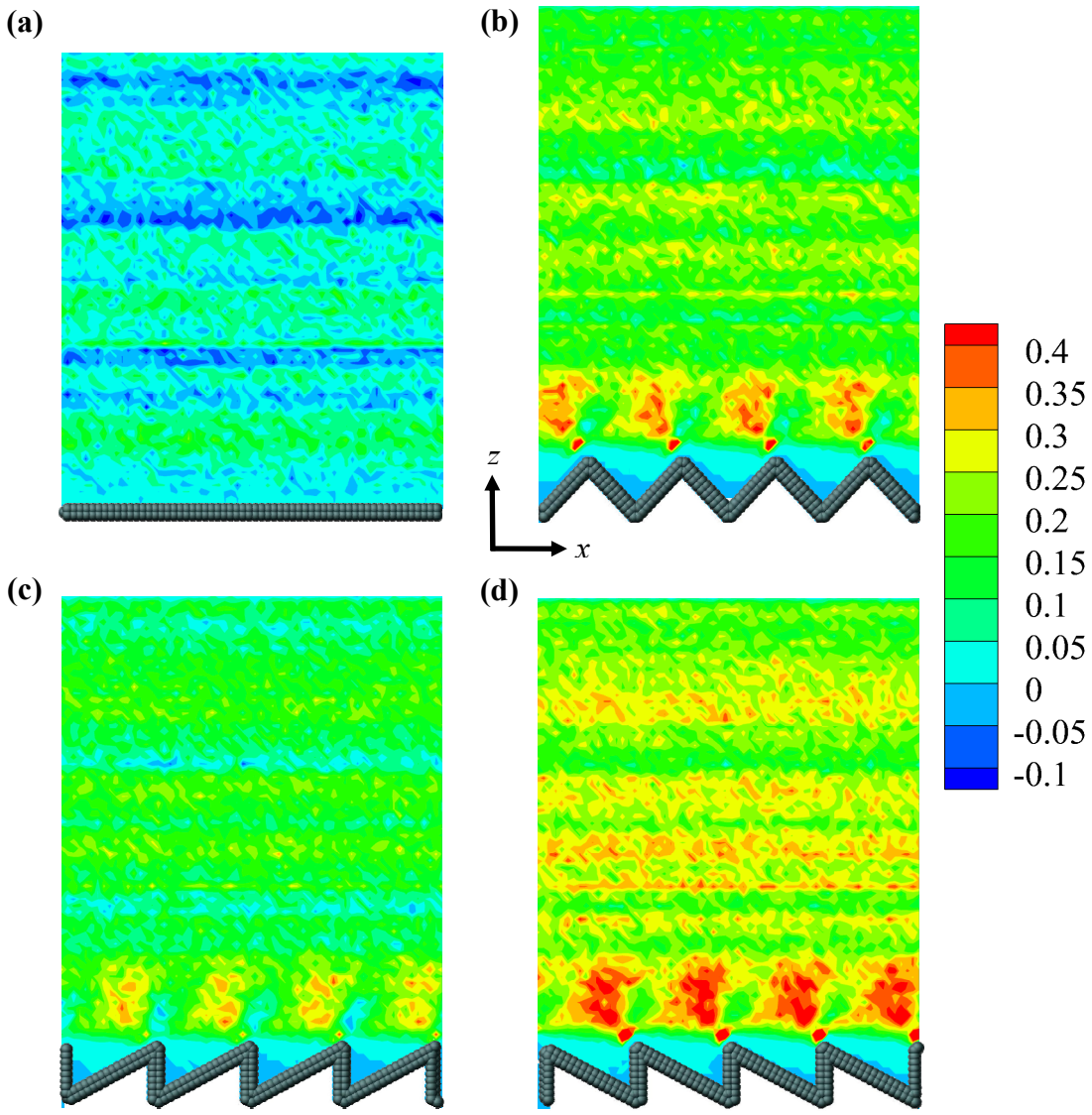

Figure 5.6 Shear stress σ_{xz} distribution in the network sliding on non-adhesive smooth and grooved surfaces. The stress is averaged over the depth of the network in the y direction and normalized by the shear modulus G. The temperature and dimensionless normal load are $k_BT = 0.5$ and $P = 0.25$, respectively. The sliding velocity in parts (a), (b), (c), and (d) is $V\sqrt{k_BT/m} = 1$. The network parameters are $N = 2550$ and $C_{ave} = 8$. Only two layers of wall beads are visible (see Figure 5.2).

the rough substrates. Figure 5.7 shows a series of simulation snapshots illustrating how the real area of contact changes as the network slides at different velocities on a rough rigid wall. The results of Figure 5.6 illustrate that in fact the area in which the majority of

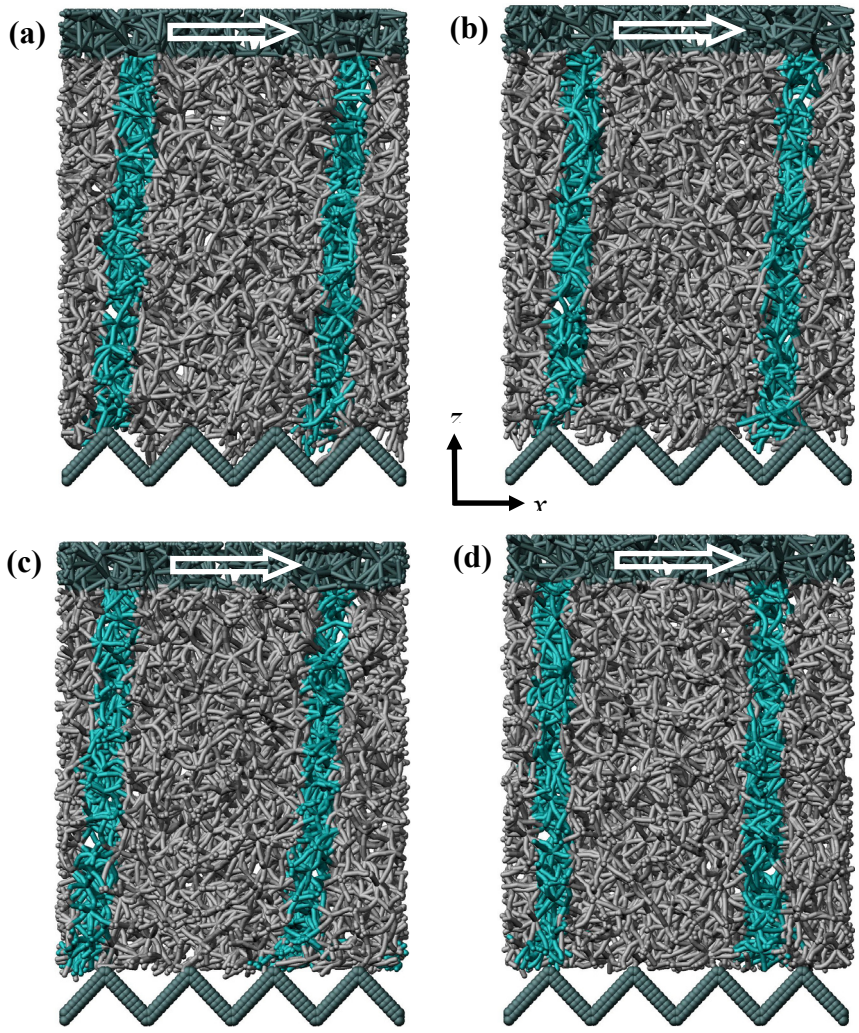

Figure 5.7 Snapshots illustrating the change in the real area of contact between the network and solid wall as the sliding velocity increases. The reduction in the real area of contact is a result of network stiffening due to the increased frequency of periodic deformations (see Figure 5.4b). The temperature and dimensionless normal load are $k_BT = 0.5$ and $P = 0.25$, respectively. The sliding velocity $V\sqrt{k_BT/m}$ in parts (a), (b), (c), and (d) equals to 0.01, 0.1, 1, and 10, respectively. White arrows display the direction of sliding. The cyan strips indicate the network deformation in response to the friction force exerted by the substrate. The network parameters are $N = 2550$ and $C_{ave} = 8$. Only two layers of wall beads are visible (see Figure 5.2).

energy dissipation takes place is of the order of λ^2 for both smooth and rough surfaces. We note that for the smooth surface $\lambda = \Delta x$. Therefore, μ should reach a maximum

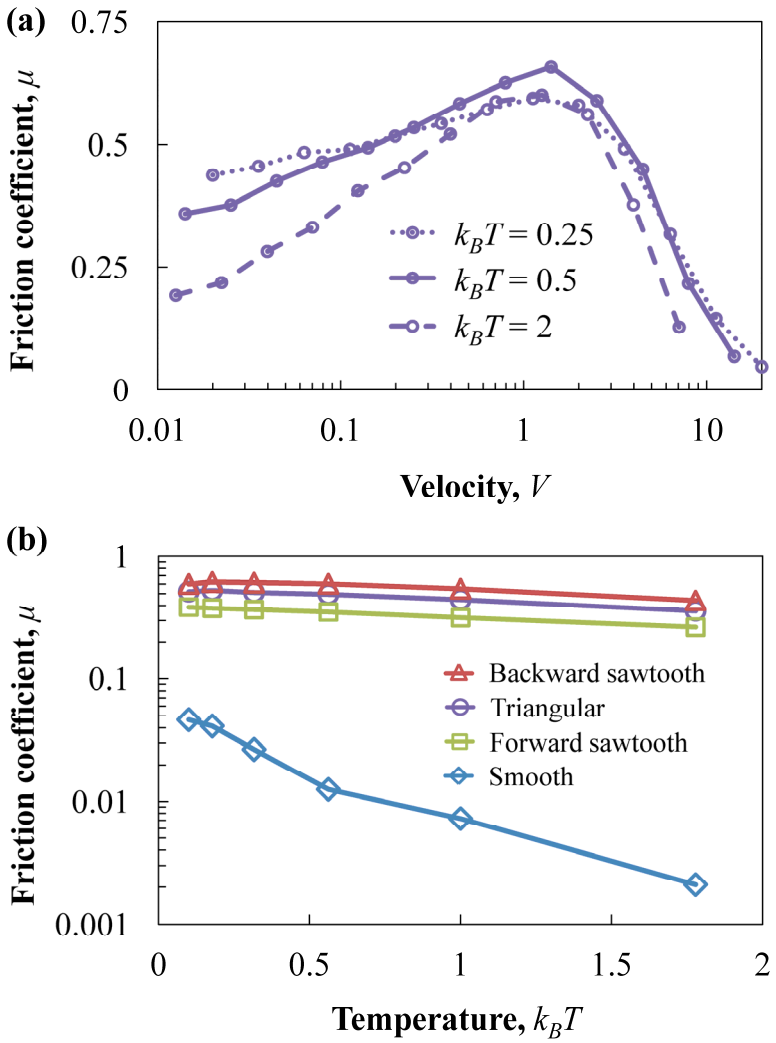

Figure 5.8 (a) Friction coefficient as a function of network velocity at different temperatures for sliding on the non-adhesive grooved surface with triangular asperities (see Figure 5.2). (b) Friction coefficient as a function of temperature for sliding on non-adhesive smooth and grooved substrates (see Figure 5.2). The sliding velocity is $V\sqrt{k_BT/m} = 0.1$. The dimensionless normal load is $P = 0.25$. The network parameters are $N = 2550$ and $C_{ave} = 8$.

when the period of oscillations becomes comparable with $\lambda/\sqrt{k_BT/m}$ or, in other words, when $V \sim 1$. Indeed, Figure 5.5 shows that the velocity corresponding to the maximum friction is $V_{\max} \sim 1.4$ for flat and ratcheted substrates.

Furthermore, our simulations reveal that, at a given asperity height and wavelength, the friction coefficient is the lowest for a surface with forward sawtooth grooves, while the surface with backward grooves leads to the highest friction. This behavior agrees very well with the observations of Carbone *et al*. [113] and further proves that the hysteretic friction strongly depends on the direction of sliding for surfaces with anisotropic roughness. Figure 5.6 also demonstrates that the stress concentration at the tip of asperities is significantly reduced for surfaces grooved in the direction of sliding. The lower stress concentration might be important for reducing wear. Therefore, our findings could potentially lead to new way to reduce friction and control wear by engineering surface roughness.

To get a better insight about the hysteretic friction of our network, we examine the effects of temperature and normal load on the coefficient of friction. Figures 5.8a shows $\mu - V$ curves of the symmetrically grooved substrate for three different temperatures. Our calculations demonstrate that irrespective of the temperature the maximum friction happens at the same dimensionless velocity, which again supports our argument about the velocity of maximum friction. In Figure 5.8b, we present the variation of μ as a function of temperature at a fixed sliding velocity below $V_{\max}$. We see that for smooth and grooved surfaces, the friction exponentially decreases with the temperature $\ln \mu \propto -k_B T$. Qualitatively similar behavior has been observed experimentally [256-257].

Figure 5.9 shows the normal load dependence of the friction coefficient. From Figure 5.9a, we see that $V_{\max}$ is independent of the normal load. The results of Figure 5.9b also indicate that when the normal load is small, μ increases with P. However, in

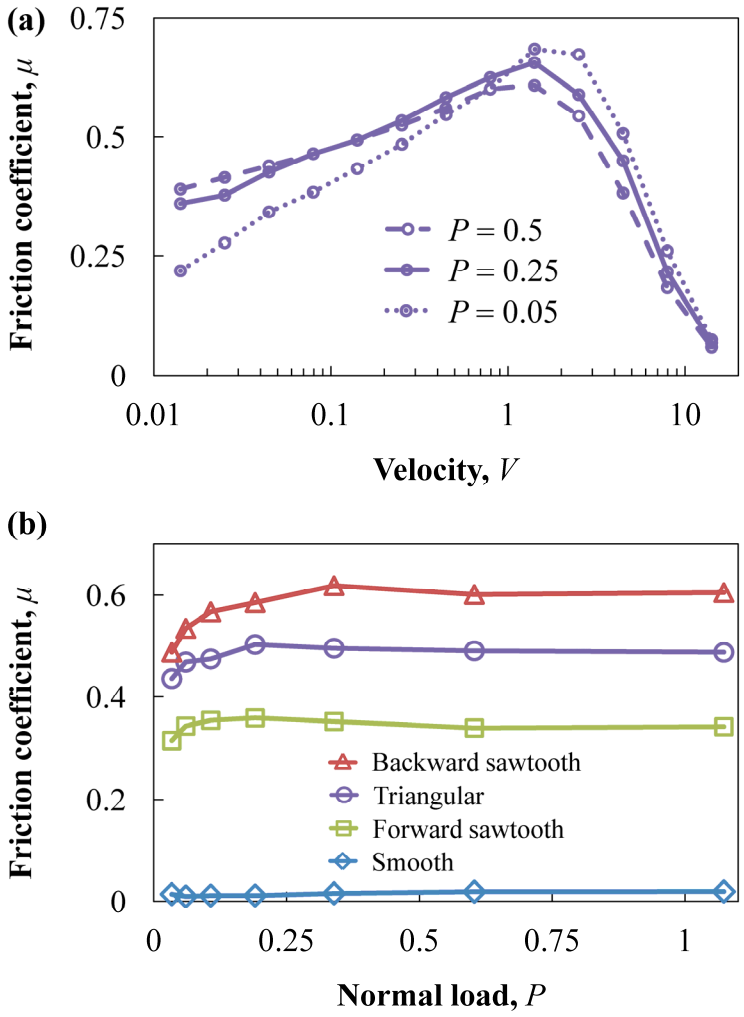

Figure 5.9 (a) Friction coefficient as a function of network velocity at different normal loads for sliding on the non-adhesive grooved surface with triangular asperities (see Figure 5.2). (b) Friction coefficient as a function of normal load for sliding on non-adhesive smooth and grooved substrates (see Figure 5.2). The sliding velocity is $V\sqrt{k_BT/m} = 0.1$. The temperature is $k_BT = 0.5$. The network parameters are $N = 2550$ and $C_{ave} = 8$.

accordance with the experimental measurements [113, 258], the hysteretic friction coefficient becomes independent of the normal load at intermediate values of P. In this situation, the normal load is proportional to the real area of contact, which itself is proportional to the friction force [105, 244]. Hence, the coefficient of friction, defined as the friction force divided by the normal load, remains unchanged.

5.4.2 Sliding on Adhesive Surfaces

Similar to the previous section, we first study the velocity dependence of the friction coefficient. The results of our simulations are presented in Figure 5.9 for smooth and corrugated surfaces (see Figure 5.2) with the attraction coefficient $\Lambda = 1/12$. For all substrates, our simulations reproduce the bell-shaped curve for the dependence of friction coefficient on the sliding velocity as reported in the earlier theoretical and experimental studies [103, 245, 255]. Comparing Figures 5.5 and 5.10, we see that the friction increases when there is an attraction interaction between the network and counter surface. As mentioned earlier, the energy dissipation happens both in the bulk and at the adhesive interface. For the non-adhesive smooth surface, the dissipation in the bulk is almost negligible (see Figure 5.5). Thus, the friction on the smooth adhesive surface can be seen as a measure of how much energy is dissipated at the interface. We already calculated how much energy is dissipated in the bulk for non-adhesive rough surfaces (Figure 5.5). Therefore, we should be able to estimate the friction on adhesive rough surfaces by adding the friction on non-adhesive rough surfaces to the friction on the adhesive smooth surface. In fact, Figure 5.10 shows that the adhesive friction of ratcheted surfaces is approximately equal to the summation of the two contributions.

Figure 5.10 shows that $V_{\max}$ depends on the size and shape of surface roughness. The velocity of maximum friction is about $V_{\max} \sim 0.5$ for the flat wall and for the wall with forward sawtooth asperities. Previous studies [255] have shown that when friction is dominated by the energy dissipation at the interface, the friction coefficient starts decreasing before the period of oscillations reaches the minimum time required to fully dissipate the energy. The velocity corresponding to the maximum friction in this case is

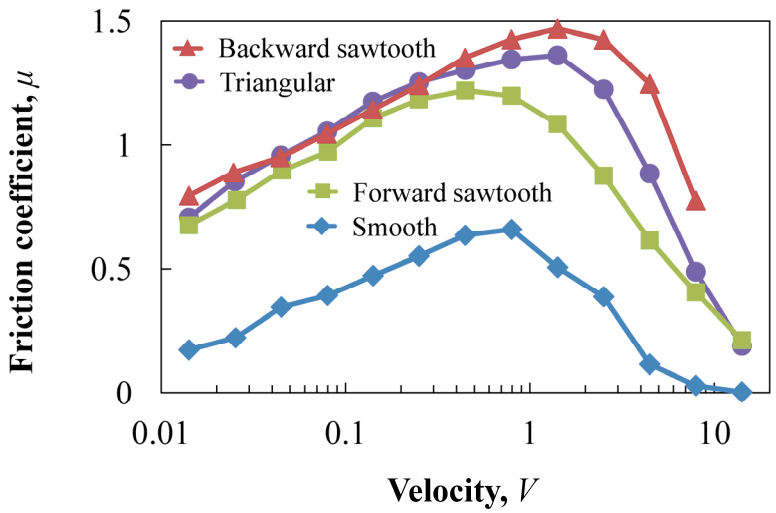

Figure 5.10 Friction coefficient as a function of velocity for sliding on adhesive smooth and grooved substrates (see Figure 5.2). The temperature, dimensionless normal load, and dimensionless attraction coefficient are $k_BT = 0.5$, $P = 0.25$, and $\Lambda = 1/12$, respectively. The network parameters are $N = 2550$ and $C_{ave} = 8$.

estimated to be smaller by a factor of e^{-U/k_BT} where $U = \Lambda r_c^{adh}/4$ is the depth of the attraction potential. This is consistent with the results shown in Figure 5.10. To further test this scaling, in Figure 5.12, we plot $\mu - \overline{V}$ curves for sliding on the smooth walls with three different adhesive strengths. Here, $\overline{V} = V/e^{-U/k_BT}$ is the rescaled velocity. Our simulations reveal that for all three cases the maximum friction takes place when the rescaled velocity is of the order of unity $O(\overline{V}) \sim 1$ indicating that the rescaling provides an accurate approximation for $V_{\max}$.

However, for surfaces with triangular and backward sawtooth asperities, the maximum friction occurs at a higher velocity $V_{\max} \sim 1.4$. The fact that $V_{\max}$ coincides with the velocity of maximum friction for non-adhesive surfaces (Figure 5.5) indicates that for these cases, the energy dissipation in the bulk has a higher contribution than the dissipation at the interface. As the sliding velocity increases, the real area of contact

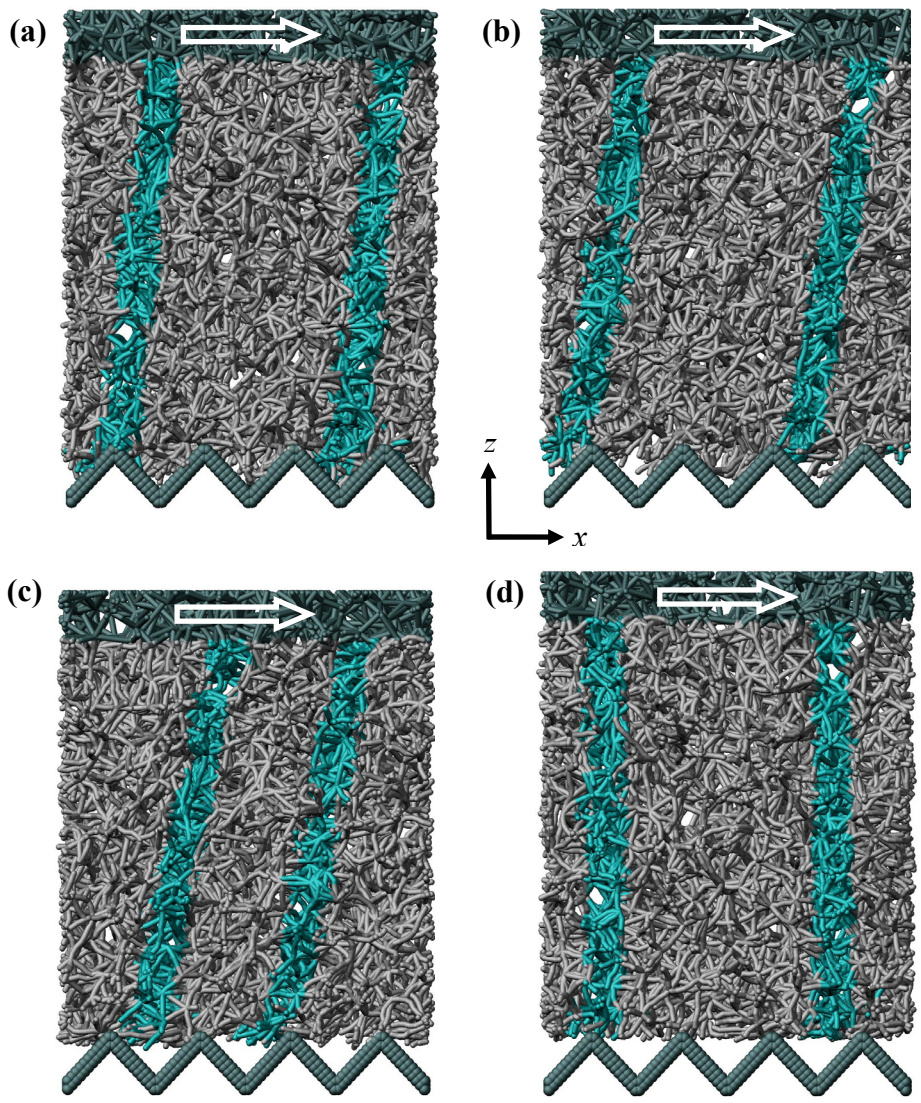

Figure 5.11 Snapshots illustrating the change in the real area of contact between the network and an adhesive wall as the sliding velocity increases. The reduction in the real area of contact is a result of network stiffening due to the increased frequency of periodic deformations (see Figure 5.4b). The temperature, dimensionless normal load, and dimensionless attraction coefficient are $k_BT = 0.5$, $P = 0.25$, and $\Lambda = 1/12$, respectively. The sliding velocity $V\sqrt{k_BT/m}$ in parts (a), (b), (c), and (d) equals to 0.01, 0.1, 1, and 10, respectively. White arrows display the direction of sliding. The cyan strips indicate the network deformation in response to the friction force exerted by the substrate. The network parameters are $N = 2550$ and $C_{ave} = 8$. Only two layers of wall beads are visible (see Figure 5.2).

between the network and counter surfaces decreases (see Figure 5.11). The decrease is

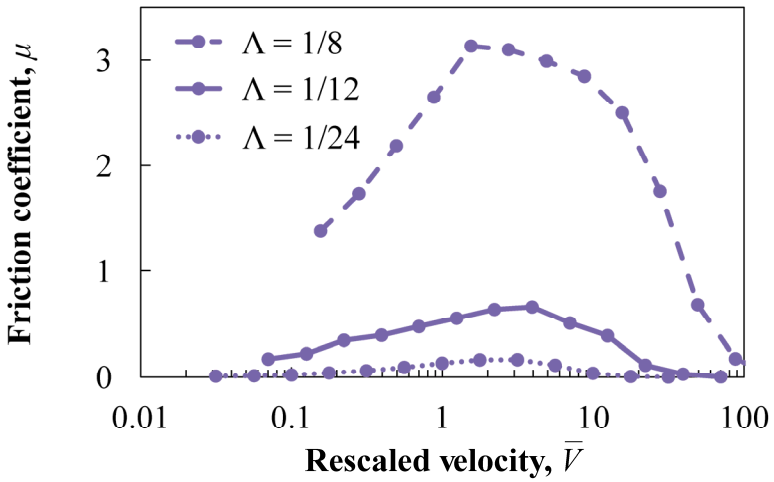

Figure 5.12 Friction coefficient as a function of velocity for sliding on smooth surfaces with different adhesion (see Figure 5.2). The temperature and dimensionless normal load are $k_B T = 0.5$ and $P = 0.25$, respectively. The network parameters are $N = 2550$ and $C_{ave} = 8$.

more pronounced for the surfaces with triangular and backward sawtooth grooves comparing to the wall with forward sawtooth asperities. The energy dissipation at the interface is closely related to the real contact area. Therefore, a higher reduction of the latter leads to a lower contribution of the former in the friction.

The comparison of Figures 5.5 and 5.9 leads to another important observation. In contrast to the hysteretic friction on non-adhesive surfaces, we note that there is a little difference between the adhesive friction of corrugated surfaces with triangular, and forward and backward sawtooth asperities. The results of Figures 5.5 show that the energy dissipated in the bulk is the least for the surface with forward sawtooth asperities and is the highest for the surface with backward sawtooth asperities. However, the energy dissipation at the adhesive interface follows an opposite trend which results in approximately the same friction for walls with different topographies.

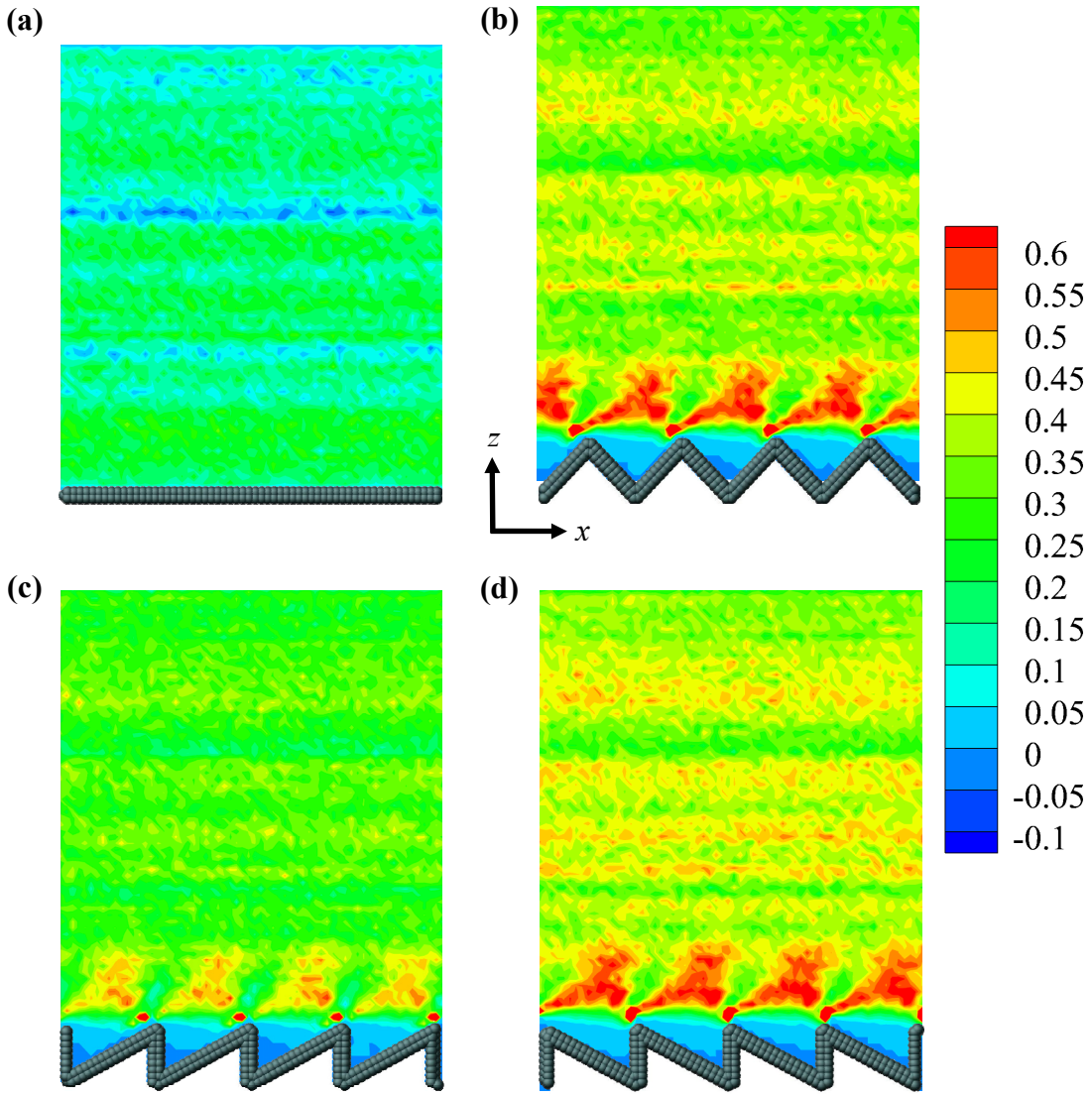

Figure 5.13 Shear stress σ_{xz} distribution in the network sliding on adhesive smooth and grooved surfaces. The stress is averaged over the depth of the network in the y direction and normalized by the shear modulus G. The temperature, dimensionless normal load, and dimensionless attraction coefficient are $k_BT = 0.5$, $P = 0.25$, and $\Lambda = 1/12$, respectively. The sliding velocity in parts (a), (b), (c), and (d) is $V\sqrt{k_BT/m} = 1$. The network parameters are $N = 2550$ and $C_{ave} = 8$. Only two layers of wall beads are visible (see Figure 5.2).

Figure 5.11 displays a trend similar to that observed in Figure 5.7 for the change in the real area of contact as a function of the sliding velocity. However, it is known that,

at a given velocity and normal load, the real area of contact is greater for adhesive surfaces compared to non-adhesive ones. The shear stress distribution for adhesive surfaces (Figure 5.13) is qualitatively similar to that of non-adhesive surfaces (Figure 5.6) except for the regions of high shear stress that are more skewed in the direction of sliding on adhesive surfaces.

Lastly, we probe how the temperature and normal load affect the adhesive friction. In Figure 5.14a, we plot the friction coefficient of the symmetrically corrugated wall versus the sliding velocity for three different temperatures. We see that when $k_B T$ is comparable with U, the friction is maximum at $V_{\max} \sim 1$ whereas at lower temperatures the maximum friction occurs at $V_{\max} e^{-U/k_B T} \sim 1$. This behavior is consistent with the results of Figure 5.12 for the smooth surface and further confirms that when the energy dissipation at the interface is dominant, the friction is maximized at $\overline{V} \sim 1$.

Figure 5.14b illustrates the temperature dependence of μ at a constant sliding velocity for smooth and grooved surfaces. Our calculations reveal that the friction coefficient for all cases decreases rather exponentially with the temperature which is consistent with both theory and experiment [103, 255]. Our results also show a stronger temperature dependence for the smooth surface where the energy is mainly dissipated at the interface. Comparing with Figure 5.8b, we find that the adhesive friction is more sensitive to temperature changes than the hysteretic friction. This is attributed to the strong temperature dependence of energy dissipation at adhesive interfaces [255].

To examine the effect of normal load on the friction on adhesive surfaces, in Figure 5.15a, we plot $\mu - V$ curves of the symmetrically grooved substrate for three different normal loads. Similar to Figure 5.9a, the normal load does not change the

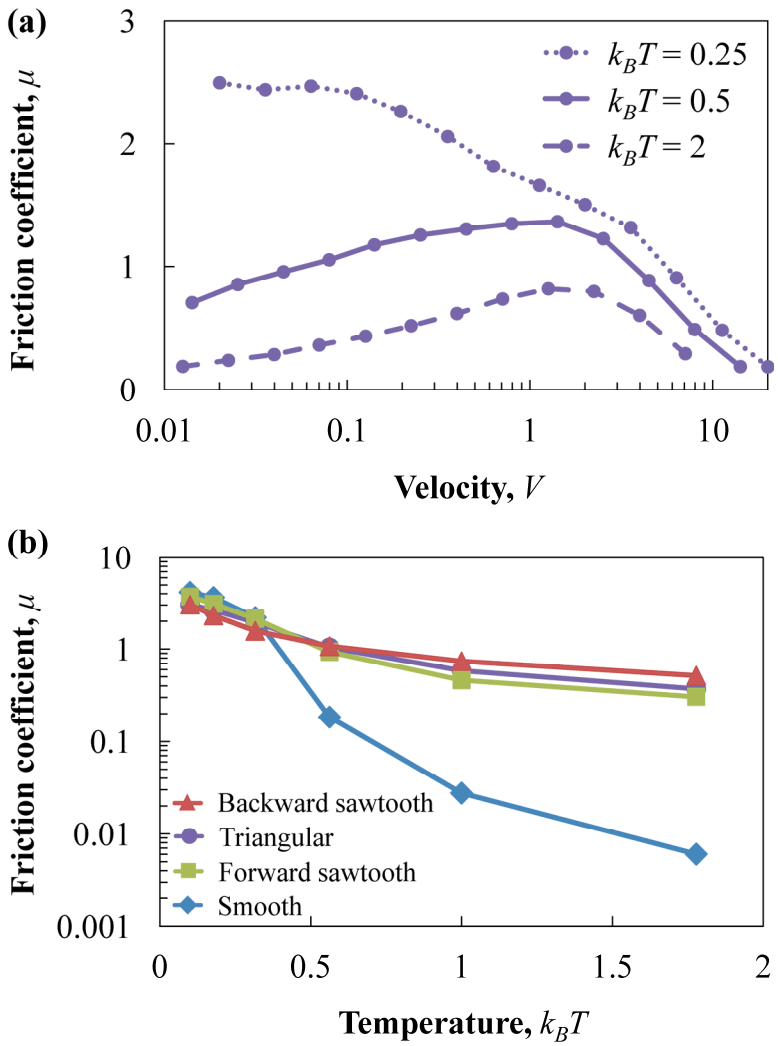

Figure 5.14 (a) Friction coefficient as a function of velocity at different temperatures for sliding on the adhesive grooved surface with triangular asperities (see Figure 5.2). (b) Friction coefficient as a function of temperature for sliding on adhesive smooth and grooved substrates (see Figure 5.2). The sliding velocity is $V\sqrt{k_BT/m} = 0.1$. The dimensionless normal load and attraction coefficient are, respectively, $P = 0.25$ and $\Lambda = 1/12$. The network parameters are $N = 2550$ and $C_{ave} = 8$.

position of the maximum friction. On the contrary, though, the magnitude of μ seems to decrease with increasing normal load. We plot the friction coefficient versus the normal load at a constant velocity and temperature in Figure 5.15b. We find that when the applied pressure is much smaller than the network shear modulus, μ slowly increases

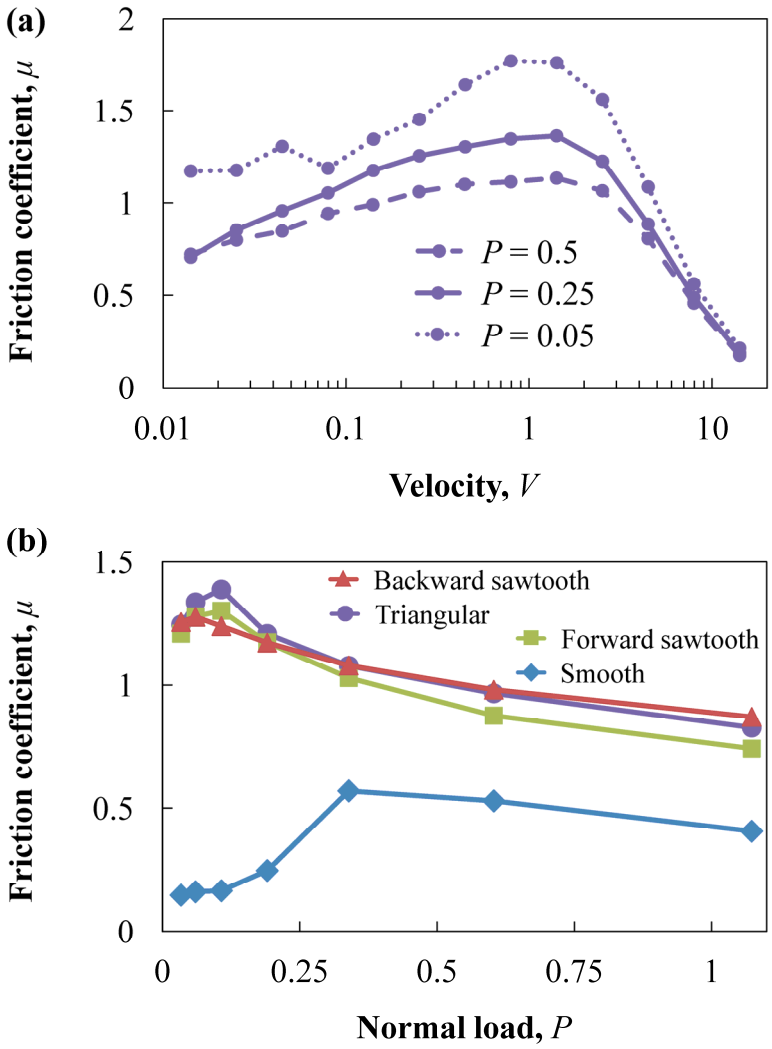

Figure 5.15 (a) Friction coefficient as a function of velocity at different normal loads for sliding on the adhesive grooved surface with triangular asperities (see Figure 5.2). (b) Friction coefficient as a function of normal load for sliding on adhesive smooth and grooved substrates (see Figure 5.2). The sliding velocity is $V\sqrt{k_BT/m} = 0.1$. The temperature and dimensionless attraction coefficient are, respectively, $k_BT = 0.5$ and $\Lambda = 1/12$. The network parameters are $N = 2550$ and $C_{ave} = 8$.

with P. As the normal pressure further increases, however, the friction coefficient decreases as power law of P. This is because the real area of contact does not increase proportionally to the normal load leading to a drop in μ. Prior experimental measurements [102, 259] have indicated that the power law breaks down at sufficiently

high normal loads for which an additional increase in the load does not affect the real area of contact and, therefore, μ decreases linearly with P.

5.5 Experimental Realization

The results of our calculations in this chapter can be readily converted to experimentally realizable values. For instance, our simulations predict that the maximum friction for an elastomer with shear modulus $G \sim 10^5\,\text{Pa}$, $G''/\omega \sim 0.1\,\text{N}\cdot\text{s}/\text{m}^2$, $G_0' - G_\infty' \sim 10^5\,\text{Pa}$, density $\rho_e \sim 10^3\,\text{kg}/\text{m}^3$, and characteristic relaxation time $T_{rel} \sim 10^{-7}\,\text{s}$ at room temperature that slide over a non-adhesive grooved surface with $\lambda \sim H \sim 10^{-6}\,\text{m}$ takes place at velocity $V \sim 10\,\text{m}/\text{s}$. According to our simulations, the maximum friction velocity of the same elastomer sliding over a smooth wall with adhesive energy twice larger than the room-temperature thermal energy is $V \sim 1\,\text{m}/\text{s}$.

5.6 Summary and Future Directions

We used our model for polymer networks to study the frictional behavior of dry elastomers in relative motion against adhesive and non-adhesive surfaces. We considered smooth substrates and those with triangular, forward and backward sawooth asperities. We showed that the friction experienced on non-adhesive surfaces is the lowest for a surface with forward sawtooth roughness, while the surface with backward roughness leads to the highest friction. For adhesive surfaces, our simulations revealed that the friction force is independent of the surface geometry when the sliding velocity is sufficiently slow.

We also examined the effects of sliding velocity, temperature, and normal load on the hysteretic and adhesive friction of our network. In particular, our simulations

predicted a bell-shaped curve for the dependence of the friction coefficient on the sliding velocity. We demonstrated that the velocity at which the friction is maximum depends on the system temperature for the hysteretic friction and is a function of the ratio between the thermal and adhesion energy for the adhesive friction. Moreover, our calculations indicated that at low sliding velocities, both hysteretic and adhesive friction decrease with an increase in the temperature. Finally, we showed that while the coefficient of hysteretic friction is nearly independent of the normal load, the adhesive friction coefficient exhibits an intricate relation with the applied pressure.

Overall, our findings in this chapter shed light on the complex frictional behavior of elastomers and give insights about the effect of roughness asymmetry on the elastomeric friction which could be useful for developing new methods for regulating friction and reducing wear using directional surfaces. In addition, our simulations revealed that our coarse-grained particle-based model for dry viscoelastic networks can be effectively used to predict the influence of system parameters on the friction of elastomers. This opens a new avenue for developing high performance computational tools to analyze the complex tribological response of polymer networks.

As a future direction, our studies could be extended to probe the friction of gels. This requires adding the DPD solvent to our model discussed in this chapter. The presence of a host solvent would alter the frictional response of the network in a non-trivial fashion. For instance, the sliding of a polymer network on a grooved surface in an aqueous environment could lead to the emergence of small scale fluid flows which may substantially influence the friction.

Another direction to extend our work is to consider the sliding of elastomers on soft surfaces. This problem is of high practical importance and, yet, has not been fully explored. The relative stiffness of counter surfaces becomes a critical parameter in this problem. Moreover, elastic instabilities are more likely to develop, especially, when there is an attractive interaction between rubbing surfaces. Additionally, the effects of roughness size and geometry may be somewhat different from the sliding on hard substrates.

CHAPTER 6

CONCLUDING REMARKS AND OUTLOOK

We developed a mesoscale computational model for permanently cross-linked polymer networks. Our model is based on dissipative particle dynamics (DPD), a course-grained molecular dynamics (MD) method that employs a momentum-conserving thermostat and soft repulsive interactions among beads representing clusters of molecules. We showed that our fully-coupled three-dimensional model can successfully simulate the convective and diffusive transport of fluids and solutes through polymer networks. Additionally, we demonstrated that our model is able to capture key features of polymer networks micromechanics.

Using our particle-based model, we studied the permeability and diffusivity of mechanically loaded polymer. The results of our simulations revealed that the transport properties of deformed networks are defined by the network porosity and orientation of network filaments. We characterized the latter by a second order orientation tensor, and showed that the permeability along the principal directions of a deformed network is directly related to the magnitudes of the corresponding tensor components.

We also utilized our coarse-grained model to examine the release of encapsulated solutes from microgel capsules during volume transitions. Our simulations demonstrated that both swelling and deswelling of hollow microcapsules can be used for the controlled release. We showed that the release from swollen capsules is diffusion driven, whereas the release from deswelling gel capsules occurs due to the flow of encapsulated solvent that is expelled from the shrinking capsule interior. The latter hydrodynamic release is

burst-like and continues only during capsule deswelling. We found that by introducing solid microrods inside deswelling capsules, we can control this rapid release. Our simulations indicated that the rods locally stretch the deswelling gel membrane and, thereby, prevent membrane sealing at the early stages of shrinking.

Finally, we employed our model to explore the frictional behavior of elastomers. We considered the sliding friction on adhesive and non-adhesive substrates. We examined how the friction coefficient changes as we vary the sliding velocity, temperature, and normal load. We also scrutinized the effects of roughness size and geometry. Our calculations showed that regardless of surface interactions and roughness shape, the friction coefficient initially increases with the sliding until it reaches the maximum. When the velocity is further increased, the coefficient of friction decreases and nearly vanishes at high enough velocities. We found that, depending on the surface interactions, the maximum friction velocity is determined by the temperature and ratio between the thermal energy of the system and adhesion energy of the counter surface. For the same asperity height and wavelength, our simulations revealed that the friction on non-adhesive walls strongly depends on the isotropy of surface roughness whereas the friction on adhesive substrates is nearly unaffected by the asymmetry of surface asperities at sufficiently low velocities. We also demonstrated that the coefficients of hysteretic and adhesive friction decrease exponentially with temperature when the sliding is slow. Lastly, we showed that the coefficient of hysteretic friction is practically independent of the normal load.

The results of our studies advance the basic understanding of complex dynamic interactions among compliant polymer networks, solutes, and the viscous solvent. In

particular, our studies enhance our knowledge of the convective and diffusive transport in deformed polymer networks, and provide insights into the relations between the network structure and transport properties. Furthermore, our findings enhance our understanding of the function of biological polymer networks and, in this manner, provide insight into the processes taking place in living cells. The outcomes of our calculations establish the engineering guidelines for designing a new type of adaptive and responsive microscopic carriers that can be especially useful for targeted delivery and controlled release of drugs and other solutes. Our friction simulations shed light on the intricate tribological properties of elastomers and provide useful information for regulating friction using geometrical surface patterning.

Our model of cross-linked polymer networks provides a high performance computational tool for future investigations of systems involving active and responsive polymer networks. For instance, our model can be readily used to study the release of solutes from cubic and tetrahedral capsules and probe how capsule geometry affects the rate and duration of release. The sliding friction of elastomers on soft surfaces can be considered as well. As another example, our model can be extended to examine the influence of gradient in the cross-linking density on the transport properties of polymer networks. One could also modify our current model by introducing electrostatic interactions to simulate transport of ions and other charged entities

REFERENCES

[1] C. S. Patrickios, *Polymer Networks: Recent Developments*, Macromolecular Symposia, **291-292** (1): 1-11, 2010.

[2] K. M. Schmoller, P. Fernandez, R. C. Arevalo, D. L. Blair and A. R. Bausch, *Cyclic hardening in bundled actin networks*, Nature Communications, **1**, 2010.

[3] V. M. Tysseling-Mattiace, V. Sahni, K. L. Niece, D. Birch, C. Czeisler, M. G. Fehlings, S. I. Stupp and J. A. Kessler, *Self-assembling nanofibers inhibit glial scar formation and promote axon elongation after spinal cord injury*, Journal of Neuroscience, **28** (14): 3814-3823, 2008.

[4] R. M. Kasi, S. K. Ahn, S. C. Kim, N. Sharma and Y. X. Zhou, *Stimuli-responsive polymer gels*, Soft Matter, **4** (6): 1151-1157, 2008.

[5] Y. Osada and J. P. Gong, *Stimuli-Responsive Polymer Gels and Their Application to Chemomechanical Systems*, Progress in Polymer Science, **18** (2): 187-226, 1993.

[6] M. A. C. Stuart, W. T. S. Huck, J. Genzer, M. Muller, C. Ober, M. Stamm, G. B. Sukhorukov, I. Szleifer, V. V. Tsukruk, M. Urban, F. Winnik, S. Zauscher, I. Luzinov and S. Minko, *Emerging applications of stimuli-responsive polymer materials*, Nature Materials, **9** (2): 101-113, 2010.

[7] M. W. Urban and F. Liu, *Recent advances and challenges in designing stimuli-responsive polymers*, Progress in Polymer Science, **35** (1-2): 3-23, 2010.

[8] Y. Takeoka, A. Bin Imran and T. Seki, *Recent advances in hydrogels in terms of fast stimuli responsiveness and superior mechanical performance*, Polymer Journal, **42** (11): 839-851, 2010.

[9] K. Park and Y. Qiu, *Environment-sensitive hydrogels for drug delivery*, Advanced Drug Delivery Reviews, **53** (3): 321-339, 2001.

[10] T. Miyata, T. Uragami and K. Nakamae, *Biomolecule-sensitive hydrogels*, Advanced Drug Delivery Reviews, **54** (1): 79-98, 2002.

[11] I. Tomatsu, K. Peng and A. Kros, *Photoresponsive hydrogels for biomedical applications*, Advanced Drug Delivery Reviews: DOI: 10.1016/j.addr.2011.1006.1009, 2011.

[12] H. S. Xia, J. K. Wu, X. L. Gong and Y. C. Fan, *Physically crosslinked poly(vinyl alcohol) hydrogels with magnetic field controlled modulus*, Soft Matter, **7** (13): 6205-6212, 2011.

[13] R. T. Olsson, M. A. S. A. Samir, G. Salazar-Alvarez, L. Belova, V. Strom, L. A. Berglund, O. Ikkala, J. Nogues and U. W. Gedde, *Making flexible magnetic aerogels and stiff magnetic nanopaper using cellulose nanofibrils as templates*, Nature Nanotechnology, **5** (8): 584-588, 2010.

[14] S. Maeda, S. Nakamaru, Y. Hara and S. Hashimoto, *Control of Autonomous Swelling - Deswelling Behavior for a Polymer Gel*, Journal of Physical Chemistry B, **113** (14): 4609-4613, 2009.

[15] R. D. Groot and P. B. Warren, *Dissipative particle dynamics: Bridging the gap between atomistic and mesoscopic simulation*, Journal of Chemical Physics, **107** (11): 4423-4435, 1997.

[16] M. Quesada-Perez, J. A. Maroto-Centeno, J. Forcada and R. Hidalgo-Alvarez, *Gel swelling theories: the classical formalism and recent approaches*, Soft Matter, **7** (22): 10536-10547, 2011.

[17] L. S. Zha, B. Banik and F. Alexis, *Stimulus responsive nanogels for drug delivery*, Soft Matter, **7** (13): 5908-5916, 2011.

[18] R. Yoshida, *Design of functional polymer gels and their application to biomimetic materials*, Current Organic Chemistry, **9** (16): 1617-1641, 2005.

[19] G. Huang, J. Gao, Z. B. Hu, J. V. S. John, B. C. Ponder and D. Moro, *Controlled drug release from hydrogel nanoparticle networks*, Journal of Controlled Release, **94** (2-3): 303-311, 2004.

[20] J. Z. Hilt and N. S. Satarkar, *Magnetic hydrogel nanocomposites for remote controlled pulsatile drug release*, Journal of Controlled Release, **130** (3): 246-251, 2008.

[21] A. K. Bajpai, S. K. Shukla, S. Bhanu and S. Kankane, *Responsive polymers in controlled drug delivery*, Progress in Polymer Science, **33** (11): 1088-1118, 2008.

[22] M. Malmsten, H. Bysell and P. Hansson, *Biomacromolecules in microgels - Opportunities and challenges for drug delivery*, Current Opinion in Colloid & Interface Science, **15** (6): 435-444, 2010.

[23] G. B. Sukhorukov, M. F. Bedard, B. G. De Geest, A. G. Skirtach and H. Mohwald, *Polymeric microcapsules with light responsive properties for encapsulation and release*, Advances in Colloid and Interface Science, **158** (1-2): 2-14, 2010.

[24] S. Minko, M. Motornov, Y. Roiter and I. Tokarev, *Stimuli-responsive nanoparticles, nanogels and capsules for integrated multifunctional intelligent systems*, Progress in Polymer Science, **35** (1-2): 174-211, 2010.

[25] S. Seiffert, J. Thiele, A. R. Abate and D. A. Weitz, *Smart Microgel Capsules from Macromolecular Precursors*, Journal of the American Chemical Society, **132** (18): 6606-6609, 2010.

[26] S. Minko and I. Tokarev, *Stimuli-Responsive Porous Hydrogels at Interfaces for Molecular Filtration, Separation, Controlled Release, and Gating in Capsules and Membranes*, Advanced Materials, **22** (31): 3446-3462, 2010.

[27] A. G. Skirtach, M. Delcea and H. Mohwald, *Stimuli-responsive LbL capsules and nanoshells for drug delivery*, Advanced Drug Delivery Reviews, **63** (9): 730-747, 2011.

[28] D. F. Moore and W. Geyer, *Review of Adhesion Theories for Elastomers*, Wear, **22** (2): 113-&, 1972.

[29] B. N. J. Persson, *Rubber friction and tire dynamics*, Journal of Physics-Condensed Matter, **23** (1), 2011.

[30] S. W. Zhang, *Tribology of elastomers*. Elsevier Science, 2004.

[31] R. F. Salant, *Theory of lubrication of elastomeric rotary shaft seals*, Proceedings of the Institution of Mechanical Engineers Part J-Journal of Engineering Tribology, **213** (J3): 189-201, 1999.

[32] R. Elleuch, K. Elleuch, H. Ben Abdelounis and H. Zahouani, *Surface roughness effect on friction behaviour of elastomeric material*, Materials Science and Engineering a-Structural Materials Properties Microstructure and Processing, **465** (1-2): 8-12, 2007.

[33] F. Wu-Bavouzet, J. Cayer-Barrioz, A. Le Bot, F. Brochard-Wyart and A. Buguin, *Effect of surface pattern on the adhesive friction of elastomers*, Physical Review E, **82** (3), 2010.

[34] M. J. Hancock, K. Sekeroglu and M. C. Demirel, *Bioinspired Directional Surfaces for Adhesion, Wetting, and Transport*, Advanced Functional Materials, **22** (11): 2223-2234, 2012.

[35] E. Degrandi-Contraires, C. Poulard, F. Restagno and L. Leger, *Sliding friction at soft micropatterned elastomer interfaces*, Faraday Discussions, 2012.

[36] S. Tawfick, M. De Volder, D. Copic, S. J. Park, C. R. Oliver, E. S. Polsen, M. J. Roberts and A. J. Hart, *Engineering of Micro- and Nanostructured Surfaces with Anisotropic Geometries and Properties*, Advanced Materials, **24** (13): 1628-1674, 2012.

[37] E. W. Durbin and G. A. Buxton, *A coarse-grained model of targeted drug delivery from responsive polymer nanoparticles*, Soft Matter, **6** (4): 762-767, 2010.

[38] N. Park, S. H. Um, H. Funabashi, J. Xu and D. Luo, *A cell-free protein-producing gel*, Nature Materials, **8** (5): 432-437, 2009.

[39] X. M. Chen, A. C. Dunn, W. G. Sawyer and M. Sarntinoranont, *A biphasic model for micro-indentation of a hydrogel-based contact lens*, Journal of Biomechanical Engineering-Transactions of the ASME, **129** (2): 156-163, 2007.

[40] D. W. Hutmacher, *Biomaterials offer cancer research the third dimension*, Nature Materials, **9** (2): 90-93, 2010.

[41] Y. Murase, S. Maeda, S. Hashimoto and R. Yoshida, *Design of a Mass Transport Surface Utilizing Peristaltic Motion of a Self-Oscillating Gel*, Langmuir, **25** (1): 483-489, 2009.

[42] P. Dayal, O. Kuksenok and A. C. Balazs, *Designing autonomously motile gels that follow complex paths*, Soft Matter, **6** (4): 768-773, 2010.

[43] M. Shingo, Y. Hara, R. Yoshida and S. Hashimoto, *Chemical robot-Design of self-walking gel-*, In Proceedings of the Intelligent Robots and Systems, 2007. IROS 2007. IEEE/RSJ International Conference on2150-2155, 2007.

[44] R. Daganl, *Intelligent gels*, Chemical & Engineering News, **75** (23): 26-37, 1997.

[45] R. Barbucci, B. D. Ratner and S. Atzet, in *Hydrogels* Springer Milan: pp. 43-51, 2009.

[46] N. Ter-Oganessian, D. A. Pink and A. Boulbitch, *Active microrheology of networks composed of semiflexible polymers: Theory and comparison with simulations*, Physical Review E, **72** (4), 2005.

[47] J. M. Mansour and V. C. Mow, *Permeability of Articular-Cartilage under Compressive Strain and at High-Pressures*, Journal of Bone and Joint Surgery-American Volume, **58** (4): 509-516, 1976.

[48] S. Whitaker, *Flow in porous media I: A theoretical derivation of Darcy's law*, Transport in Porous Media, **1** (1): 3-25, 1986.

[49] G. D. J. Phillies, *The Hydrodynamic Scaling Model for Polymer Self-Diffusion*, Journal of Physical Chemistry, **93** (13): 5029-5039, 1989.

[50] G. D. J. Phillies, T. Pirnat, M. Kiss, N. Teasdale, D. Maclung, H. Inglefield, C. Malone, A. Rau, L. P. Yu and J. Rollings, *Probe diffusion in solutions of low-molecular-weight polyelectrolytes*, Macromolecules, **22** (10): 4068-4075, 1989.

[51] D. S. Clague and R. J. Phillips, *A numerical calculation of the hydraulic permeability of three-dimensional disordered fibrous media*, Physics of Fluids, **9** (6): 1562-1572, 1997.

[52] J. C. Bosma and J. A. Wesselingh, *Partitioning and diffusion of large molecules in fibrous structures*, Journal of Chromatography B, **743** (1-2): 169-180, 2000.

[53] W. Y. Gu, H. Yao, C. Y. Huang and H. S. Cheung, *New insight into deformation-dependent hydraulic permeability of gels and cartilage, and dynamic behavior of agarose gels in confined compression*, Journal of Biomechanics, **36** (4): 593-598, 2003.

[54] B. Markert, *A constitutive approach to 3-d nonlinear fluid flow through finite deformable porous continua - With application to a high-porosity polyurethane foam*, Transport in Porous Media, **70** (3): 427-450, 2007.

[55] D. Mu, Z. S. Liu, C. Huang and N. Djilali, *Determination of the effective diffusion coefficient in porous media including Knudsen effects*, Microfluidics and Nanofluidics, **4** (3): 257-260, 2008.

[56] T. Stylianopoulos, A. Yeckel, J. J. Derby, X. J. Luo, M. S. Shephard, E. A. Sander and V. H. Barocas, *Permeability calculations in three-dimensional isotropic and oriented fiber networks*, Physics of Fluids, **20** (12): 123601, 2008.

[57] Y. Cu and W. M. Saltzman, *Mathematical modeling of molecular diffusion through mucus*, Advanced Drug Delivery Reviews, **61** (2): 101-114, 2009.

[58] W. M. Saltzman, M. L. Radomsky, K. J. Whaley and R. A. Cone, *Antibody Diffusion in Human Cervical-Mucus*, Biophysical Journal, **66** (2): 508-515, 1994.

[59] P. L. Chandran, T. Stylianopoulos and V. H. Barocas, *Microstructure-based, multiscale modeling for the mechanical behavior of hydrated fiber networks*, Multiscale Modeling & Simulation, **7** (1): 22-43, 2008.

[60] C. Heussinger, B. Schaefer and E. Frey, *Nonaffine rubber elasticity for stiff polymer networks*, Physical Review E, **76** (3): 031906, 2007.

[61] J. Wilhelm and E. Frey, *Elasticity of stiff polymer networks*, Physical Review Letters, **91** (10): 108103, 2003.

[62] A. E. X. Brown, R. I. Litvinov, D. E. Discher, P. K. Purohit and J. W. Weisel, *Multiscale Mechanics of Fibrin Polymer: Gel Stretching with Protein Unfolding and Loss of Water*, Science, **325** (5941): 741-744, 2009.

[63] D. A. Fletcher and D. Mullins, *Cell mechanics and the cytoskeleton*, Nature, **463** (7280): 485-492, 2010.

[64] K. A. Erk, K. J. Henderson and K. R. Shull, *Strain Stiffening in Synthetic and Biopolymer Networks*, Biomacromolecules, **11** (5): 1358-1363, 2010.

[65] F. Urciuolo, G. Imparato and P. A. Netti, *Effect of dynamic loading on solute transport in soft gels implication for drug delivery*, Aiche Journal, **54** (3): 824-834, 2008.

[66] A. Caspi, R. Granek and M. Elbaum, *Enhanced diffusion in active intracellular transport*, Physical Review Letters, **85** (26): 5655-5658, 2000.

[67] E. M. Huisman, C. Storm and G. T. Barkema, *Monte Carlo study of multiply crosslinked semiflexible polymer networks*, Physical Review E, **78** (5), 2008.

[68] S. B. Lindstrom, D. A. Vader, A. Kulachenko and D. A. Weitz, *Biopolymer network geometries: Characterization, regeneration, and elastic properties*, Physical Review E, **82** (5), 2010.

[69] V. Klepko, Y. Melnichenko and V. Shilov, *Liquid flow through polymer gels*, Polymer Gels and Networks, **4** (4): 351-361, 1996.

[70] D. P. Holmes, M. Roche, T. Sinha and H. A. Stone, *Bending and twisting of soft materials by non-homogenous swelling*, Soft Matter, **7** (11): 5188-5193, 2011.

[71] J. U. Sommer, R. Dockhorn, P. B. Welzel, U. Freudenberg and C. Werner, *Swelling Equilibrium of a Binary Polymer Gel*, Macromolecules, **44** (4): 981-986, 2011.

[72] Y. L. Li, D. Maciel, H. Tomas, J. Rodrigues, H. Ma and X. Y. Shi, *pH sensitive Laponite/alginate hybrid hydrogels: swelling behaviour and release mechanism*, Soft Matter, **7** (13): 6231-6238, 2011.

[73] S. Y. Xing, Y. Guan and Y. J. Zhang, *Kinetics of Glucose-Induced Swelling of P(NIPAM-AAPBA) Microgels*, Macromolecules, **44** (11): 4479-4486, 2011.

[74] H. H. Dai and Z. L. Song, *Some analytical formulas for the equilibrium states of a swollen hydrogel shell*, Soft Matter, **7** (18): 8473-8483, 2011.

[75] P. K. Jha, J. W. Zwanikken, F. A. Detcheverry, J. J. de Pablo and M. O. de la Cruz, *Study of volume phase transitions in polymeric nanogels by theoretically informed coarse-grained simulations*, Soft Matter, **7** (13): 5965-5975, 2011.

[76] M. Caldorera-Moore, M. K. Kang, Z. Moore, V. Singh, S. V. Sreenivasan, L. Shi, R. Huang and K. Roy, *Swelling behavior of nanoscale, shape- and size-specific, hydrogel particles fabricated using imprint lithography*, Soft Matter, **7** (6): 2879-2887, 2011.

[77] T. Sakai, M. Kurakazu, Y. Akagi, M. Shibayama and U. Chung, *Effect of swelling and deswelling on the elasticity of polymer networks in the dilute to semi-dilute region*, Soft Matter, **8** (9): 2730-2736, 2012.

[78] B. Xu, X. J. Di and G. B. McKenna, *Swelling Behavior of Cross-Linked Rubber: Explanation of the Elusive Peak in the Swelling Activity Parameter (Dilational Modulus)*, Macromolecules, **45** (5): 2402-2410, 2012.

[79] H. Q. Jiang, J. P. Zhang, X. H. Zhao and Z. G. Suo, *A finite element method for transient analysis of concurrent large deformation and mass transport in gels*, J. Appl. Phys., **105** (9), 2009.

[80] V. V. Yashin and A. C. Balazs, *Pattern formation and shape changes in self-oscillating polymer gels*, Science, **314** (5800): 798-801, 2006.

[81] J. P. Keener, S. Sircar and A. L. Fogelson, *Influence of the standard free energy on swelling kinetics of gels*, Physical Review E, **83** (4), 2011.

[82] J. Wahrmund, J. W. Kim, L. Y. Chu, C. J. Wang, Y. Li, A. Fernandez-Nieves, D. A. Weitz, A. Krokhin and Z. B. Hu, *Swelling Kinetics of a Microgel Shell*, Macromolecules, **42** (23): 9357-9365, 2009.

[83] P. A. L. Fernandes, S. Schmidt, M. Zeiser, A. Fery and T. Hellweg, *Swelling and mechanical properties of polymer gels with cross-linking gradient*, Soft Matter, **6** (15): 3455-3458, 2010.

[84] C. Y. Gao, S. Leporatti, S. Moya, E. Donath and H. Mohwald, *Swelling and shrinking of polyelectrolyte microcapsules in response to changes in temperature and ionic strength*, Chemistry-a European Journal, **9** (4): 915-920, 2003.

[85] D. A. Head, A. J. Levine and F. C. MacKintosh, *Deformation of cross-linked semiflexible polymer networks*, Physical Review Letters, **91** (10): 108102, 2003.

[86] J. Liu, G. H. Koenderink, K. E. Kasza, F. C. MacKintosh and D. A. Weitz, *Visualizing the strain field in semiflexible polymer networks: Strain fluctuations and nonlinear rheology of F-actin gels*, Physical Review Letters, **98** (19): 198304, 2007.

[87] G. A. Buxton and N. Clarke, *"Bending to stretching" transition in disordered networks*, Physical Review Letters, **98** (23): 238103, 2007.

[88] E. A. Sander, T. Stylianopoulos, R. T. Tranquillo and V. H. Barocas, *Image-based multiscale modeling predicts tissue-level and network-level fiber reorganization in stretched cell-compacted collagen gels*, Proceedings of the National Academy of Sciences of the United States of America, **106** (42): 17675-17680, 2009.

[89] G. H. Koenderink, Z. Dogic, F. Nakamura, P. M. Bendix, F. C. MacKintosh, J. H. Hartwig, T. P. Stossel and D. A. Weitz, *An active biopolymer network controlled by molecular motors*, Proceedings of the National Academy of Sciences of the United States of America, **106** (36): 15192-15197, 2009.

[90] S. Ulrich, X. Mao, P. M. Goldbart and A. Zippelius, *Elasticity of highly cross-linked random networks*, Europhysics Letters, **76** (4): 677-682, 2006.

[91] O. Lieleg, M. M. A. E. Claessens and A. R. Bausch, *Structure and dynamics of cross-linked actin networks*, Soft Matter, **6** (2): 218-225, 2010.

[92] J. P. Gong, *Why are double network hydrogels so tough?*, Soft Matter, **6** (12): 2583-2590, 2010.

[93] M. A. Tahir and H. V. Tafreshi, *Influence of fiber orientation on the transverse permeability of fibrous media*, Physics of Fluids, **21** (8): 083604, 2009.

[94] A. Nabovati, E. W. Llewellin and A. C. M. Sousa, *A general model for the permeability of fibrous porous media based on fluid flow simulations using the lattice Boltzmann method*, Composites Part a-Applied Science and Manufacturing, **40** (6-7): 860-869, 2009.

[95] G. W. Jackson and D. F. James, *The Permeability of Fibrous Porous-Media*, Canadian Journal of Chemical Engineering, **64** (3): 364-374, 1986.

[96] A. F. Morais, H. Seybold, H. J. Herrmann and J. S. Andrade, *Non-Newtonian Fluid Flow through Three-Dimensional Disordered Porous Media*, Physical Review Letters, **103** (19): 194502, 2009.

[97] T. Sochi, *Non-Newtonian flow in porous media*, Polymer, **51** (22): 5007-5023, 2010.

[98] L. Liu, P. S. Li and S. A. Asher, *Entropic trapping of macromolecules by mesoscopic periodic voids in a polymer hydrogel*, Nature, **397** (6715): 141-144, 1999.

[99] S. Seiffert and W. Oppermann, *Diffusion of linear macromolecules and spherical particles in semidilute polymer solutions and polymer networks*, Polymer, **49** (19): 4115-4126, 2008.

[100] A. Le Gal, X. Yang and M. Kluppel, *Evaluation of sliding friction and contact mechanics of elastomers based on dynamic-mechanical analysis*, Journal of Chemical Physics, **123** (1), 2005.

[101] D. F. Moore and W. Geyer, *Review of Hysteresis Theories for Elastomers*, Wear, **30** (1): 1-34, 1974.

[102] A. Schallamach, *The Load Dependence of Rubber Friction*, Proceedings of the Physical Society of London Section B, **65** (393): 657-661, 1952.

[103] A. Schallamach, *The Velocity and Temperature Dependence of Rubber Friction*, Proceedings of the Physical Society of London Section B, **66** (401): 386-392, 1953.

[104] K. A. Grosch, *Relation between Friction and Visco-Elastic Properties of Rubber*, Nature, **197** (487): 858-&, 1963.

[105] B. N. J. Persson and E. Tosatti, *Qualitative theory of rubber friction and wear*, Journal of Chemical Physics, **112** (4): 2021-2029, 2000.

[106] B. N. J. Persson, *On the theory of rubber friction*, Surface Science, **401** (3): 445-454, 1998.

[107] A. R. Savkoor, *Mechanics of Sliding Friction of Elastomers*, Wear, **113** (1): 37-60, 1986.

[108] N. K. Myshkin, M. I. Petrokovets and A. V. Kovalev, *Tribology of polymers: Adhesion, friction, wear, and mass-transfer*, Tribology International, **38** (11-12): 910-921, 2005.

[109] Q. V. Bui and J. P. Ponthot, *Estimation of rubber sliding friction from asperity interaction modeling*, Wear, **252** (1-2): 150-160, 2002.

[110] P. Wriggers and J. Reinelt, *Multi-scale approach for frictional contact of elastomers on rough rigid surfaces*, Computer Methods in Applied Mechanics and Engineering, **198** (21-26): 1996-2008, 2009.

[111] A. K. Singh and V. A. Juvekar, *Steady dynamic friction at elastomer-hard solid interface: A model based on population balance of bonds*, Soft Matter, **7** (22): 10601-10611, 2011.

[112] R. J. Pinnington, *Rubber friction on rough and smooth surfaces*, Wear, **267** (9-10): 1653-1664, 2009.

[113] G. Carbone, B. Lorenz, B. N. J. Persson and A. Wohlers, *Contact mechanics and rubber friction for randomly rough surfaces with anisotropic statistical properties*, European Physical Journal E, **29** (3): 275-284, 2009.

[114] M. Du, Y. Maki, T. Tominaga, H. Furukawa, J. P. Gong, Y. Osada and Q. Zheng, *Friction of soft gel in dilute polymer solution*, Macromolecules, **40** (12): 4313-4321, 2007.

[115] D. P. Chang, J. E. Dolbow and S. Zauscher, *Switchable friction of stimulus-responsive hydrogels*, Langmuir, **23** (1): 250-257, 2007.

[116] K. Kamada, H. Furukawa, T. Kurokawa, T. Tada, T. Tominaga, Y. Nakano and J. P. Gong, *Surfactant-induced friction reduction for hydrogels in the boundary lubrication regime*, Journal of Physics-Condensed Matter, **23** (28), 2011.

[117] A. Dedinaite, E. Thormann, G. Olanya, P. M. Claesson, B. Nystrom, A. L. Kjoniksen and K. Z. Zhu, *Friction in aqueous media tuned by temperature-responsive polymer layers*, Soft Matter, **6** (11): 2489-2498, 2010.

[118] M. Takata, T. Yamaguchi and M. Doi, *Friction Control of a Gel by Electric Field in Ionic Surfactant Solution*, Journal of the Physical Society of Japan, **79** (6), 2010.

[119] J. P. Gong, *Friction and lubrication of hydrogels - its richness and complexity*, Soft Matter, **2** (7): 544-552, 2006.

[120] J. Gong and Y. Osada, *Gel friction: a model based on surface repulsion and adsorption*, The Journal of chemical physics, **109** (18): 8062-8068, 1998.

[121] Y. Osada, J. P. Gong, Y. Iwasaki, K. Kurihara and Y. Hamai, *Friction of gels. 3. Friction on solid surfaces*, Journal of Physical Chemistry B, **103** (29): 6001-6006, 1999.

[122] G. Kagata, J. P. Gong and Y. Osada, *Friction of gels. 6. Effects of sliding velocity and viscoelastic responses of the network*, Journal of Physical Chemistry B, **106** (18): 4596-4601, 2002.

[123] J. P. Gong, T. Tominaga, N. Takedomi, H. Biederman, H. Furukawa and Y. Osada, *Effect of substrate adhesion and hydrophobicity on hydrogel friction*, Soft Matter, **4** (5): 1033-1040, 2008.

[124] S. Momozono, K. Nakamura and K. Kyogoku, *Theoretical model for adhesive friction between elastomers and rough solid surfaces*, Journal of Chemical Physics, **132** (11), 2010.

[125] E. A. Sander, A. M. Stein, M. J. Swickrath and V. H. Barocas, edited by T. Dumitrica Springer Netherlands, **Vol. 9**: pp. 557-602, 2010.

[126] E. Moeendarbary, T. Y. Ng and M. Zangeneh, *Dissipative Particle Dynamics in Soft Matter and Polymeric Applications - a Review*, International Journal of Applied Mechanics, **2** (1): 161-190, 2010.

[127] J. Sweeney, *A comparison of three polymer network models in current use*, Computational and Theoretical Polymer Science, **9** (1): 27-33, 1999.

[128] P. J. Hoogerbrugge and J. M. V. A. Koelman, *Simulating Microscopic Hydrodynamic Phenomena with Dissipative Particle Dynamics*, Europhysics Letters, **19** (3): 155-160, 1992.

[129] T. Steiner, C. Cupelli, R. Zengerle and M. Santer, *Simulation of advanced microfluidic systems with dissipative particle dynamics*, Microfluidics and Nanofluidics, **7** (3): 307-323, 2009.

[130] N. Filipovic, M. Kojic and M. Ferrari, *Dissipative particle dynamics simulation of circular and elliptical particles motion in 2D laminar shear flow*, Microfluidics and Nanofluidics, **10** (5): 1127-1134, 2011.

[131] H. Masoud and A. Alexeev, *Controlled Release of Nanoparticles and Macromolecules from Responsive Microgel Capsules*, ACS Nano, **6** (1): 212-219, 2012.

[132] S. Chen, N. Phan-Thien, X. J. Fan and B. C. Khoo, *Dissipative particle dynamics simulation of polymer drops in a periodic shear flow*, Journal of Non-Newtonian Fluid Mechanics, **118** (1): 65-81, 2004.

[133] A. Alexeev, W. E. Uspal and A. C. Balazs, *Harnessing Janus nanoparticles to create controllable pores in membranes*, ACS Nano, **2** (6): 1117-1122, 2008.

[134] D. A. Fedosov, G. E. Karniadakis and B. Caswell, *Dissipative particle dynamics simulation of depletion layer and polymer migration in micro- and nanochannels for dilute polymer solutions*, Journal of Chemical Physics, **128** (14): 144903, 2008.

[135] H. Masoud and A. Alexeev, *Selective control of surface properties using hydrodynamic interactions*, Chemical Communications, **47** (1): 472-474, 2011.

[136] H. Masoud and A. Alexeev, *Permeability and Diffusion through Mechanically Deformed Random Polymer Networks*, Macromolecules, **43** (23): 10117-10122, 2010.

[137] X. J. Fan, N. Phan-Thien, S. Chen, X. H. Wu and T. Y. Ng, *Simulating flow of DNA suspension using dissipative particle dynamics*, Physics of Fluids, **18** (6): 063102, 2006.

[138] J. R. Spaeth, I. G. Kevrekidis and A. Z. Panagiotopoulos, *Dissipative particle dynamics simulations of polymer-protected nanoparticle self-assembly*, Journal of Chemical Physics, **135** (18), 2011.

[139] M. Basan, J. Prost, J. F. Joanny and J. Elgeti, *Dissipative particle dynamics simulations for biological tissues: rheology and competition*, Physical Biology, **8** (2), 2011.

[140] Y. R. Sliozberg, J. W. Andzelm, J. K. Brennan, M. R. Vanlandingham, V. Pryamitsyn and V. Ganesan, *Modeling Viscoelastic Properties of Triblock Copolymers: A DPD Simulation Study*, Journal of Polymer Science Part B-Polymer Physics, **48** (1): 15-25, 2010.

[141] M. B. Liu, P. Meakin and H. Huang, *Dissipative particle dynamics simulation of multiphase fluid flow in microchannels and microchannel networks*, Physics of Fluids, **19** (3), 2007.

[142] K. Yang and Y. Q. Ma, *Computer simulation of the translocation of nanoparticles with different shapes across a lipid bilayer*, Nature Nanotechnology, **5** (8): 579-583, 2010.

[143] F. Goujon, A. Ghoufi, P. Malfreyt and D. J. Tildesley, *Frictional forces in polyelectrolyte brushes: effects of sliding velocity, solvent quality and salt*, Soft Matter, **8** (17): 4635-4644, 2012.

[144] S. Pal and C. Seidel, *Dissipative particle dynamics simulations of polymer brushes: Comparison with molecular dynamics simulations*, Macromolecular Theory and Simulations, **15** (9): 668-673, 2006.

[145] P. Espanol and P. Warren, *Statistical-Mechanics of Dissipative Particle Dynamics*, Europhysics Letters, **30** (4): 191-196, 1995.

[146] I. V. Pivkin and G. E. Karniadakis, *A new method to impose no-slip boundary conditions in dissipative particle dynamics*, Journal of Computational Physics, **207** (1): 114-128, 2005.

[147] M. Revenga, I. Zuniga and P. Espanol, *Boundary conditions in dissipative particle dynamics*, Computer Physics Communications, **121**: 309-311, 1999.

[148] A. M. Altenhoff, J. H. Walther and P. Koumoutsakos, *A stochastic boundary forcing for dissipative particle dynamics*, Journal of Computational Physics, **225** (1): 1125-1136, 2007.

[149] D. A. Fedosov, I. V. Pivkin and G. E. Karniadakis, *Velocity limit in DPD simulations of wall-bounded flows*, Journal of Computational Physics, **227** (4): 2540-2559, 2008.

[150] N. A. Spenley, *Scaling laws for polymers in dissipative particle dynamics*, Europhysics Letters, **49** (4): 534-540, 2000.

[151] M. D. Graham, *Fluid Dynamics of Dissolved Polymer Molecules in Confined Geometries*, Annual Review of Fluid Mechanics, Vol 43, **43**: 273-298, 2011.

[152] W. X. Pan, D. A. Fedosov, G. E. Karniadakis and B. Caswell, *Hydrodynamic interactions for single dissipative-particle-dynamics particles and their clusters and filaments*, Physical Review E, **78** (4): 46706, 2008.

[153] L. Spielman and S. L. Goren, *Model for predicting pressure drop and filtration efficiency in fibrous media*, Environmental Science & Technology, **2** (4): 279-287, 1968.

[154] G. Kasper, T. Niida and M. Yang, *Measurements of Viscous Drag on Cylinders and Chains of Spheres with Aspect Ratios between 2 and 50*, Journal of Aerosol Science, **16** (6): 535-556, 1985.

[155] J. H. Irving and J. G. Kirkwood, *The Statistical Mechanical Theory of Transport Processes .4. The Equations of Hydrodynamics*, Journal of Chemical Physics, **18** (6): 817-829, 1950.

[156] A. M. Stein, D. A. Vader, D. A. Weitz and L. M. Sander, *The Micromechanics of Three-Dimensional Collagen-I Gels*, Complexity, **16** (4): 22-28, 2011.

[157] A. V. Dobrynin and J. M. Y. Carrillo, *Universality in Nonlinear Elasticity of Biological and Polymeric Networks and Gels*, Macromolecules, **44** (1): 140-146, 2011.

[158] A. W. Lees and S. F. Edwards, *Computer Study of Transport Processes under Extreme Conditions*, Journal of Physics Part C Solid State Physics, **5** (15): 1921-&, 1972.

[159] T. Kim, W. Hwang, H. Lee and R. D. Kamm, *Computational Analysis of Viscoelastic Properties of Crosslinked Actin Networks*, Plos Computational Biology, **5** (7), 2009.

[160] M. L. Gardel, K. E. Kasza, C. P. Brangwynne, J. Y. Liu and D. A. Weitz, *Mechanical Response of Cytoskeletal Networks*, Biophysical Tools for Biologists, Vol 2: In Vivo Techniques, **89**: 487-+, 2008.

[161] N. A. Peppas, J. Z. Hilt, A. Khademhosseini and R. Langer, *Hydrogels in biology and medicine: From molecular principles to bionanotechnology*, Advanced Materials, **18** (11): 1345-1360, 2006.

[162] R. Langer and D. A. Tirrell, *Designing materials for biology and medicine*, Nature, **428** (6982): 487-492, 2004.

[163] O. Kreft, A. M. Javier, G. B. Sukhorukov and W. J. Parak, *Polymer microcapsules as mobile local pH-sensors*, Journal of Materials Chemistry, **17** (42): 4471-4476, 2007.

[164] I. Gorelikov, L. M. Field and E. Kumacheva, *Hybrid microgels photoresponsive in the near-infrared spectral range*, Journal of the American Chemical Society, **126** (49): 15938-15939, 2004.

[165] I. Tomatsu, K. Peng and A. Kros, *Photoresponsive hydrogels for biomedical applications*, Advanced Drug Delivery Reviews, **63** (14-15): 1257-1266, 2011.

[166] T. Tanaka and D. J. Fillmore, *Kinetics of Swelling of Gels*, Journal of Chemical Physics, **70** (3): 1214-1218, 1979.

[167] G. A. Buxton, *The fate of a polymer nanoparticle subject to flow-induced shear stresses*, Epl, **84** (2): 26006, 2008.

[168] A. Jackson and W. Gu, *Transport Properties of Cartilaginous Tissues*, Current rheumatology reviews, **5** (1): 40, 2009.

[169] R. L. Mauck, C. T. Hung and G. A. Ateshian, *Modeling of neutral solute transport in a dynamically loaded porous permeable gel: Implications for articular cartilage biosynthesis and tissue engineering*, Journal of Biomechanical Engineering-Transactions of the Asme, **125** (5): 602-614, 2003.

[170] C. P. Brangwynne, G. H. Koenderink, F. C. MacKintosh and D. A. Weitz, *Intracellular transport by active diffusion*, Trends in Cell Biology, **19** (9): 423-427, 2009.

[171] J. Li, J. K. Park, R. B. Moore and L. A. Madsen, *Linear coupling of alignment with transport in a polymer electrolyte membrane*, Nature Materials, **10** (7): 507-511, 2011.

[172] J. K. Park, J. Li, G. M. Divoux, L. A. Madsen and R. B. Moore, *Oriented Morphology and Anisotropic Transport in Uniaxially Stretched Perfluorosulfonate Ionomer Membranes*, Macromolecules, **44** (14): 5701-5710, 2011.

[173] D. Vader, A. Kabla, D. Weitz and L. Mahadevan, *Strain-Induced Alignment in Collagen Gels*, Plos One, **4** (6), 2009.

[174] Batchelo.Gk, *Slender-Body Theory for Particles of Arbitrary Cross-Section in Stokes Flow*, Journal of Fluid Mechanics, **44** (Nov26): 419-&, 1970.

[175] M. Irie, *Stimuli-responsive polymer gels: An approach to micro actuators*, Microchemical Journal: 363-371, 1994.

[176] S. Nayak and L. A. Lyon, *Soft nanotechnology with soft nanoparticles*, Angewandte Chemie-International Edition, **44** (47): 7686-7708, 2005.

[177] A. Fery, F. Dubreuil and H. Mohwald, *Mechanics of artificial microcapsules*, New Journal of Physics, **6**: 18, 2004.

[178] O. I. Vinogradova, O. V. Lebedeva and B. S. Kim, *Mechanical behavior and characterization of microcapsules*, Annual Review of Materials Research, **36**: 143-178, 2006.

[179] R. Arshady, *Microspheres and Microcapsules - a Survey of Manufacturing Techniques .1. Suspension Cross-Linking*, Polymer Engineering and Science, **29** (24): 1746-1758, 1989.

[180] B. G. De Geest, C. Dejugnat, G. B. Sukhorukov, K. Braeckmans, S. C. De Smedt and J. Demeester, *Self-rupturing microcapsules*, Advanced Materials, **17** (19): 2357-+, 2005.

[181] H. Y. Koo, S. T. Chang, W. S. Choi, J. H. Park, D. Y. Kim and O. D. Velev, *Emulsion-based synthesis of reversibly swellable, magnetic nanoparticle-embedded polymer microcapsules*, Chemistry of Materials, **18** (14): 3308-3313, 2006.

[182] X. Y. Liu, C. Y. Gao, J. C. Shen and H. Mohwald, *Multilayer microcapsules as anti-cancer drug delivery vehicle: Deposition, sustained release, and in vitro bioactivity*, Macromolecular Bioscience, **5** (12): 1209-1219, 2005.

[183] B. Neu, A. Voigt, R. Mitlohner, S. Leporatti, C. Y. Gao, E. Donath, H. Kiesewetter, H. Mohwald, H. J. Meiselman and H. Baumler, *Biological cells as templates for hollow microcapsules*, Journal of Microencapsulation, **18** (3): 385-395, 2001.

[184] V. V. Tsukruk, O. Shchepelina, V. Kozlovskaya, S. Singamaneni and E. Kharlampieva, *Replication of anisotropic dispersed particulates and complex continuous templates*, Journal of Materials Chemistry, **20** (32): 6587-6603, 2010.

[185] J. P. Zhang, X. H. Zhao, Z. G. Suo and H. Q. Jiang, *A finite element method for transient analysis of concurrent large deformation and mass transport in gels (vol 105, 093522, 2009)*, Journal of Applied Physics, **105** (12), 2009.

[186] W. Hong, X. H. Zhao, J. X. Zhou and Z. G. Suo, *A theory of coupled diffusion and large deformation in polymeric gels*, Journal of the Mechanics and Physics of Solids, **56** (5): 1779-1793, 2008.

[187] D. Y. Arifin, L. Y. Lee and C. H. Wang, *Mathematical modeling and simulation of drug release from microspheres: Implications to drug delivery systems*, Adv. Drug Deliver. Rev., **58** (12-13): 1274-1325, 2006.

[188] C. S. Brazel and L. F. Wu, *Mathematical model to predict drug release, including the early-time burst effect, from swellable homogeneous hydrogels*, Ind. Eng. Chem. Res., **47** (5): 1518-1526, 2008.

[189] M. Grassi, G. Lamberti, S. Cascone and G. Grassi, *Mathematical modeling of simultaneous drug release and in vivo absorption*, Int. J. Pharm.: DOI: 10.1016/j.ijpharm.2010.1012.1044, 2011.

[190] E. Kaunisto, M. Marucci, P. Borgquist and A. Axelsson, *Mechanistic modelling of drug release from polymer-coated and swelling and dissolving polymer matrix systems*, Int. J. Pharm.: DOI: 10.1016/j.ijpharm.2011.1001.1021, 2011.

[191] L. L. Lao, N. A. Peppas, F. Y. C. Boey and S. S. Venkatraman, *Modeling of drug release from bulk-degrading polymers*, Int. J. Pharm.: DOI: 10.1016/j.ijpharm.2010.1012.1020, 2011.

[192] C. Kleinstreuer and Z. Zhang, *Optimal Drug-Aerosol Delivery to Predetermined Lung Sites*, Journal of Heat Transfer-Transactions of the Asme, **133** (1): 011002, 2011.

[193] L. Huynh, C. Neale, R. Pomès and C. Allen, *Computational approaches to the rational design of nanoemulsions, polymeric micelles, and dendrimers for drug delivery*, Nanomed.-Nanotechnol. Biol. Med.: DOI: 10.1016/j.nano.2011.1005.1006, 2011.

[194] A. T. Metters and C. C. Lin, *Hydrogels in controlled release formulations: Network design and mathematical modeling*, Adv. Drug Del. Rev., **58** (12-13): 1379-1408, 2006.

[195] N. Clarke and G. A. Buxton, *Drug diffusion from polymer core-shell nanoparticles*, Soft Matter, **3** (12): 1513-1517, 2007.

[196] S. Zhang, L. Shang, H. J. Du and S. S. Venkatraman, *A novel approach for the control of drug release rate through hydrogel membrane - II. Thermodynamic modeling of the partition control scheme*, Journal of Membrane Science, **321** (2): 331-336, 2008.

[197] S. Zhang, L. Shang, H. Du and S. S. Venkatraman, *A novel approach for the control of drug release rate through hydrogel membrane: I. Effect of drug immobilization on drug release rate by copolymerization method*, European Journal of Pharmaceutics and Biopharmaceutics, **68** (3): 715-723, 2008.

[198] H. Mohammadi and W. Herzog, *A novel model for diffusion based release kinetics using an inverse numerical method*, Med. Eng. Phys.: DOI: 10.1016/j.medengphy.2011.1002.1003, 2011.

[199] Y. Li and T. Tanaka, *Kinetics of Swelling and Shrinking of Gels*, Journal of Chemical Physics, **92** (2): 1365-1371, 1990.

[200] T. Tanaka, *Kinetics of Phase-Transition in Polymer Gels*, Physica A, **140** (1-2): 261-268, 1986.

[201] A. Peters and S. J. Candau, *Kinetics of Swelling of Spherical and Cylindrical Gels*, Macromolecules, **21** (7): 2278-2282, 1988.

[202] A. Suzuki and T. Hara, *Kinetics of one-dimensional swelling and shrinking of polymer gels under mechanical constraint*, Journal of Chemical Physics, **114** (11): 5012-5015, 2001.

[203] C. J. Wang, Y. Li and Z. B. Hu, *Swelling kinetics of polymer gels*, Macromolecules, **30** (16): 4727-4732, 1997.

[204] S. K. De, N. R. Aluru, B. Johnson, W. C. Crone, D. J. Beebe and J. Moore, *Equilibrium swelling and kinetics of pH-responsive hydrogels: Models, experiments, and simulations*, Journal of Microelectromechanical Systems, **11** (5): 544-555, 2002.

[205] Z. G. Suo, R. Marcombe, S. Q. Cai, W. Hong, X. H. Zhao and Y. Lapusta, *A theory of constrained swelling of a pH-sensitive hydrogel*, Soft Matter, **6** (4): 784-793, 2010.

[206] M. O. de la Cruz, P. K. Jha, J. W. Zwanikken, F. A. Detcheverry and J. J. de Pablo, *Study of volume phase transitions in polymeric nanogels by theoretically informed coarse-grained simulations*, Soft Matter, **7** (13): 5965-5975, 2011.

[207] F. H. Meng, Z. Y. Zhong and J. Feijen, *Stimuli-Responsive Polymersomes for Programmed Drug Delivery*, Biomacromolecules, **10** (2): 197-209, 2009.

[208] A. P. Esser-Kahn, S. A. Odom, N. R. Sottos, S. R. White and J. S. Moore, *Triggered Release from Polymer Capsules*, Macromolecules, **44** (14): 5539-5553, 2011.

[209] Y. L. Luo, Y. S. Shiao and Y. F. Huang, *Release of Photoactivatable Drugs from Plasmonic Nanoparticles for Targeted Cancer Therapy*, ACS Nano, **5** (10): 7796-7804, 2011.

[210] M. S. Shoichet, Y. F. Wang, Y. Lapitsky and C. E. Kang, *Accelerated release of a sparingly soluble drug from an injectable hyaluronan-methylcellulose hydrogel*, Journal of Controlled Release, **140** (3): 218-223, 2009.

[211] G. A. Buxton and E. W. Durbin, *A coarse-grained model of targeted drug delivery from responsive polymer nanoparticles*, Soft Matter, **6** (4): 762-767, 2010.

[212] J. S. Soares and P. Zunino, *A mixture model for water uptake, degradation, erosion and drug release from polydisperse polymeric networks*, Biomaterials, **31** (11): 3032-3042, 2010.

[213] Y. Qian, X. D. Guo, L. J. Zhang and Z. M. Wu, *Dissipative Particle Dynamics Studies on Microstructure of pH-Sensitive Micelles for Sustained Drug Delivery*, Macromolecules, **43** (18): 7839-7844, 2010.

[214] T. Srinophakun and J. Boonmee, *Preliminary Study of Conformation and Drug Release Mechanism of Doxorubicin-Conjugated Glycol Chitosan, via cis-Aconityl Linkage, by Molecular Modeling*, International Journal of Molecular Sciences, **12** (3): 1672-1683, 2011.

[215] Z. Modrzejewska, R. Zarzycki, G. Rogacki and K. Nawrotek, *Modeling of Drug (Albumin) Release from Thermosensitive Chitosan Hydrogels*, Industrial & Engineering Chemistry Research, **50** (9): 5866-5872, 2011.

[216] Y. H. Bae, T. Okano and S. W. Kim, *On-Off Thermocontrol of Solute Transport .2. Solute Release from Thermosensitive Hydrogels*, Pharmaceutical Research, **8** (5): 624-628, 1991.

[217] K. Kono, S. Kimura and Y. Imanishi, *Ph-Responsive Permeability of Polyamide Capsule Membrane Coated with Lipid Molecules and Amphiphilic Polypeptides*, Journal of Membrane Science, **58** (1): 1-9, 1991.

[218] A. Gutowska, J. S. Bark, I. C. Kwon, Y. H. Bae, Y. Cha and S. W. Kim, *Squeezing hydrogels for controlled oral drug delivery*, Journal of Controlled Release, **48** (2-3): 141-148, 1997.

[219] Z. M. Xing, C. L. Wang, J. Yan, L. Zhang, L. Li and L. S. Zha, *Dual stimuli responsive hollow nanogels with IPN structure for temperature controlling drug loading and pH triggering drug release*, Soft Matter, **7** (18): 7992-7997, 2011.

[220] A. M. Pavlov, V. Saez, A. Cobley, J. Graves, G. B. Sukhorukov and T. J. Mason, *Controlled protein release from microcapsules with composite shells using high frequency ultrasound-potential for in vivo medical use*, Soft Matter, **7** (9): 4341-4347, 2011.

[221] C. Gao, E. Donath, S. Moya, V. Dudnik and H. Mohwald, *Elasticity of hollow polyelectrolyte capsules prepared by the layer-by-layer technique*, European Physical Journal E, **5** (1): 21-27, 2001.

[222] W. Mickel, S. Munster, L. M. Jawerth, D. A. Vader, D. A. Weitz, A. P. Sheppard, K. Mecke, B. Fabry and G. E. Schroder-Turk, *Robust Pore Size Analysis of Filamentous Networks from Three-Dimensional Confocal Microscopy*, Biophysical Journal, **95** (12): 6072-6080, 2008.

[223] Q. J. He, L. M. Guo, F. M. Cui, Y. Chen, P. Jiang and J. L. Shi, *Facile one-pot synthesis and drug storage/release properties of hollow micro/mesoporous organosilica nanospheres*, Materials Letters, **63** (22): 1943-1945, 2009.

[224] Y. F. Zhu and J. L. Shi, *A mesoporous core-shell structure for pH-controlled storage and release of water-soluble drug*, Microporous and Mesoporous Materials, **103** (1-3): 243-249, 2007.

[225] Y. F. Zhu, J. L. Shi, W. H. Shen, X. P. Dong, J. W. Feng, M. L. Ruan and Y. S. Li, *Stimuli-responsive controlled drug release from a hollow mesoporous silica sphere/polyelectrolyte multilayer core-shell structure*, Angewandte Chemie-International Edition, **44** (32): 5083-5087, 2005.

[226] S. Gam, J. S. Meth, S. G. Zane, C. Z. Chi, B. A. Wood, M. E. Seitz, K. I. Winey, N. Clarke and R. J. Composto, *Macromolecular Diffusion in a Crowded Polymer Nanocomposite*, Macromolecules, **44** (9): 3494-3501, 2011.

[227] Z. B. Hu, X. M. Zhang and Y. Li, *Synthesis and Application of Modulated Polymer Gels*, Science, **269** (5223): 525-527, 1995.

[228] Y. Li and T. Tanaka, *Phase-Transitions of Gels*, Annual Review of Materials Science, **22**: 243-277, 1992.

[229] H. Allan S, *Applications of thermally reversible polymers and hydrogels in therapeutics and diagnostics*, Journal of Controlled Release, **6** (1): 297-305, 1987.

[230] T. Okano and A. Kikuchi, *Pulsatile drug release control using hydrogels*, Advanced Drug Delivery Reviews, **54** (1): 53-77, 2002.

[231] R. Yoshida, K. Sakai, T. Okano and Y. Sakurai, *Pulsatile Drug-Delivery Systems Using Hydrogels*, Advanced Drug Delivery Reviews, **11** (1-2): 85-108, 1993.

[232] D. Patel, B. Patel and C. Patel, *An overview on intelligent drug delivery systems*, International Journal of Advances in Pharmaceutical Research, **2** (2): 57-63, 2011.

[233] L. S. Zha, Y. Zhang, W. L. Yang and S. K. Fu, *Monodisperse temperature-sensitive microcontainers*, Advanced Materials, **14** (15): 1090-1092, 2002.

[234] Y. J. Zhang, Y. Guan and S. Q. Zhou, *Synthesis and volume phase transitions of glucose-sensitive microgels*, Biomacromolecules, **7** (11): 3196-3201, 2006.

[235] Z. Xing, C. Wang, J. Yan, L. Zhang, L. Li and L. Zha, *Dual stimuli responsive hollow nanogels with IPN structure for temperature controlling drug loading and pH triggering drug release*, Soft Matter, **7** (18): 7992-7997, 2011.

[236] A. S. Zahr, M. de Villiers and M. V. Pishko, *Encapsulation of drug nanoparticles in self-assembled macromolecular nanoshells*, Langmuir, **21** (1): 403-410, 2005.

[237] Y. J. Wang, Y. Yan, J. W. Cui, L. Hosta-Rigau, J. K. Heath, E. C. Nice and F. Caruso, *Encapsulation of Water-Insoluble Drugs in Polymer Capsules Prepared Using Mesoporous Silica Templates for Intracellular Drug Delivery*, Advanced Materials, **22** (38): 4293-4297, 2010.

[238] V. Kozlovskaya, E. Kharlampieva, M. L. Mansfield and S. A. Sukhishvili, *Poly(methacrylic acid) hydrogel films and capsules: Response to pH and ionic strength, and encapsulation of macromolecules*, Chemistry of Materials, **18** (2): 328-336, 2006.

[239] S. H. Kim, H. Hwang, C. H. Lim, J. W. Shim and S. M. Yang, *Packing of Emulsion Droplets: Structural and Functional Motifs for Multi-Cored Microcapsules*, Advanced Functional Materials, **21** (9): 1608-1615, 2011.

[240] H. C. Shum, Y. J. Zhao, S. H. Kim and D. A. Weitz, *Multicompartment Polymersomes from Double Emulsions*, Angewandte Chemie-International Edition, **50** (7): 1648-1651, 2011.

[241] L. Dahne, S. Leporatti, E. Donath and H. Mohwald, *Fabrication of micro reaction cages with tailored properties*, Journal of the American Chemical Society, **123** (23): 5431-5436, 2001.

[242] D. M. Vriezema, M. C. Aragones, J. A. A. W. Elemans, J. J. L. M. Cornelissen, A. E. Rowan and R. J. M. Nolte, *Self-assembled nanoreactors*, Chemical Reviews, **105** (4): 1445-1489, 2005.

[243] O. Shchepelina, V. Kozlovskaya, E. Kharlampieva, W. B. Mao, A. Alexeev and V. V. Tsukruk, *Anisotropic Micro- and Nano-Capsules*, Macromolecular Rapid Communications, **31** (23): 2041-2046, 2010.

[244] B. N. J. Persson, *Theory of rubber friction and contact mechanics*, Journal of Chemical Physics, **115** (8): 3840-3861, 2001.

[245] B. N. J. Persson and A. I. Volokitin, *Rubber friction on smooth surfaces*, European Physical Journal E, **21** (1): 69-80, 2006.

[246] K. Vorvolakos and M. K. Chaudhury, *The effects of molecular weight and temperature on the kinetic friction of silicone rubbers*, Langmuir, **19** (17): 6778-6787, 2003.

[247] C. J. Rand and A. J. Crosby, *Friction of soft elastomeric wrinkled surfaces*, Journal of Applied Physics, **106** (6), 2009.

[248] R. Venkatasubramanian, K. J. Jin and N. S. Pesika, *Use of Electrochemical Deposition to Create Randomly Rough Surfaces and Roughness Gradients*, Langmuir, **27** (7): 3261-3265, 2011.

[249] D. Martina, C. Creton, P. Damman, M. Jeusette and A. Lindner, *Adhesion of soft viscoelastic adhesives on periodic rough surfaces*, Soft Matter, **8** (19): 5350-5357, 2012.

[250] B. He, W. Chen and Q. J. Wang, *Surface texture effect on friction of a microtextured poly(dimethylsiloxane) (PDMS)*, Tribology Letters, **31** (3): 187-197, 2008.

[251] S. Sills, K. Vorvolakos, M. K. Chaudhury and R. M. Overney, edited by E. Gnecco and E. Meyer Springer Berlin Heidelberg: pp. 659-676, 2007.

[252] M. Rubinstein and R. H. Colby, *Polymer physics*. Oxford University Press, Oxford ; New York, 2003.

[253] W. Philippoff, *Mechanical Investigations of Elastomers in a Wide Range of Frequencies*, Journal of Applied Physics, **24** (6): 685-689, 1953.

[254] B. N. J. Persson, O. Albohr, G. Heinrich and H. Ueba, *Crack propagation in rubber-like materials*, Journal of Physics-Condensed Matter, **17** (44): R1071-R1142, 2005.

[255] M. K. Chaudhury, K. Vorvolakos and D. Malotky, in *Polymer thin films*, edited by O. K. C. Tsui and T. P. Russell World Scientific Pub Co Inc, Singapore: pp. 195-219, 2008.

[256] B. N. J. Persson, *Rubber friction: role of the flash temperature*, Journal of Physics-Condensed Matter, **18** (32): 7789-7823, 2006.

[257] Schallam.A, *Abrasion Fatigue and Smearing of Rubber*, Journal of Applied Polymer Science, **12** (2): 281-&, 1968.

[258] K. A. Grosch, *Realtion between Friction and Visco-Elastic Properties of Rubber*, Proceedings of the Royal Society of London Series a-Mathematical and Physical Sciences, **274** (1356): 21-+, 1963.

[259] K. Mori, S. Kaneda, K. Kanae, H. Hirahara, Y. Oishi and A. Iwabuchi, *Influence on Friction Force of Adhesion Force between Vulcanizates and Sliders*, Rubber Chemistry and Technology, **67** (5): 797-805, 1994.

VITA

HASSAN MASOUD

Hassan Masoud was born in the historic city of Shiraz located in the southwest of Iran. He graduated from Tohid high school in 2002 and received his B.S. degree with Highest Honors in Aerospace Engineering from the Sharif University of Technology, Tehran, Iran in 2006. Subsequently, he joined the State University of New York at Buffalo where he earned his M.S. degree in Mechanical Engineering in 2009. Hassan then moved to Georgia Tech to pursue a Ph.D. also in Mechanical Engineering. Hassan employs theory and computer simulations to find solutions to challenging problems at the intersection of engineering, physics, and biology. His research interests include mechanics of soft and active materials, fluid-structure interactions, small scale fluid mechanics, and biomimetic design.